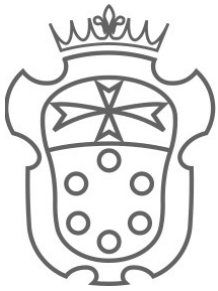

Scuola Normale Superiore

Ph. D. Thesis in Physics

Photonic engineering of CW, ultrabroad gain, aperiodic quantum cascade lasers at terahertz frequencies, integration with 2D materials and study of the optical mode dynamics

Simone Biasco

Advisor:
Prof. Miriam Serena Vitiello

Internal supervisor:
Prof. Giuseppe Carlo La Rocca

Contents

INTRODUCTION

The terahertz (THz) frequency range of the electromagnetic spectrum is usually defined in the range between 0.1 THz and 10 THz, corresponding to wavelengths in the interval from 3 mm to 30 μm, lying in-between the infrared and the microwave spectral regimes. In recent years, the progress of THz technology has fostered interdisciplinary research in spectroscopy and tomography to map macroscopic systems, (chemical detection and imaging, amongst others [1]) or microscopic ones, such as nanoparticles and nanowires on either static or dynamic timescales [2].

THz radiation is commonly generated with photoconductive emitters [3-5], semiconductor diodes [6], free-electron lasers [7], photomixing [8], and beating of a pump and idler signal from non-linear crystals [9,10]. These approaches are often bulky, expensive or with limited optical powers [11]. The breakthrough demonstration of quantum cascade lasers operating in the far-infrared, and based on quantum engineered heterostructures [12], paved the way to the development of much more compact, efficient and powerful semiconductor THz sources. Thanks to the atomic-layer resolution ensured in the heterostructure growth by molecular beam epitaxy (MBE) [13], very accurate designs can be implemented via a proper sequence of quantum barriers and quantum wells. In this way, sharp discontinuities in the conduction and valence bands edges are created, in order to manipulate the electron energy levels and wavefunction localization, and to provide optical intersubband transitions at the desired frequencies. [14]

Nowadays, miniaturized THz QCLs can provide coherent emission over the frequency range between 1.2 THz and 5.6 THz [15, 16], demonstrating Watt-level powers [17,18] and a maximum operation temperature of ≈ 210 K in pulsed regime [19] and ≈ 130 K in continuous-wave (CW) mode [20]. The optimization of the optical power and efficiency, as well as control over the emission spectrum and the beam profile are critical aspects for the performance of the laser. Indeed, high-power CW operation with tailored single-mode or multimode spectra have many potential applications, but it is challenging to address all these aspects, simultaneously. For example, since light is confined at sub-wavelength scales by the THz QCL waveguide in the conventional Fabry-Perot configuration, diffraction effects typically hinder a good beam collimation.

A very promising approach to control the emission of THz QCLs relies on engineering light propagation in the resonator, by introducing scattering elements which interact with the photon wavevector and provide the feedback and extraction mechanism, necessary to light amplification and outcoupling. THz resonator architectures based on distributed feedback (DFB) gratings [21-25] or periodic photonic crystal patterns [26,27] have been demonstrated over the recent years, achieving controlled far-field intensity profile and spectra. However, the latter structures typically suffer from the poor power extraction associated to their intrinsic symmetry and periodicity, or involve demanding lithographical constraints in the device micro-fabrication.
Alternative solutions to circumvent this issue rely on introducing specific asymmetries in the laser cavity or even devising cavity-less resonators which can allow modifying the coherent nature of the laser emission. Furthermore, changes in the laser emission features can be achieved via a local perturbation of the beam spatial and spectral properties, either by devising optical micro-cavities coupled on-chip on the laser surface of by means of an optical material that, once embedded intra-cavity or coupled with it, can locally perturb the electromagnetic field.
The objective of the present thesis is the investigation of photonic engineering architectures to tailor the spectral and spatial emission of THz QCLs to simultaneously achieve high power, continuous wave (CW) operation, collimated beam profiles, high slope efficiencies, tunable emission. The latter goals are achieved by implementing aperiodic photonic patterns on the resonator surface. Furthermore, the influence of graphene saturable absorbers based on 2D materials on the laser emission properties is explored.

Surface photonic patterns exploiting violations of the crystal lattice periodicity have been investigated in recent years, since their broken spatial symmetries allow circumventing the limitations of conventional photonic crystal structures, while requiring standard cleanroom fabrication processes. For example, aperiodic THz resonators based on a double-metal waveguide feature dual periodicity gratings [28] or integrate one-dimensional [29] and two-dimensional [30,31] deterministic quasi-crystal patterns in the top metal layer of the laser, or even exploiting completely disordered scheme like the random laser [32-34]. These different architectures allow controlling the interaction between THz radiation and the scattering wavevectors, as well as the radiative losses,

achieving significant optical powers of some tens of mW and determining the emission frequency and beam profile. However, it is challenging to address these aspects, simultaneously.

In the present thesis, the influence of aperiodic patterns in one dimensional (1D) or two-dimensional (2D) resonators is explored in a number of different one-dimensional and two-dimensional photonic geometries, based on both deterministic and non-deterministic generation algorithms.

The first photonic concept devised in the present thesis is a one-dimensional wire laser architecture exploiting a combination of two distinct photonic gratings: a lateral sinusoidal corrugation of the ridge width and a sequence of extraction holes placed on the top metal surface of the device. This approach allows achieving independent control and manipulation of the extraction and feedback mechanism, which are governed by the top hole grating and the ridge corrugation, respectively. The fine-tuning of the extraction wavevector ensures tailored emission direction and narrow beam divergence, enhanced optical power and efficiency, as well as robust single-mode selection based on the high-quality factor modes resonating in the device in both pulsed and CW operations.

As an alternative approach a one-dimensional laser which exploits a sequence of open slits in the top metal cladding, specifically distributed to reproduce a quasi-crystal pattern which inherently features spatial periodicity breaking, and supports lasing on the modes at the edges of the photonic frequency pseudo-bandgaps, have been exploited. The complex photon scattering induced by the quasi-crystal grating can be tuned by varying the resonator geometric parameters to achieve single- or multi-mode emission, control the beam shape and optimize the power output, reaching record slope efficiencies.

The effect of an even stronger disorder is studied with the development of two-dimensional resonators integrating a distribution of completely random holes in the top metal layer of the THz QCLs. The random air holes provide the photon multiple scattering for light feedback, without need for a traditional cavity, as well as the out-coupling to free space. The rich interference patterns result in an intrinsically multimode emission over a broad spectral bandwidth, with beam

profiles which strongly depend on the density of the holes as well as on the device area.
The investigated photonic architectures offer a concrete perspective for the optimization and tuning of THz QCLs by design, yet further control over the THz QCL emission can be achieved by an external modulation, providing a feedback controlled by a coupled micro-cavity with varying size. Indeed, a selective frequency tuning and intensity modulation of the multimode spectra of quasi-crystal and random devices was demonstrated.

As a final goal the present thesis describes the influence on the laser emission properties of a bi-dimensional multilayer 2D material, commenting on how it can induce modify the emission properties of a laser. In this respect, two-dimensional materials like graphene have attracted attention due to their unique optoelectronic properties recently exploited at THz frequency [35-37] and to the possibility of intra-cavity integration. This would open novel directions for mode manipulations, thanks to the combination of the local high intensity of the near-field radiation and the non-linear effects of graphene, such as the saturable absorption recently demonstrated in the THz range [38,39].

Different samples of multilayer graphene were investigated, demonstrating a promising potential for efficient tuning of multimode, aperiodic THz QCLs.

The present Ph.D. thesis is organized as follows:

- Chapter 1 provides an overview of the basic principles of QCLs, with a special focus on state of the art photonic engineering architectures for tailoring the laser emission at THz frequencies.
- Chapter 2 introduces the development and characterization of distributed feedback corrugated wire lasers, specifically engineered to separately control the feedback and extraction of radiation in CW regime [40].
- Chapter 3 illustrates the basic principles and experimental development of surface-emitting, one-dimensional quasi-crystal lasers, providing record slope efficiencies and high output power [41].
- Chapter 4 presents the computational investigation and experimental demonstration of the first electrically pumped CW random THz lasers [42].

- Chapter 5 details the mode dynamics of aperiodic THz QCLs, when their multimode emission is coupled to an external micro-cavity or multilayer graphene samples, showing selective frequency tuning and intensity modulation, or the activation of additional spectral peaks due to the interaction with the samples of the two-dimensional material, respectively.

Finally, the conclusions and future perspectives of the work of the present thesis are described in the last section.

CHAPTER 1:
TERAHERTZ QUANTUM CASCADE LASERS AND MODE ENGINEERING

1.1 Terahertz quantum cascade lasers

1.1.1 Quantum cascade heterostructures

A quantum cascade laser (QCL) is a unipolar semiconductor device emitting coherently at mid-infrared (mid-IR) or Terahertz (THz) frequencies [43] and based on two main elements:

- an active material which is electrically pumped to generate and amplify photons via stimulated emission
- a resonator providing the feedback to allow radiation propagating in the active material and outcouple to the free space.

A QCL heterostructure relies on a multiple-quantum-well system grown by molecular beam epitaxy (MBE), typically formed by a sequence of alternating layers of semiconductor materials having different conduction band levels, usually III-V structures like GaAs/$Al_xGa_{1-x}As$, InP/$Ga_xIn_{1-x}P$, InAs/ $Al_xIn_{1-x}As$, AlN/GaN and GaN/$Al_xGa_{1-x}N$. The resulting heterostructure is designed with specific choice of materials, layer thicknesses and doping levels to achieve the desired spatial sequence of quantum wells and barriers along the growth direction, engineering the local electron energy levels (or subbands), the localization of the wavefunctions and the scattering properties to control the electron population and the emission frequency of the laser.

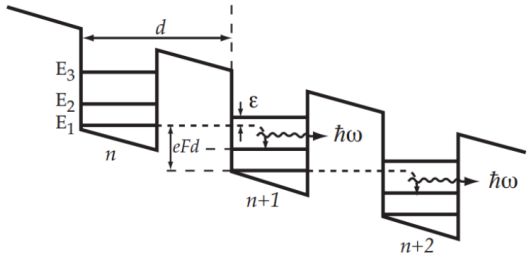

Figure 1.1: A schematic representation of the quantum cascade mechanism proposed by Kazarinov and Suris, from [43]. Under the application of a bias, an electron cascades through a sequence of quantum wells and barriers, emitting a photon at each transition between radiative energy levels.

As reported in figure 1.1, the first proposal of the multi-quantum well superlattice [44] by Kazarinov and Suris, was theoretically investigated as a model system in which the application of an external bias makes optical

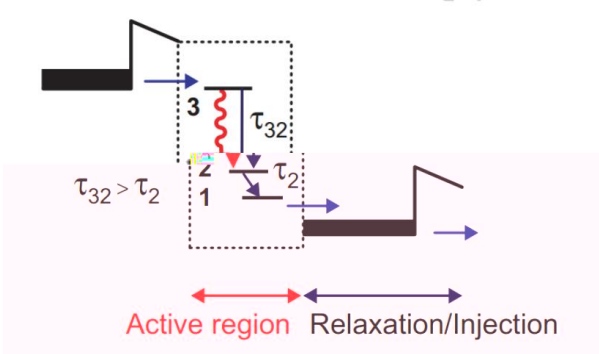

Figure 1.2: Diagram of the three-level model for a single period of a QCL heterostructure, showing the $_{32}$. The fast depletion of level 2 $_2$ $_{32}$ $_2$. From [43].

transitions possible between subbands localized in the same quantum well or between subbands of two adjacent wells. In the latter case, an increase of the barrier thickness diminishes the probability of interaction between wavefunctions confined in adjacent wells, making optical transitions between subbands n = 3 and n = 2 of the same well more likely. The fast depletion of the second level towards the subband n = 1 favors the electron population inversion between n = 3 and n = 2. The band tilting induced by the external electric field applied across the heterostructure can be tuned to align the ground state level of each quantum well to an excited subband in the next quantum well. In this way, the injected electrons are resonantly transferred from one well to the next one, inducing the cascade mechanism. This simple theoretical superlattice model paved the way to the exploitation of inter-subband transitions for lasing action, which was later achieved with a mid-IR QCL [45], based on a more complex quantum structure with a periodic repetition of a unit cell with engineered barriers and wells. The resulting transitions produce photons with the electric field parallel to the growth axis, i.e. with TM polarization due to a transition selection rule. [46]

The QCL active material has a unit cell made up of two main sections: the active region and the relaxation region, as shown in figure 1.2. In the gain region, electrons are selectively injected in the upper state 3 and radiatively $_{32}$, emitting a photon with energy $_3$ - E_2. These subband energies can be finely tuned by choosing the appropriate materials for the barriers and the wells, and defining their thicknesses. Level 2 is depleted due to the strong coupling to level 1, with a fast

2 32, so that electrons are then injected into the relaxation region. This part is made up by a sequence of barriers and wells with different thickness, producing a graded energy gap which increases the electron energy with respect to the bottom of the band and optimizes the injection into the next unit cell. This region is typically doped with silicon atoms to provide charge neutrality and avoid the formation of local electrical domains altering the electron flow. The accurate design of the energy levels ensures selective injection of carriers in the next upper radiative level, in presence of an external field applied to the material. Therefore, each electron is then reused in the next unit period, producing as many photons as many repeated unit cells are in the system, making this cascading mechanism very efficient. More photons are produced increasing the number of periods N_p in the heterostructure, which also helps to lower the threshold current since this reduces the population density per single unit cell, so that ohmic losses are limited. However, the detrimental absorption losses and scattering effects increase linearly with the number of periods, so the overall heterostructure size is typically limited to some tens of periods for mid-IR QCLs and about 200 periods for THz QCLs.

The discussed model only considers the subband levels arising from the electron localization along the heterostructure growth axis z, but the carriers also have an energy dispersion associated to the motion in the orthogonal x-y plane. As shown in figure 1.3 in the case of an effective mass model with small non-parabolicities, the different energy parabolas are stacked by an energy offset corresponding to the subband level, but all the emitted photons practically have the same frequency, giving a narrow linewidth.

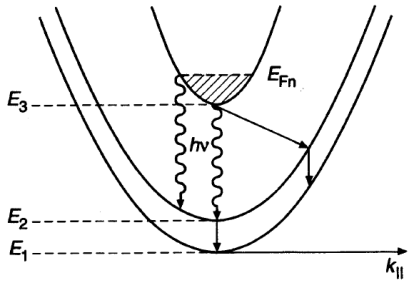

Figure 1.3: Schematic representation of the dispersion of the n = 1, 2, and 3 states parallel to the layers, as functions of the in-plane momentum $k_{||}$. An electron population is in the subband n = 3 up to the non-equilibrium quasi-Fermi energy E_{Fn} and radiatively decays in level n = 2 (wavy -radiative decays via interaction with inter-subband optical-phonons are indicated with straight arrows. From [45]

1.1.2 QCL rate equations

The fundamental operation of a QCL can be described exploiting the simple three-level model of the gain region with length L_p [43] introduced above in figure 1.2. A current density J injects electrons with charge q_0 in level 3, giving a carrier density N_3 $_3$. An optical transition from level 3 $_{32}$ populates the intermediate level 2 up to a density N_2 $_2$, for example by strong scattering with longitudinal optical (LO) phonons in the material. The associated stationary rate equations are:

$$\begin{aligned} \frac{\partial N_3}{\partial t} &= \frac{J}{q_0} - \frac{N_3}{\tau_3} = 0 \\ \frac{\partial N_2}{\partial t} &= \frac{N_3}{\tau_{32}} - \frac{N_2}{\tau_2} = 0 \end{aligned} \tag{1}$$

which give a population difference between levels 3 and 2:

$$N_3 - N_2 = \left(1 - \frac{\tau_2}{\tau_{32}}\right)\frac{\tau_3 J}{q_0} \tag{2}$$

P $_2$ $_{32}$ and increases linearly with the injected current density. The threshold current density J_{th} is reached when the waveguide and mirror losses are compensated by

$$g = \tau_2\left(1 - \frac{\tau_2}{\tau_{32}}\right)\frac{4\pi q_0 Z_{32}^2}{n\lambda\varepsilon_0 L_p}\frac{1}{\gamma_{32}} \tag{3}$$

where Z_{32} is the dipole matrix element associated to th $_{32}$ is the full width at half maximum of the transition, n is the material $_0$ is the vacuum permittivity. Above threshold, the gain is clamped to this value, giving a photon flux S which scales linearly with the injected current density. However, the increase of the emitted radiation intensity is limited by the negative differential resistance (NDR) effect, associated to the band misalignment induced by an excessive bias. This means there is a current density at which the optical power output is maximum, called J_{max}. More refined equations are needed to accurately describe the complexity of the transport and gain mechanisms in a QCL, yet this model intuitively highlights the connection between electrical pumping, population inversion and inter-subband transitions processes.

1.1.3 Quantum design of THz QCL active regions

The THz frequency region is approximately defined as the range of photon energies between 0.4 meV and 41 meV, which made the demonstration [12] of THz QCLs more challenging with respect to mid-IR devices. Indeed, the

- Chirped Superlattice design

The CSL heterostructure (fig. 1.4a) features a number of miniband of states, produced by many quantum wells coupled together, with a gradual chirp of the barrier and well thicknesses. The radiative transition takes place between the lowest state of the upper miniband 2 and the highest state of the lower miniband 1. Since the intra-miniband electron scattering is 10 times faster than the inter-band scattering time, the depletion of level 1 is very efficient, favoring the population inversion required for laser action. The typical length of one CSL period is about 100 nm and this was the design implemented for the first demonstration of a THz QCL.

- Bound-to-continuum design

The BTC design (fig. 1.4b) still exploits miniband of states, but its upper radiative state 2 is tuned to an energy within the forbidden minigap. The wavefunction of the final state 1 has maximum intensity shifted with respect to state 2, as they are localized in different wells, producing a diagonal transition in real space. This results in a reduced coupling between the two states, and an increase for the upper miniband lifetime due to limited non-radiative scattering rate. Due to the stronger coupling between the upper state and the injector states, the BTC scheme improved the thermal performance and efficiency.

- Resonant-phonon design

The RP scheme (fig. 1.4c) does not use minibands, but takes advantage of LO phonon-electron interaction, which is one of the main scattering mechanisms in a QCL. Indeed, a collector/injector state is engineered to lie below the lower radiative state 1, with an energy difference corresponding to the typical LO phonon energy (in GaAs, about 36 meV). In this way, state 1 is depleted very rapidly (< 1 ps) due to the electron relaxation with the emission of one LO phonon. This phonon-assisted depopulation is enhanced for significant overlap between state 1 and the collector wavefunction, while the upper state 2 is spatially confined to minimize the interaction with the collector state. This design optimizes the different lifetimes so that population inversion is more easily reached, allowing a reduced period of about 50 nm.

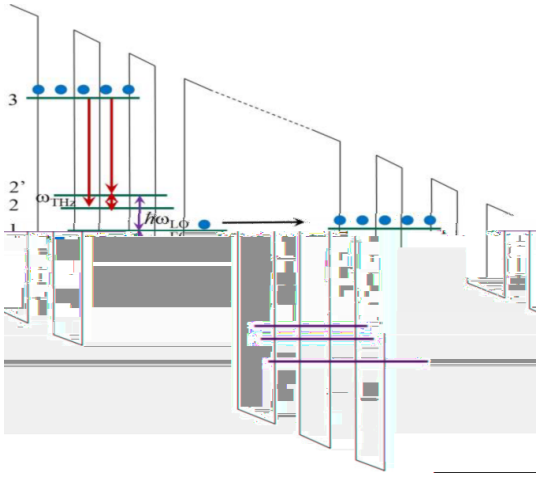

Figure 1.5: a) Schematic of the DFG process between the electron states in a band structure of quantum cascade laser, in which mid-IR photons
2) 1). The results in the
generation of THz 1 - 2. From [48]

- Difference-frequency generation design

DFG THz active materials are monolithically integrated heterostructures operating with a dual-wavelength infrared emission and featuring giant second-order non- (2) associated to the inter-subband transitions in coupled quantum wells. A possible approach is the use of two distinct quantum cascade sections engineered to produce mid-IR photons with distinct frequencies, as shown in figure 1.5. By coupling two infrared waves with 1 2 and wavevectors $\mathbf{k}_1$ and $\mathbf{k}_2$ respectively in the non- 1 - 2 and wavevector $\mathbf{k}$ [48,49] The efficiency of the DFG process increases with large (2) and in presence of wavevector phase matching:

$$|\mathbf{k} - (\mathbf{k}_1 - \mathbf{k}_2))| \approx 0 \tag{4}$$

The crucial advantage of this concept is that it allows the generation of coherent THz radiation at room temperature, since it is based on the mid-IR QCL active medium, for pulsed [50] and CW [51] operations. By accurate resonator engineering, purified single-mode DFG emission can be obtained [52] and tuned over a broad spectral range in the THz region [53]. The flexibility of the DFG scheme has recently been further demonstrated by the generation of THz

frequency combs via down-converting a mid-IR comb with an integrated mid-IR single-mode source, without using any external optical elements. [54]

1.1.4 Figures of merit of a QCL

The transport and optical performance of a THz QCL is assessed by measuring the current density-voltage (J-V) characteristic and the current density-optical power (J-L) curve, also known as LJV. Some of the main parameters are[55]:

- threshold current density:

laser action starts at a minimum current value I_{th}, which can be divided by the device are to retrieve the threshold current density J_{th}

- current density at maximum emission:

at the maximum power output condition, the measured current is I_{max} and is easily connected to the density J_{max}, which defines the operational dynamic range of the laser

- maximum optical power:

the maximum value of the radiation emitted by a QCL is

- slope efficiency:

above the threshold and below I_{max}, the output optical power P_{out} grows almost linearly as a function of the injected current. The linear fit in this current interval gives an estimate of the slope efficiency, i.e. a measurement of how much light power is produced for a unit increase in the current injection. For the case of Fabry-Perot ridge, the slope efficiency SE is defined as:

$$SE = N_p \hbar \omega_{32} \alpha_{m1} \frac{dS}{dJ} \eta_{int} \tag{5}$$

where N_p is the number of periods in the heterostructure, $\hbar$ 32 is the emitted m1 int is the internal quantum efficiency (measuring how many photons are produced by a cascading electron), dS/dJ is the slope of the photon flux with respect to the injected current density J.

- wall-plug efficiency:

it is an overall efficiency, directly relating the optical power from the laser to the total electrical power consumption, due to the current I and bias V required for the laser operation at the maximum emission condition:

$$WP = \frac{P_{out}^{max}}{I_{max} V_{max}} \tag{6}$$

- Threshold current density as a function of temperature:

by operating the laser at different temperatures, it is possible to investigate the thermal management of the structure. Indeed, the thermal dynamics can enchance the non-radiative decay channels by increasing the electron energies, becoming detrimental for the electron population inversion, as well as for the emission of LO phonons. Therefore, the laser threshold condition at increasing temperature can be satisfied only pumping more current in the QCL. This results in an increase of the threshold current density, described by the phenomenological formula:

$$J_{th}(T) = J_1 + J_2 \exp\left(\frac{T}{T_2}\right) \tag{7}$$

where the characteristic temperature T_2 can be retrieved by fitting the experimental trend.

1.2 Waveguide architectures for THz QCLs

1.2.1 Introduction

Light confinement in a QCL is partly provided by the refractive index contrast between the heterostructures and the cladding materials. For a resonating electromagnetic mode with a spatial distribution of the electric field **E**(**r**), the confinement factor is defined as [43]:

$$\Gamma = \left(\int_{AR} |\mathbf{E}(\mathbf{r})|^2 d^3\mathbf{r}\right)\left(\int_{-\infty}^{+\infty} |\mathbf{E}(\mathbf{r})|^2 d^3\mathbf{r}\right)^{-1} \tag{8}$$

which approaches to 1 when the mode is tightly confined in the active material and there is negligible leakage through its cladding and substrate materials.

Conventional ridge waveguides used for Fabry-Perot lasers are characterized by two main loss mechanisms, associated to absorption and scattering in the $_w$) and to the reflectivity of the ridge facets, acting as mirror $_m$. Metallic claddings and/or highly-doped semiconductor layers are implemented in the double-metal or single-plasmon waveguides to confine THz light, exploiting the small penetration depths (for 3 THz radiation, about 30 nm in gold).

1.2.2 Single plasmon resonators

The single-plasmon architecture sandwiches the active material with a top metal layer and a highly-doped bottom semiconductor layer, with a typical thickness

between 200 nm and 800 nm, grown on top a semi-insulating substrate [47]. ^{18} cm^{-3}) is chosen to produce a plasma

below this cutoff frequency, according to the Drude-Lorentz model [56]. The Helmholtz equation for radiation , wavelength and free-space wavevector k_0

$$\nabla^2\mathbf{E} = -\varepsilon(\mathbf{r})\frac{\omega^2}{c^2}\mathbf{E} \tag{9}$$

Due to the slab geometry, the electric field can be written as

$$\mathbb{E}(x,y)e^{\quad}e^{\quad} \quad \mathbb{E}(x,y,z,t)= \tag{10}$$

At the interfaces between the active material and the metallic or quasi-metallic layers, the interaction between the free charges and the electromagnetic wave gives rise to surface plasmon (SP) polaritons [47], which have a propagation constant:

$$k_{SP} = k_0\sqrt{\frac{\varepsilon_d\varepsilon_m}{\varepsilon_d+\varepsilon_m}} \tag{11}$$

where $_d$ $_m$ the one of the metal. Considering that $_m$ $_m|$ and their sign switch between the metal and dielectric regions, k_{SP} is a complex number, indicating that the electric field decays along the z axis (i.e., the growth direction) in correspondence with the metallic or quasi-metallic layers, as shown in figure 1.6. In this model, the associated losses in the single plasmon w

at 3 THz) with respect to mid-IR radiation.
Moreover, even if the field penetrates for some tens of microns in the bottom substrate (see figure 1.7a and 1.7b), the free-carrier absorption losses are limited since the only doped region has a thickness of a few hundred nanometers. This results $^{-1}$ and in a mode and 0.5 for single-plasmon waveguides.

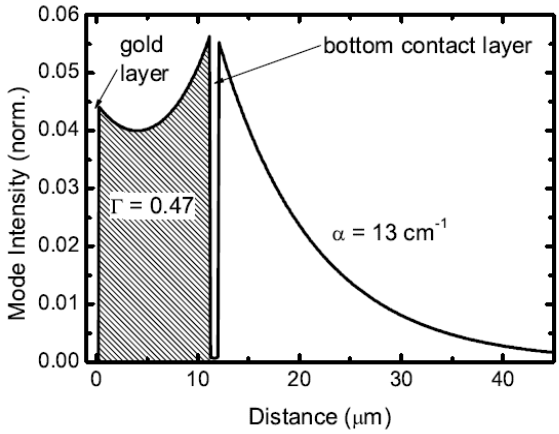

Figure 1.6: Profile of the mode intensity along the growth direction for the single plasmon waveguide used to demonstrate the first THz QCL. Measuring the distance from the top metal layer, the shaded area corresponds to the active region where the mode shows little variation, while below the bottom contact layer, the field penetrates into the substrate with an exponential decay. From [57]

1.2.3 Double-metal waveguides

An alternative waveguide design exploits a second metal cladding, replacing the highly doped bottom layer (figures 1.7c), therefore forcing the electric field to be confined in the active region. This architecture gives rise to slightly higher waveguides losses with respect to single plasmon device $^{-1}$ - 50 cm^{-1}) with the advantage of am uch tighter confinement of the THz radiation along the vertical direction with d. The sub-wavelength confinement helps to limit the threshold current and thermal dissipation, providing good high-temperature performance. Unfortunately, the impedance mismatch between the active material and vacuum at the facet, as well as its sub-wavelength size induce poor radiation extraction to free space, with diffractive effects which significantly affect the emitted beam shape [47].

double metal waveguides is comparable with the one achieved for the single-plasmon design, indicating that both architectures can efficiently confine light.
However, due to the appealing advantages of the double-metal design, a number of approaches have been investigated over the year to address their extraction issues and improve their performance with new waveguide optimization concepts. Indeed, a significant part of the developments of THz QCLs reported in this thesis is based on the photonic engineering of resonators, which is introduced below.

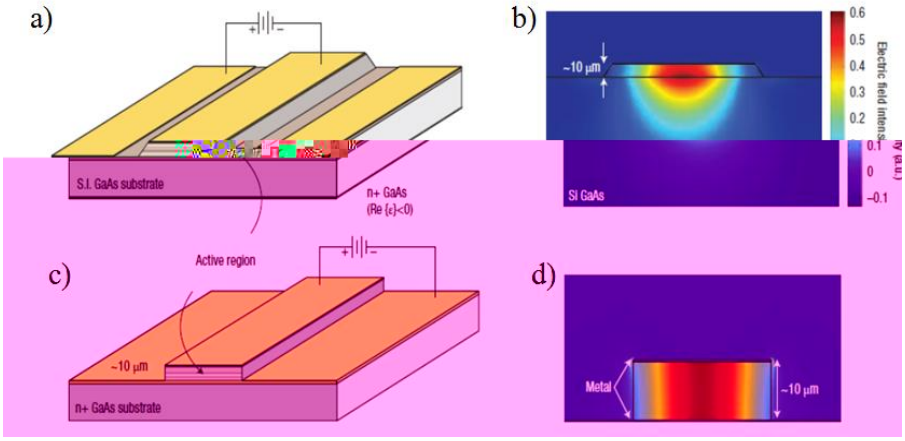

Figure 1.7: a) Schematics of the single plasmon waveguide and b) the simulation of the fundamental THz cavity mode intensity, extending into the substrate. c)Schematics of the double-metal waveguide, for a standard Fabry-Perot laser. d) On the right, the simulation of a THz electric field intensity showing tight light confinement between the top and bottom metal claddings. From [47]

1.3 Terahertz photonic engineering

1.3.1 Distributed feedback resonators

The most conventional resonator geometry for a double-metal THz QCL is the Fabry-Perot (F-P) scheme, implemented by defining cleaved facets which act as mirrors and giving a non-selective feedback for all the frequencies allowed in the resonator. For a cavity with refraction index n and ridge length d, a $_{FSR}$, called free spectral range, exists between adjacent spectral lines [58]. Within the active material bandwidth, the resonating frequencies are

$$\nu_m = m\Delta_{FSR} = m\frac{c}{2nd} \tag{12}$$

with integer index m, as set by the boundary conditions at the reflective facets. The intrinsic multimode emission is therefore determined by the F-P ridge length, though transverse optical excitations are also possible for a sufficiently wide ridge, with little control over the feedback mechanism. This issue can be addressed by introducing a pattern of scattering elements on the top cladding of the double-metal waveguide. The fundamental concept is that this creates a spatial modulation of the refractive index for THz photons, which produce

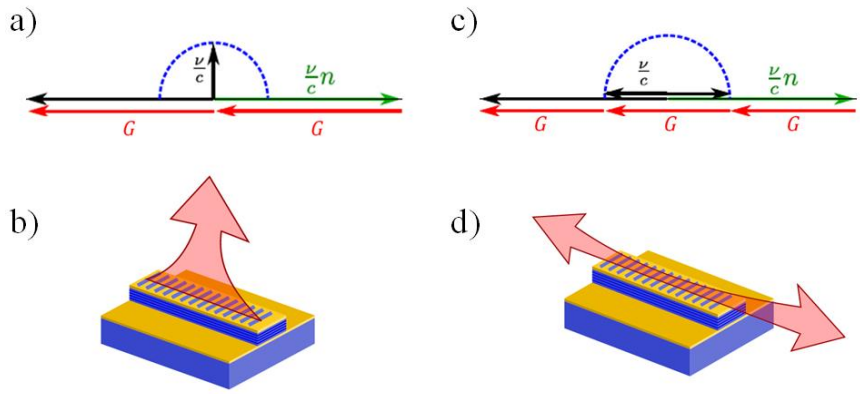

Figure 1.8: a) 1D light-cone diagram for a second-order DFB laser, showing the feedback wavevector G (red line), as well as the backward-propagating (black line) and forward-

laser cavity with refraction index n. As shown in b), the second-order interaction between light and the feedback wavevector results in a zero-sum of the horizontal momentum, matching with the free-space light circle (dotted blue line) to give vertical extraction. c) The light cone representation of the third-order DFB mechanism shows that the free-space coupling condition is achieved in the horizontal direction, as reported in d).

tailored scattering and interference processes to control the emission frequency and direction of the laser beam. Radiation propagating in the resonator undergoes repeated scattering processes along the different spatial positions inside the resonator, which is the core idea of the distributed feedback (DFB) scheme [59]. The simple DFB geometry is created by a one-dimensional sequence of open slits implemented on the top metal surface with a fixed resulting photonic lattice, the main wavevectors which interact with light are associated to the grating harmonics k_m 60] with m = 0,1,2,3... Based on the exploited order m, one-dimensional DFB structures [22,24,25] can be tailored to achieve vertical or longitudinal emission, at a well-defined frequency, by tuning the interaction between the light wavevector and the feedback wavevector by design [61].

material with refractive index n, the first-order DFB scheme exploits a grating . In this way, the complete backscattering condition is realized and the photon direction is inverted, so that it propagates back and forth at a specific resonant frequency. The grating wavevector provides both the feedback and extraction of light to the free space in the longitudinal direction, i.e. parallel to the long side of the laser ridge. A second-order DFB, instead, has a spatial periodicity such that the scattering vector is G

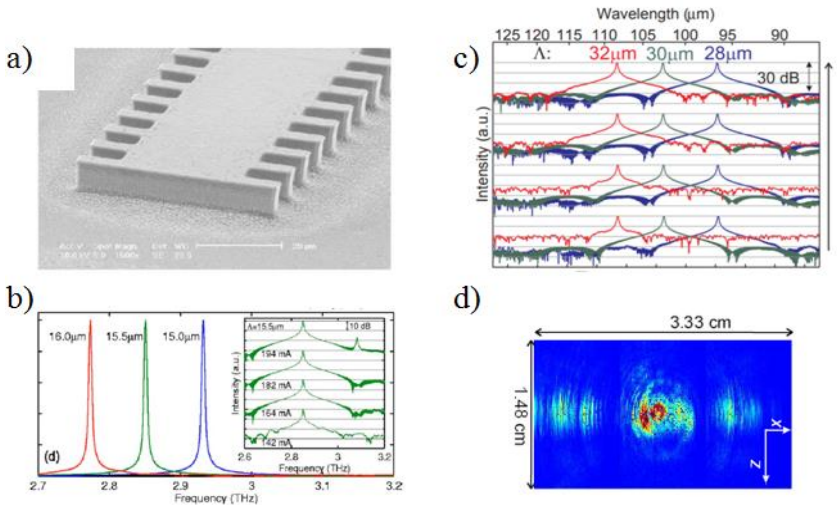

Figure 1.9: a) SEM image of first-order DFB THz QCL exploiting a periodic lateral corrugation to ensure the desired modulation of the refractive index modulation and provide longitudinal light extraction, from [22]. b) Emission spectra of first-order DFB lasers showing robust single-mode emission, from [22]. c) Single-mode FTIR emission spectra of second-order DFB THz QCLs with different grating periodicities, from [24]. d) Beam intensity profile for a second-order DFB laser, from [24].

shown in the light-cone diagram in figure 1.8a, a double interaction of the photon wavevector with the grating one results in a zero horizontal momentum, corresponding to a matching with the free-space light vector in the vertical direction. Therefore, second-order DFB lasers provide surface emission in the vertical direction, orthogonal to the top metal layer (see figure 1.8b). -order

The photon propagation along the ridge is reversed upon three scattering events with G as shown in figure 1.8c, so that light is finally extracted in the longitudinal direction (see figure 1.8d). The sequence order can further be progressively increased following the rationale described above.

An example of a first-order DFB THz QCL reported in [22] is based on a periodic lateral modulation of the laser ridge width (figure 1.9a), which, in turn, creates a periodic variation of the refraction index seen by the photons in correspondence with the narrow and wide cross-section regions. The resulting laser spectra show that the geometry gives a robust mode selection, with the single emission frequency varying accordingly to the different implemented periodicity (figure 1.9b). Figure 1.9c reports the single-mode emission spectra of second-order DFB THz QCLs with different periodicities [24], based on a

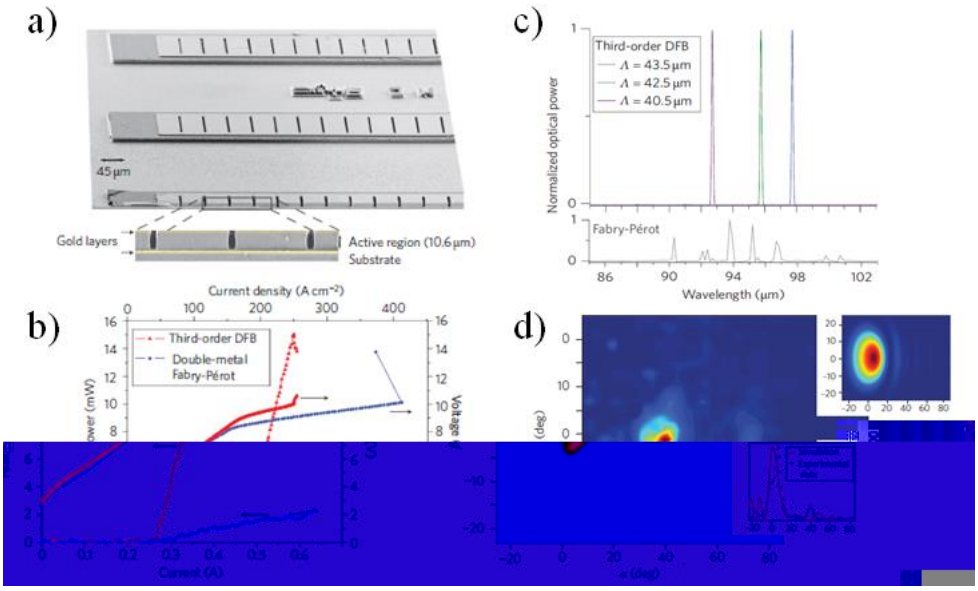

Figure 1.10: a) SEM image of third-order DFB THz QCLs with the detail of the slit grating in the inset. b) Comparison of the LIV characteristic of a DFB laser and a conventional Fabry-Perot device with the same material and comparable size. c) Single-mode FTIR emission spectra of DFB devices with different grating periodicities (top), compared to the multimode emission of a Fabry-Perot device (bottom). d) Far-field intensity profile for an effective index of 3.5, compared to the simulated bem divergence in the inset. All panels are from [25]

sequence of air slits opened in the top metal waveguide to provide feedback and vertical extraction of the laser beam (fig. 1.9d). The experimental realization of a third-order DFB resonator [25] based on a slit grating (figure 1.10a) required a demanding micro-fabrication accuracy to achieve the effective refractive index needed to fulfill the third-order scattering condition. Indeed, a careful deep etching of the semiconductor below the slits was needed to reduce the effective index of the structure to n = 3, starting from a GaAs-based

demonstrated an optimized light outcoupling significantly improving the efficiency and the optical power with respect to a standard Fabry-Perot device with same material and size (figure 1.10b), while the resonator geometry ensured single-mode emission on a frequency dictated by the chosen DFB period (figure 1.10c). Interestingly, the fine tuning of the lithographical parameters and the etching process allowed reaching a very narrow beam divergence in the longitudinal direction for this edge-emitting devices (figure 1.10d).

1.3.2 Photonic crystals

The described periodic one-dimensional DFB THz resonators belong to the larger family of photonic crystals (PCs), based on a regular repetition of scattering elements in one-dimensional, two-dimensional and three-dimensional systems. The associated spatial distribution of the dielectric function is considered constant in the frequency range of interest and has a discrete translational invariance, such that:

$$\varepsilon(\mathbf{r}) = \varepsilon(\mathbf{r} + \mathbf{R}) \tag{13}$$

where **R** is a linear superposition of integer multiples of the fundamental lattice vectors $\mathbf{v}_1$, $\mathbf{v}_2$, $\mathbf{v}_3$, which define the unit cell of the crystal. Such modulated distribution is physically implemented by arranging a number of scatterers in the positions indicated by a subset of the crystal vectors. In analogy with the Bloch theorem used in solid-state physics, the electromagnetic fields in a PC can be investigated by decomposing the magnetic field modes as [62]:

$$\mathbf{H}_{n,\mathbf{k}} = \mathbf{u}_{n,\mathbf{k}}(\mathbf{r})e^{i\mathbf{k}\mathbf{r}} \tag{14}$$

where $\mathbf{u}_{n\mathbf{k}}$ **r**) and the wavevector **k** belongs to the reciprocal lattice. By imposing periodic boundary conditions, the study of Maxwell's equations can be restricted to the PC unit cell, leading to the eigenproblem:

$$\nabla \times \left[\frac{1}{\varepsilon(\mathbf{r})}\nabla \times \mathbf{H}(\mathbf{r})\right] = \left(\frac{\omega}{c}\right)^2 \mathbf{H}(\mathbf{r}) \tag{15}$$

which can be solved to retrieve the angular **k**) of the resonating eigenmodes for each value of **k** , with the constraint:

$$(i\mathbf{k} + \nabla) \cdot \mathbf{u}_{n,\mathbf{k}}(\mathbf{r}) = 0 \tag{16}$$

k) are continuous functions of **k** and periodic for translations by a reciprocal vector **K**. The redundant wavevectors can be eliminated by folding the band structure in the first Brillouin zone (BZ) of the reciprocal $_n(\mathbf{k})$ with the band index n. Exploiting the periodicity of the system in both the real and reciprocal space therefore helps to simplify the computations, by reducing the domain size required for numerical solutions. A realistic investigation of a PC resonator should also include the losses and the light outcoupling to the free space, which give complex values of

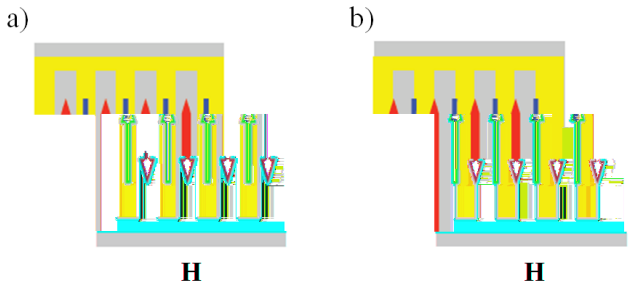

Figure 1.11: a) Diagram of the magnetic field spatial distribution, highlighting the positive intensity peaks (blue arrows) and negative ones (red arrows) in the case of a symmetric mode. b) Distribution of the positive and negative intensity peaks of the magnetic field, for an anti-symmetric mode.

the eigenfrequencies accounting for the typical mode lifetime:

$$\nu = \frac{\omega_0 - i\delta}{2\pi} \tag{17}$$

from which the associated quality factor can be retrieved:

$$Q = \frac{\omega_0}{2\delta} \tag{18}$$

The computed overall quality factor includes the different decay channels, associated to the material losses (in particular in metal and doped regions), as well as the extraction of light outside the resonator, mimicking the propagation of a laser beam. The light extraction is usually characterized by defining a rad obtained integrating the near-field Poynting vector over a surface S enclosing the resonator and dividing by the electromagnetic energy stored in the cavity volume V_A:

$$\gamma_{rad}(\nu) = \frac{1}{\tau_{rad}(\nu)} = \frac{2}{\varepsilon_0} \frac{\int_S (\mathbf{E} \times \mathbf{H^*}) \cdot \hat{n}\, dS}{\int_A (\varepsilon_r |E|^2 + Z_0^2 |H|^2)\, dV_A} \tag{19}$$

0 r is the relative permittivity of the active material, and Z_0 is the vacuum impedance. Electromagnetic modes with high Q form standing waves with long lifetime, having a strong coupling with the active material which makes them favored for laser action with respect to low-Q modes.[63] In a perfectly periodic PC, the electromagnetic eigenmodes have an inherent symmetry or anti-symmetry with respect to the photonic pattern of scattering elements, which in turn affects their confinement and quality factor. As reported in figure 1.11a for the simple case of a one-dimensional slit grating,

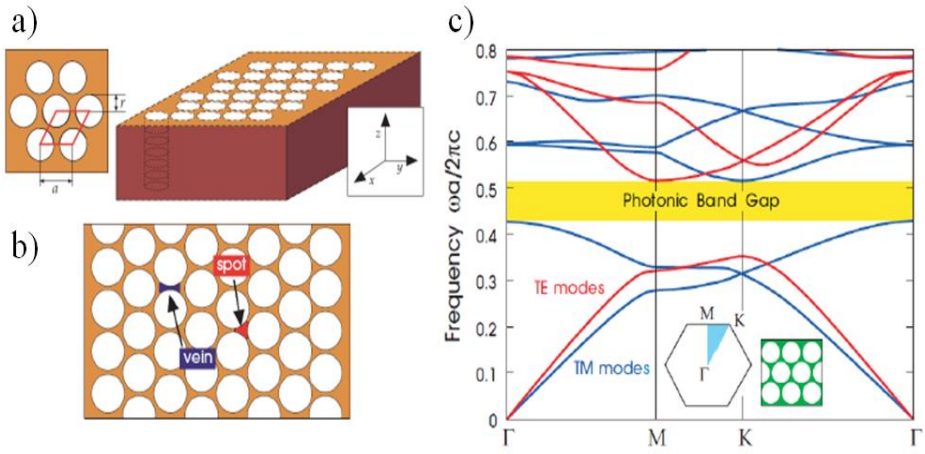

Figure 1.12: a) Unit cell of a triangular photonic crystal formed by an array of air columns (n = 1), surrounded by a material with refractive index n = 3.61. The air cylinders have radius r and lattice constant a, corresponding to a filling factor r/a = 0.48. b) Top view of the structure with the indications of the dielectric spots between three near columns connected by narrow veins. c) Photonic band structure showing a complete band gap for both TM (blue) and TE (red) modes, computed in the irreducible Brillouin zone in blue in the inset. All panels from [63].

the symmetric spatial profile of a magnetic eigenmode **H** has maxima and minima in correspondence with the open slits and the metal strips, respectively. This means the field is well coupled to free space and is "radiative", with a poor confinement and a correspondingly low Q, which makes the amplification of the mode less efficient. Conversely, an anti-symmetric mode (figure 1.11b) has maxima and minima of **H** at the edges of the open slits, featuring lower radiative losses and higher Q which favors lasing. Unfortunately, the opposite sign of the field at these points creates destructive interference in the far field, limiting the light extraction and making the mode "non-radiative". In both cases, a power extraction issue is intrinsically present due to the structure geometry. Moreover, high-quality factors in a PC correspond to a small group velocity for the mode, which is a typical feature of modes lying at the edge of the photonic bandgaps. Figure1.12a reports the example of two-dimensional PC featuring a triangular unit cell, made up by an array of air holes drilled across a dielectric material. This results in a spatial modulation formed by a series of narrow veins and large spots with high refraction index alternating with the low-index air pillars (figure 1.12b). The scattering properties of the system are strongly dependent on the pillar radius r and the crystal period a, which are summarized by the filling factor parameter r/a. This specific geometry produces

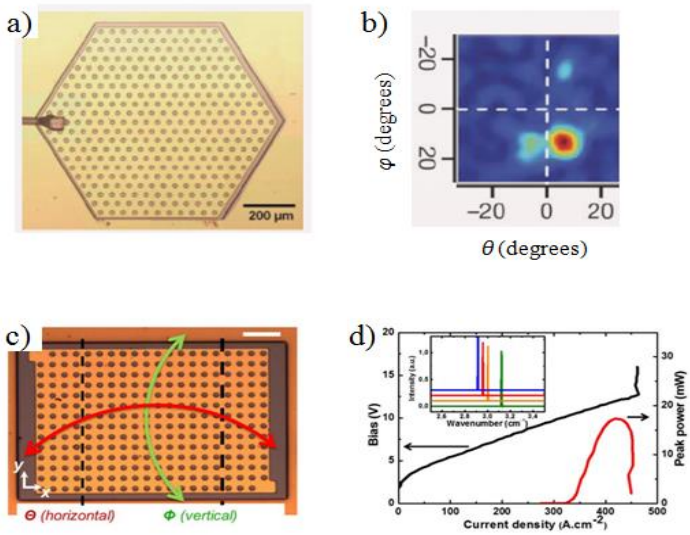

Figure 1.13: a) Microscope image of a triangular photonic crystal THz resonator and b) the associated emitted far-field profile from [26]. c) Microscope image of a square photonic lattice -mode emission (see inset), from [64]

a photonic band structure computed over the BZ domain, showing there is a forbidden frequency region (i.e., photonic bandgap) where no state exists for any reciprocal wavevector, for both TM and TE light polarization (figure 1.12c). Figure 1.13a shows a two-dimensional PC THz QCL with a triangular pattern of holes in the top metal layer of the device, surrounded by highly doped boundary domain which suppresses the fields extending to the edge of the resonator.[26] In this way, only the modes strongly coupled with central PC region are available for laser action: the emission frequency and far-field pattern (figure 1.13b) can be varied by setting distinct r/a parameters. A two-dimensional PC THz resonator exploiting a square array of holes is shown in figure 1.13c, which was actually engineered to emit on the radiative, normally low-Q modes by adding a slight anisotropy in the lattice [64]. Indeed, a rectangular unit cell was devised to alter the mode competition between radiative and non-radiative fields, achieving single-mode emission with a significant maximum power of about 17 mW (figure 1.13d). This is an indication that the power limitations of THz photonic crystal resonators can be addressed by the development of novel waveguide architectures which violate the spatial symmetry and perfect periodicity, while simultaneously tailoring the emission spectrum and beam profile.

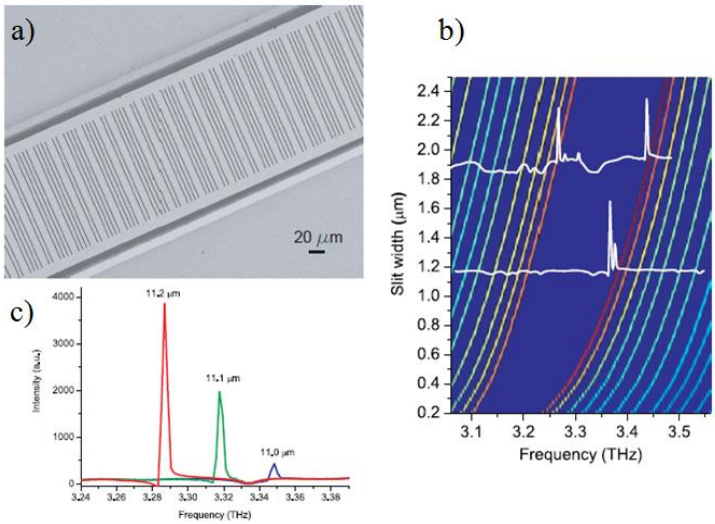

Figure 1.14: a) Scanning electron image (SEM) of a Fibonacci THz QCL, showing the aperiodic distribution of the slits in the top metal grating. b) Calculation of the resonating frequencies around the bandgap of a Fibonacci resonator with fixed quasi- and slit width varied between 0.2 µm and 2.5 µm. Experimental emission spectra are superimposed for resonators with different slit widths of 1.1 µm and 1.8 µm (with offset matching their slit width). c) FTIR emission spectra of Fibonacci devices with different quasi- From [69]

1.3.3 Photonic quasi-crystals

A photonic quasi-crystal is a system with an aperiodic spatial modulation of the dielectric function (or, equivalently, of the refractive index), dictated by a deterministic generation rule.

A quasi-crystal is mathematically built by the infinite repetition of two or more distinct unit cells [65,66], forming an irregular lattice at the sites $\mathbf{R}_i$ with long-range order and no discrete translational invariance, unlike crystals. Different deterministic algorithms have been developed to generate a number of quasi-crystal geometries, such as the generalized dual method, the inflation rules and hyper-dimensional projections. The implementation of a photonic quasi-crystal relies on the positioning of scattering elements in the resonator, such as slits or holes, in correspondence with the quasi-lattice vertices. A quasi-crystal features orientational order, minimal separation between adjacent lattice vertices, and quasi-periodic translational order. These properties are encoded in the quasi-crystal structure factor:

$$S(\mathbf{k}) = \lim_{N\to\infty} \frac{1}{N} \sum_i e^{i\mathbf{k}\cdot\mathbf{R}_i} \tag{20}$$

which is summed over all the lattice vertices. S(**k**) is analogous to the reciprocal space representation of crystals, and provides an indication of the Fourier component intensity associated to the wavevectors. The Fourier spectrum of quasi-crystals is typically much richer than that of crystals, being singular-continuous, i.e. for every two peaks of S(**k**) there is always a third wavevector in-between [67]. The scattering processes of photons with the rich wavevector spectrum results in complex interference patterns which determine the resonating electromagnetic modes, often featuring photonic pseudo-bandgaps. The simulation of such resonators is much more demanding than for conventional PCs and it is not possible to properly define a photonic band structure, since all the assumptions associated to the periodic boundary conditions do not hold anymore.

Figure 1.14a shows a one-dimensional quasi-crystal slit grating employed as a DFB resonator based on the Fibonacci sequence [29,68], which is built starting from two elements A, B with lengths L_A and L_B respectively. The next elements are obtained by applying the substitution rule: A AB and B A. The nth-order Fibonacci sequence contains a number n_A of A elements and n_B of B elements, with a ratio n_A/n_B that approaches the golden mean for n

$$\lim_{n\to\infty} \frac{n_A}{n_B} = \varphi = \frac{1+\sqrt{5}}{2} = 1.618... \tag{21}$$

Setting the characteristic Fibonacci lengths to $L_A = L_B$, a distribution of open rectangular slits are defined on the top metal surface of a THz QCL, with a quasi- L_A. By tuning the geometrical parameters of the grating, it is possible to manipulate the feedback and scattering processes and control the resonating frequency of the high-quality-factor modes, which indeed vary with the slit width as shown in figure 1.14b around a 140 GHz-wide pseudo-bandgap. Figure 1.14c reports the laser emission spectra, showing a clear shift of the single-mode emission frequency as a consequence of the different

est case, the peak optical power reached a maximum value of about 6 mW, corresponding to a

The quasi-crystal concept has been recently extended to two-dimensional aperiodic THz resonators, investigating the optical performance of double-metal THz QCLs integrating patterns of holes based on a 5-fold Penrose scheme [30] and a 7-fold quasi-periodic scheme [31]. The scattering processes in such

resonators are controlled by geometrical parameters such as the average inter-site distance of these patterns, a, and the hole radius, r, which give the quasi-crystal filling factor r/a. A photon propagating in such two-dimensional pattern undergoes multiple in-plane elastic scattering with the wavevectors $\mathbf{G}_i$ in the reciprocal quasi-lattice having larger Fourier intensity. Standing waves build up from a complex interference pattern when the multiple scattering with the photon wavevector in the active material satisfies the condition [69]:

$$\sum_i \left[\mathbf{k}_P - \mathbf{G}_i\right] = 0 \tag{22}$$

This selects the eigenmodes with highest quality factors, which are favored for laser amplification, determining the extraction power, emission frequency and far-field profile of the device as a function of the hole pattern. Figure 1.15a shows a scanning electron microscope (SEM) image of a Penrose resonator -rotational invariance [30], which reached a maximum peak optical power of 65 mW at 10 K, and nicely a beam divergence comprised within a 10° ring (figure 1.15b).

Alternatively, one can exploit the quasi-crystal concept to engineer broad multimode emission in THz QCLs highly desirable for spectroscopic applications. Figure 1.15c reports the image of a quasi-crystal THz QCL with a -rotational invariance [31], providing multimode emission over 430 GHz with peak output power > 60 mW and beam divergence below 15° (figure 1.15d). By varying the degree of disorder one can tune the emission spatial and spectral properties as shown in figure 1.15e, with a device featuring defect -rotational symmetry, resulting in a less collimated laser beam (figure 1.15f).

The worst drawback of the presented architectures is the large dissipation of power caused by the resonator geometry, which results in extremely low wall-plug efficiencies. In particular, 1D architectures offer intriguing perspectives to tailor the resonator internal and external quantum efficiencies, which is the objective of this thesis. In this respect, two non-periodic one-dimensional DFB resonators schemes were developed and investigated:

- a laterally corrugated wire laser with a hole array in the top metal layer, achieving independent control over the feedback and extraction mechanism, as reported in Chapter 2 [40]

- a one-dimensional quasi-crystal DFB grating exploiting the photonic pseudo-bandgaps to control the emission spectrum and far-field profile, as reported in Chapter 3 [41]

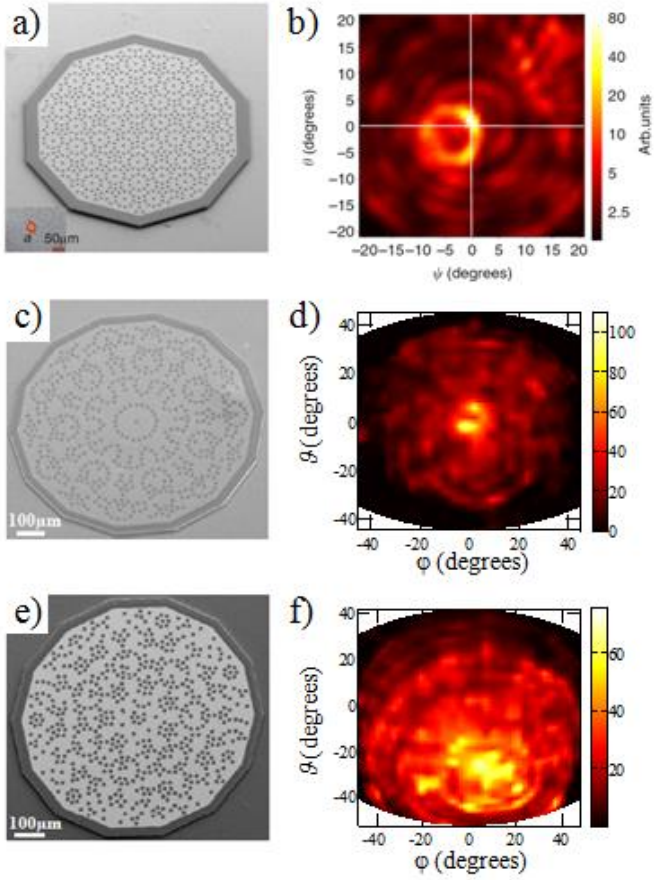

Figure 1.15: a) SEM image of a 5-fold Penrose quasi-crystal THz QCL, with an associated far-field profile reported in b) from [30]. c) SEM image of a 7-fold quasi-crystal resonator with perfect discrete rotational symmetry, with the narrow beam divergence in d), from [31]. e) SEM image of a 7-fold quasi-crystal resonator with defect points breaking the rotational invariance, with an associated far-field profile in f), from [31].

1.3.4 Random lasers

Among aperiodic resonator designs, random lasers represent a very peculiar system. Even if a random laser requires an active material to amplify light like any conventional laser, it actually does not have a properly defined optical cavity to provide the feedback mechanism. Instead, it fully relies on the multiple elastic scattering of the photon propagating across a material with a

completely irregular profile of the dielectric function, which preserves the phase relationship of the light wavelets. [70]

This complex interference scheme determines both the spatial profile and the frequency of the electromagnetic radiation in the random material, determining the degree of localization of the resonating modes. Such systems are inherently multimode and can support both extended modes and localized modes [71], which are the optical counterpart of the Anderson localized electron wavefunctions. In this regime, light is trapped by a highly disordered medium, with a strong spatial confinement and long lifetime, forming a standing wave with a random spatial profile of the electromagnetic intensity. Anderson localization of light is more likely in systems with low dimensionality, such as one-dimensional or two-dimensional structures, which offer a higher probability of light scattering in closed paths. [72] Since the intrinsic structural disorder of a random material combines with the non-linear phenomena typical of the laser gain medium, such as wave mixing and mode competition [73-76], the description and modeling of the random lasing dynamics in the different regimes is still debated.

The statistical spatial correlation of a randomly **r**) is defined as an ensemble average [76]:

$$K(\Delta\mathbf{r}) = < \varepsilon(\mathbf{r})\varepsilon(\mathbf{r}+\Delta\mathbf{r}) > \quad (23)$$

r in an isotropic medium. The resulting characteristic length, called correlation radius R_c, **r**) with respect to the $_c$ -range disorder is dominant, while in the opposite case the long- **r**). The propagation of light in such a structure is characterized by the scattering mean free path l_s, i.e. the average distance covered by a photon between two successive scattering events, and by the transport mean free path l_t, i.e. the typical distance over which the direction of the photon wavevector is randomized. These lengths are connected by the expression

$$l_t = \frac{l_s}{1 - \langle \cos\theta \rangle} \quad (24)$$

transport free path in a the characteristic linear size of the system L to identify the type of light propagation.

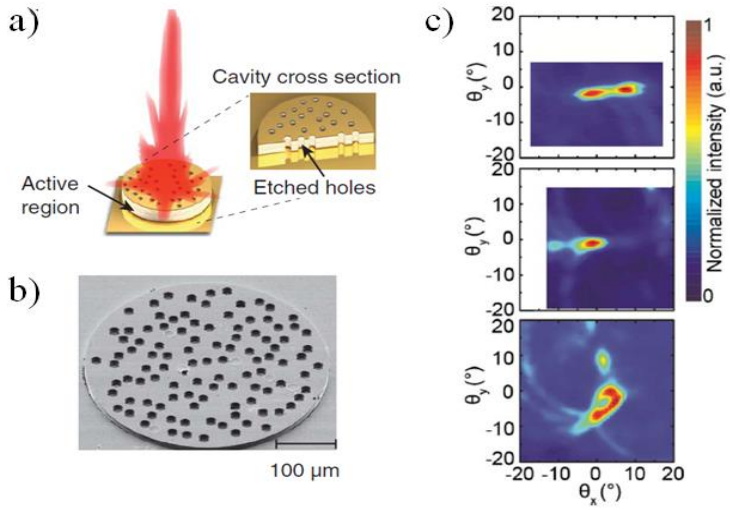

Figure 1.16: Schematic drawing of a surface-emitting circular random THz, with the completely drilled holes shown in the cross-section inset image. b) SEM image of random THz QCL. c) Far-field profiles emitted from devices with different geometric patterns. All panels from [32].

For a mode with wavevector **k**, the following regimes are possible:

- for l_t
- $_t$ << L: light can be described with a diffusion model
- for $|\mathbf{k}|l_t$ (Ioffe-Regel criterion [77])

Depending on the specific system and its degree of disorder, a random laser operates on modes which obey Maxwell's equations and have a complex spatial profile due to the multiple scattering and interference processes. Coherent emission from localized as well as extended modes is possible, resulting in in multimode spectra which can be classified in two types, which can possibly coexist in one laser [78]:

- the "resonant feedback random lasing" (RFRL) produces few sharp, uncorrelated spectral peaks, which can be interpreted as modes with little spatial overlap and relatively high quality factors
- the "incoherent feedback random lasing" (IFRL) features a smooth and broad single-peak spectrum, due to the interaction between modes with significant overlap at close frequencies, explained in a diffusion approximation picture.

Random lasing has been demonstrated in a variety of systems and spectral regions,[79-81] including mid-IR [82] and THz QCLs [32-34]. Figure 1.16a reports the schematic design of a circular THz QCL resonator patterned with a

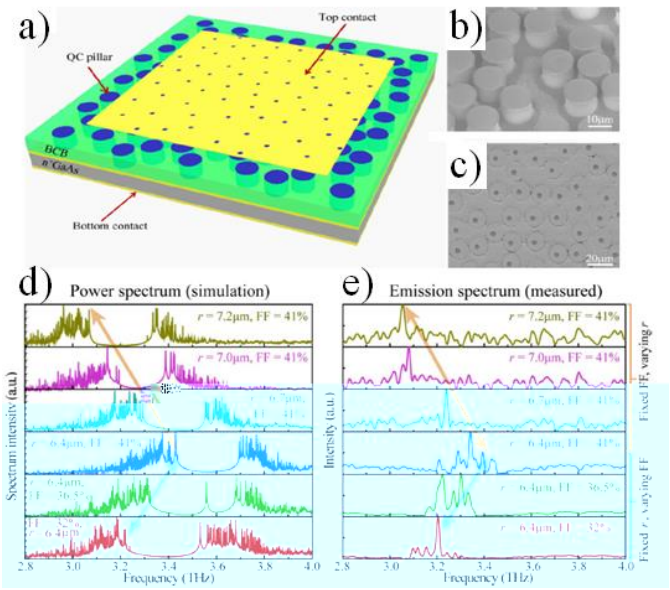

Figure 1.17: a) Diagram of the random semiconductor pillars (blue) embedded in a polymer layer (green) and covered by a top metal layer with holes in correspondence with the pillars. SEM images of the pillars in b) and of the holes in c). d) Simulated power spectrum indicating the presence of a photonic bandgap varying with the geometric parameters. e) Multimode FTIR emission spectra confirming that the emission peaks shift with the geometry design in agreement with simulations. From [33].

series of randomly distributed holes in the top metal surface [32] to provide surface light extraction. The holes are deep-etched to from air pillar across the whole heterostructure thickness (figure 1.16b). By varying the radius of the air holes, r, and their inter-site distance, a, two-dimensional geometries with different filling factor r/a were investigated, achieving a maximum power thermal management of the large device. Figure 1.16c reports some far-field intensity profiles emitted by devices with different r/a, showing a quite irregular beam spot in most cases. As shown in figure 1.17a, an alternative approach to achieve random lasing in a double-metal THz QCL exploits semiconductor pillars [33] obtained by etching most of the active material away. These pillars (figure 1.17b, 1.17c) are surrounded by a resin having low losses and low refraction index at THz frequencies, which helps inducing localized modes in the resonator. For these two-dimensional geometries with different r/a, a photonic pseudo-bandgap is revealed by simulations (figure 1.17d). Multimode emission spectra are indeed in good agreement with the numerical predictions, as visible

in figure 1.17e. However, in the described cases, operation has been reported only at low duty cycles (up to 4%) and at very low operating temperatures (5 K), due to poor thermal management. Indeed, large device areas are required in these architectures, to ensure that there is sufficient gain in the radiative optical modes following fabrication of the deep-etched pillars. The novel random laser developed in this thesis consists in a disordered distribution of holes patterned in the top metal layer of a double-metal THz QCL, surrounded by irregular borders to confine the active region while suppressing undesired modes extending to the device edges. Patterning of the holes is implemented only in the upper gold cladding and in the highly-doped semiconductor layer, so that the useful active region core is left unperturbed. We thus overcome the previous technological thermal and power limitations of THz RLs, enabling us to demonstrate the first multimode CW emission.

In this thesis, Chapter 4 is dedicated to the numerical and experimental investigation of random THz QCLs, which were designed to achieve CW operation and provide broadband spectra [42]. Moreover, in Chapter 5 the manipulation of the emission of fabricated random lasers is detailed, exploiting the interaction and feedback between the emitted mode and the optical response of multilayer graphene samples.

CHAPTER 2:
SINUSOIDAL CORRUGATED WIRE LASER

2.1 Introduction

This chapter details the design, fabrication and test of DFB lasers exploiting a novel concept for geometrically decoupling the feedback from the light outcoupling. This resonator architecture is based on the superposition of two one-dimensional photonic structures with different periodicities: a lateral sinusoidal modulation of the ridge width, and an array of top holes lithographically imprinted on the top metal surface of the device. By carefully tuning the grating periodicities providing a distributed feedback (DFB) mechanism for laser light, it is possible to optimize the matching between the guided mode and the externally propagating photons, generating a collimated beam from the laser surface by interference.

Before introducing the aperiodic design concept, it is useful to analyze the physical properties of periodic photonic systems. In a conventional one-

tailored on the fundamental (m = 1) spatial harmonics k_1

while optical feedback inside the resonator is provided by a wavevector with k_m

-dimensional

DFB structures [24,25,83] can be engineered to provide directional emission over a specific plane, governed by the interaction between the light wavevector and the feedback wavevector [61]. In these architectures, external quantum efficiency, beam shaping, and mode control are related to the extraction of symmetric and anti-symmetric resonant eigenmodes. In general, symmetric modes produce constructive interference in the far-field and have efficient outcoupling into the free space. In contrast, anti-symmetric modes interfere destructively in the far-field, but have lower loss. As such, anti-symmetric modes are favored for lasing, but consequently provide limited extraction power.

A number of photonic approaches have been explored so far to circumvent these intrinsic limitations, while still ensuring directional beam profiles. These include vertically emitting graded photonic heterostructures [84,85], quasi-periodic gratings [29], and double-periodicity DFB gratings, engineered to achieve a simultaneous tailoring of the emission frequency and a tuning of the beam direction, via the independent control of the extraction and feedback

wavevectors [28]. Further approaches have utilized on-chip phased locked arrays [86,87] and metasurface reflectors, which comprise multiple cavities [88], and induce directional THz QCL emission in pulsed operation.

In contrast to surface-emitting approaches, edge-emitting structures with narrow cavity widths are potentially more suited for applications in sensing, spectroscopy or metrology due to the lower electrical power dissipation, which better enables continuous-wave (CW) operation. In-plane emitting wire lasers exploiting third-order DFB gratings [87,89,90], and including integrated micro-antennas, [91] are the most exploited solutions in this respect. Despite the clear advantages in the emission profiles (10° divergence) [87,90] and slope efficiencies (120 mW/A) these approaches show a number of challenges. In particular, these devices require sophisticated waveguide engineering that constrains the effective mode index to n = 3, i.e., the grating order, but this is significantly smaller than that of the GaAs/AlGaAs active region (n = 3.56). The lithographic phase matching procedure then becomes demanding if a repeatable and robust fabrication process has to be realized. Alternatively, in-plane emitting antenna-feedback plasmonic lasers [92] have been recently proposed to deliver good beam shaping (4° divergence), but these have limited power extraction (1 2 mW) in pulsed operation. In the present thesis activities [40], we demonstrate double-metal waveguided DFB THz quantum cascade wire lasers, exploiting an innovative approach in which feedback is provided by a lateral sinusoidal ridge corrugation, while light extraction is separately controlled by a hole array in the top metallization. In this case, the periodicity of the array of surface holes is not an integer multiple of the lateral corrugation controlling the feedback. The feedback grating selects the lasing frequencies and allows robust single-mode emission, exploiting the inherently high spectral purity of THz QCLs [93], while the extraction array is finely tuned to optimize the radiation outcoupling. This architecture thereby simultaneously addresses the challenges of low-divergence, single-mode emission, high power, large slope efficiency, while preserving the thermal management to ensure robust CW operation.

2.2 Periodic sinusoidal corrugation resonator

2.2.1 One-dimensional light-cone scattering diagram

Let us consider a very narrow and thin cavity (with respect to the desired

laser". The cavity is designed to have a sinusoidal modulation of the width along the light propagation direction (here defined along the x-axis). Due to the narrow size of the cavity along the y-axis and z-axis, the resonator is substantially a 1D photonic system which provides a distributed feedback (DFB). The traditional mirrors of a Fabry-Perot are replaced by a structure based on a refractive index modulation spread all over the system, inducing the needed reflection and interference scheme to control light.

-

be designed with a length of a few millimeters along the x-axis. It also features a sinusoidal lateral corrugation, creating a width modulation
with a spatial feedback periodicity
(figure 2.1).

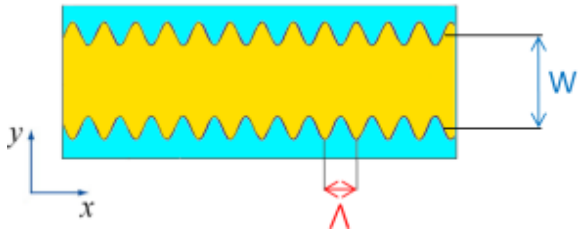

Figure 2.1: Sinusoidal lateral corrugation of the wire laser width W, with a spatial feedback periodicity

Indeed, by changing the width of the wire laser, we can modify the behavior of the electromagnetic field, which is squeezed in the periodically narrower and larger cross-section of the resonator. In practice, this creates a spatial modulation of the dielectric function for the resonating mode, having an average refractive index n_{eff} within a one-dimensional model, which can be numerically estimated studying the transverse propagation of waves in the ridge cross-section.[94]
A first, rule-of-thumb approach to the design of such a sinusoidally corrugated wire laser, requires two main information:

- the target emission frequency
- the expected effective refractive index n_{eff}

modulation since the associated wavevector k_{fb} needs to be properly tuned to interact with the light wavevector in the active material with modulus
n_{eff} . As shown in figure 2.2, radiation propagating in the forward direction (green arrow) needs to be back-scattered by the feedback wavevector (red

arrow), so that light travels in the opposite direction along the cavity (blue arrow). This establishes the proper feedback which drives photons back and forth across the wire laser.

Figure 2.2: A simple 1D model of the scattering process which makes forward propagating light (green arrow) bounce back in the opposite direction (blue arrow),

quantum cascade lasers). In order to highlight its Fourier components, this function can be rewritten as:

$$\varepsilon(x) = \varepsilon_0 + \frac{\varepsilon_d}{2i}\left[e^{i(2\pi x/\Lambda)} - e^{-i(2\pi x/\Lambda)}\right] \quad (28)$$

Even if the describes an infinitely long system, it can be reduced to a much

idea is that the electric field is itself periodic according to the geometry, i.e. , so there is no need to actually solve the problem for an infinite cavity. Therefore tools like the Bloch theorem and the Brillouin Zone reduction can be applied. In particular, the wavevectors corresponding to propagation along the x-axis are therefore limited to the reciprocal space domain k ∈]- . Any other wavevector outside this region can be obtained by a translation of the type k for m = ±1, ±2,

Unlike more disordered systems, all these conditions greatly simplify the solution of the electromagnetic problem which reduces to the form of the Helmholtz equation. The TM-polarized electric field (along the z-axis) can be written as a Fourier series:

$$E(x) = \Re\left[\sum_m E_m\, e^{i\left(k+m\frac{2\pi}{\Lambda}\right)x}\right] \quad (29)$$

introducing the complex Fourier coefficients E_m. Using the sinusoidally modulated and the Fourier expansion of E(x), the specific Helmholtz equation can be derived:

$$\left[\left(k+\frac{2\pi}{\Lambda}m\right)^2 - \varepsilon_0\frac{\omega^2}{c^2}\right]E_m + \frac{\varepsilon_d}{2i}\frac{\omega^2}{c^2}E_{m+1} - \frac{\varepsilon_d}{2i}\frac{\omega^2}{c^2}E_{m-1} = 0 \quad (30)$$

whe

re is the angular frequency of the electric field satisfying the equation. Since only contains the harmonics , the resulting master equation couples each electric field component E_m with those having order m ± 1. The objective is using this system of equations to retrieve a formula which gives of the allowed field, as a function of the wavevector k and for different orders m. A numerical solution can be implemented in a programming language such as Python or Matlab, associating at each k value the corresponding frequency . This directly provides the dispersion relation

for the sinusoidally modulated wire laser. Some important physical information can be retrieved by solving the problem at some specific values, such as the edge of the Brillouin zone k = for the order m = 0. In the case of a small dielectric modulation $_d << _0$ and neglecting the interaction with the (m+1)-order, this perturbation approach gives two combined equations:

$$\begin{aligned} -\frac{\varepsilon_d}{2i}\frac{\omega^2}{c^2}E_{-1} + \left[\frac{\pi^2}{\Lambda^2} - \varepsilon_0\frac{\omega^2}{c^2}\right]E_0 = 0 \\ \left[\frac{\pi^2}{\Lambda^2} - \varepsilon_0\frac{\omega^2}{c^2}\right]E_{-1} + \frac{\varepsilon_d}{2i}\frac{\omega^2}{c^2}E_0 = 0 \end{aligned} \tag{31}$$

Based on standard methods of linear algebra, non-trivial solutions to the above equations are those giving a system determinant equal to 0. As a result, there are two permitted angular frequencies at the Brillouin zone edge:

$$\omega_\pm = \frac{\pi c}{\Lambda}\frac{1}{\sqrt{\varepsilon_0 \mp \varepsilon_d/2}} \tag{32}$$

The larger angular frequency belongs to the upper band-edge mode, while the smaller frequency belongs to the lower band-edge mode. In between these two angular frequencies, no other modes are permitted so this forbidden spectral

center frequency of the bandgap is:

$$\nu_{NOT} = \frac{\nu_+ + \nu_-}{2} = \frac{c}{2\Lambda}\frac{1}{\sqrt{\varepsilon_0}} \tag{33}$$

which is perfectly consistent with the result obtained with the 1D wavevector scattering model. As expected from that simple representation, the target frequency is determined by the average refractive index, given by $_0$. The difference between the upper and lower frequency gives the width of the bandgap, which is proportional to the dielectric modulation depth $_d$:

$$\frac{\Delta\nu}{\nu_{NOT}} = \frac{\varepsilon_d}{2\varepsilon_0} \tag{34}$$

and directly linked to the cavity width W

$_d$, producing a wider frequency bandgap. As shown in figure 2.3, both the upper and lower band-

-edge mode has maxima and minima in phase with the wire laser corrugation, while the upper band-edge mode has maxima and minima in counter-phase with it.

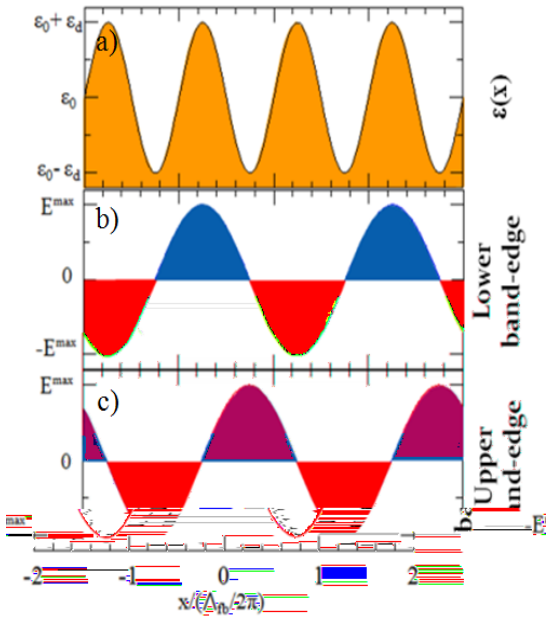

Figure 2.3: a) Spatial profile of is shown. b) Plot of the lower band-edge mode profile as a function of x for a frequency . c) Plot of the upper band-edge mode profile as a function of x for a frequency +.

In other words, the mode at the lower frequency tends to spread covering the

more concentrated in the thinner part, with a size of W-

numerical solution to the Helmholtz equation for the sinusoidal corrugation gives the dispersion relation for different orders m, producing the band structure plot reported in figure 2.4. The reported computation refers to the case

fb

0 = 11.74 with a

d = 1.34 for the fundamental mode, based on the results of the three-dimensional simulations detailed in the following section. The corresponding effective refractive index was therefore varied in the range $3.23 < n_{eff} < 3.62$, which is roughly comparable to the value used to estimate the feedback and extraction wavevectors in the light-cone framework.

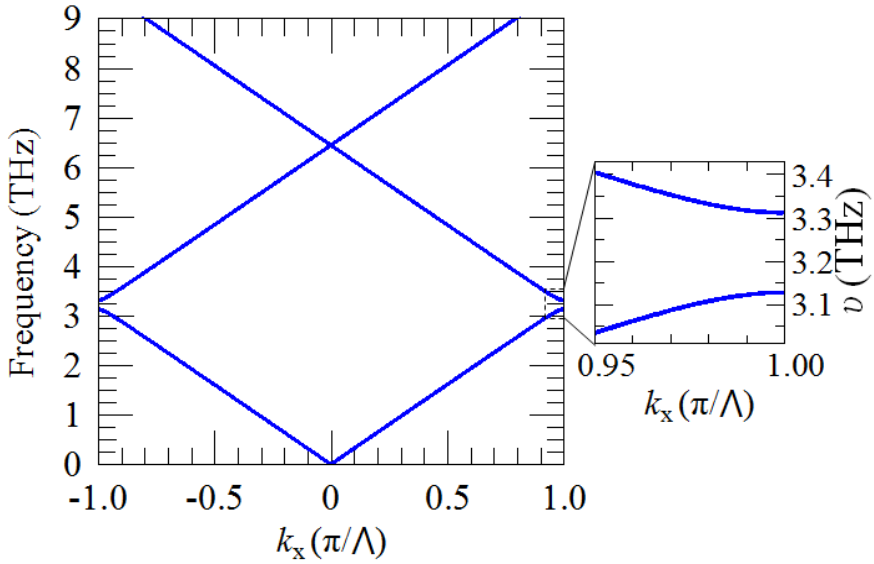

Figure 2.4: One-dimensional photonic band structure, computed on the periodic corrugation only, based on a sinusoidal spatial profile of the dielectric function, and for a ridge having

fb

The band-edge frequencies (for m = 0 and k =) are in very good agreement with the perturbation theory results discussed above. The photonic band structure contains the complete information about the electromagnetic modes which are permitted (and forbidden) inside the periodic corrugated wire laser, their frequency and wavevector. These modes are also characterized by the group velocity, which describes how fast their envelope propagates in the cavity:

$$v_g \propto \frac{d}{dk}\nu(k) \tag{35}$$

Since this slope goes to zero towards the band edge, the modes around the bandgap are the slower ones. It has been shown that the slow band-edge modes are those typically more likely to lase, so the devised corrugation allows selecting the desired emission frequency. Therefore, the emission properties of the laser can be tailored by tuning the periodicity width W, its modulation andwidth g of the active material.

2.2.3 Finite element method simulation

In order to simulate the lasing resonator structure robustly, including the effects of the extraction holes array and the lateral pads, a fully vectorial, three-dimensional (3D) model was implemented in a commercial (Comsol Multiphysics) finite element method (FEM) solver to study the resonating electromagnetic modes. A simulation was performed for the perfectly periodic resonator without the extraction hole array to calculate the quality factors, Q_{3D}, and the eigenmode frequencies, dictated by the feedback lateral corrugation, in the spectral range 2.6 3.8 THz.

The model was prepared as detailed in the following description and in figure 2.5. The bottom substrate and the top metallic surface were simulated as perfect electric conductors (PEC) to mimic the metal layers. The active material was described by the refractive index $n_{eff} = 3.50$, the Cr pads with $n_2 = 4.43 + 0.31i$, while the open boundaries outside the mesa were modeled with an external region of air ($n_{Air} = 1$), surrounded by appropriate scattering boundary conditions to mimic light propagation to free space. By comparing the electric field distributions associated with the highest Q_{3D}, we can distinguish a set of modes with distinctive envelopes that allows the bandgaps associated with the fundamental and higher-order lateral modes to be unambiguously determined. Since the electric fields of the higher-order lateral modes typically have a larger overlap with the corrugated edges than the fundamental mode, they experience a stronger variation in refractive index, which consequently results in a larger

e center frequency), while the first-order lateral mode has a center frequency of 3.51 THz and a bandgap of -order lateral

THz, which is well reproduced in the one-dimensional model for the photonic 0 d = 1.33.

2.3 Aperiodic sinusoidal wire laser

2.3.1 Aperiodic corrugated wire laser concept

Our photonic wire design was conceived to provide independent control of the feedback and extraction mechanisms through use of two independent photonic geometries. To ensure the necessary feedback for radiation propagating in the

resonator, a one-dimensional photonic grating is implemented by defining a lateral sinusoidal corrugation, which modulates the width of the 10- -thick

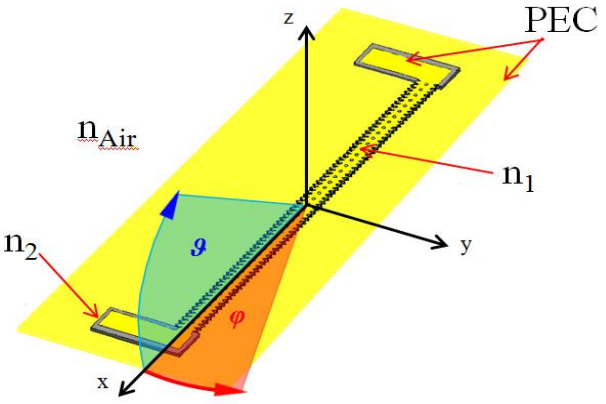

Figure 2.5: Schematics of the FEM model implemented to compute the resonating eigenmodes inside the photonic structure, with the indication of the different refractive indices and applied boundary conditions for the top and bottom metal of the laser waveguide. According to the

lying in the x y plane.

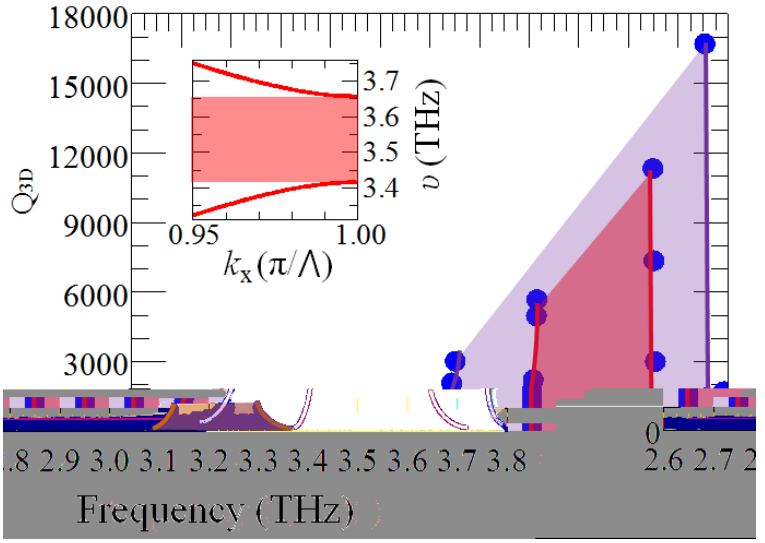

Figure 2.6: Three-dimensional quality factors, Q3D, computed at different eigenfrequencies for

fb

different photonic bandgaps associated with the fundamental mode (brown), the first-order lateral mode (magenta), and the second-order lateral mode (red), are shown. Inset: computed bandgap of the second-order lateral mode.

double-metal QCL cavity (figure 2.7) in the 30
resonator width is comparable to the typical THz wavelength in a GaAs/AlGaAs- radiation), making the

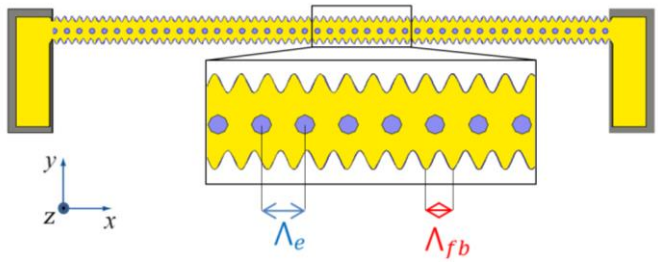

fb

-metal cavity comprises a central corrugated region, with two Cr pads at the ends of the resonator cavity being used to suppress unwanted electromagnetic modes. The inset shows the top metal contact (yellow) patterned with etched e, which define the extraction wavevector k_e e was varied in the range 19.4
emission frequency of 3.1 THz. The thin Cr absorbing layer is marked in gray.

system an almost perfect one-dimensional photonic structure. The spatial Fourier transform of the corr fb defines a feedback wavevector, which is twice the light wavevector in the active material. Setting the emission frequency to 3.1 THz, the feedback wavevector $k_{fb} = 2n_{eff}$ desired laser frequency) corresponds to

fb

index of the active region metallic waveguide $n_{eff} = 3.53$, as derived from the simulation of the transverse propagation of the fundamental mode in a two-dimensional slab [94]. Light extraction to the free space is controlled by a second grating: an array of circular holes lithographically defined on the top surface of the laser. The underlying semiconductor heterostructure is left exposed after removal of the upper metallic waveguide, and of the n+ top contact layer (by dry-etching) to prevent detrimental absorption of the outgoing

e, is designed to induce a longitudinal outcoupling of the radiation with an

A10). The one-dimensional light cone diagram in figure 2.8 provides a simple description of the scattering between the light, the feedback and the extraction wavevectors.

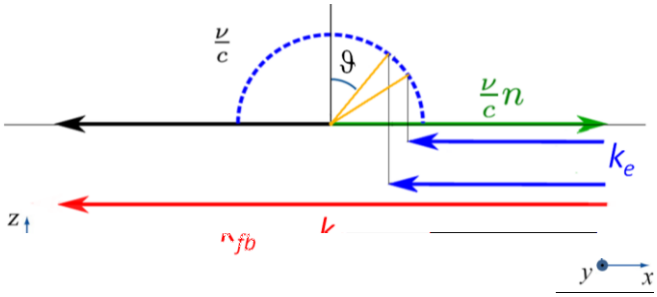

Figure 2.8: Light cone diagram. The feedback wavevector kfb (red line) and the extraction one ke (blue line) are indicated on the graph, together with the backward-propagating (black line) and forward-propagat

refractive index and c is the light speed in vacuum.

When a guided mode propagates inside the resonator with wavevector $n_{eff}k_0$ (black arrow in figure 2.8), it is scattered by the feedback vector k_{fb} (red arrow in figure 2.8) in the opposite direction (green arrow in figure 2.8). It can further scatter with the extraction wavevector k_e, which is defined via the choice of the hole array periodicity.

By carefully tuning k_e, the resulting diffracted mode can match the light wavevector in air, meaning that the vector sum of the three wavevectors must intercept the free-space light cone (blue dashed circular line, figure A13) with radius k_0

wavevector required for longitudinal emission is given by:

$$k_{\quad} = \frac{\nu}{\quad}(n_{\quad\quad} + \sin\theta) = \frac{\nu}{\quad}(n_{\quad\quad} + 1) \tag{36}$$

$_e$. By

$_e$

-dependent effective refractive index can be engineered by design in a QCL, we can obtain a perfect matching condition by tuning the extraction wavevector, by spanning a 10% range around the light cone edge. To achieve this, a series of wire lasers incorporating surface hole array of different periodicities were lithographically defined to achieve a

$_e$

$_e$ was

between 19.4
expected emission frequency of 3.1 THz. This allowed the investigation of the optimal scattering condition, for which light extraction is enhanced and emitted in the desired direction, with low divergence and large quantum efficiency.

2.3.2 Three-dimensional numerical simulation

The resonator geometry is characterized by two independent periodicities, due to the presence of the lateral sinusoidal corrugation and the extraction hole array on the top metal surface. The classical discrete spatial invariance of a photonic crystal is broken and a properly defined band structure no longer exists, requiring an alternative computation approach to handle the increased complexity of the system. A dedicated three-dimensional FEM model was therefore implemented to solve Maxwell's equations including the effects of extraction hole array on the top metallization (as in figure 2.5). The presence of the extraction holes results in a decrease of the global quality factor Q_{3D}, as a consequence of the increased radiative losses, for the modes with larger overlap with the patterned surface.

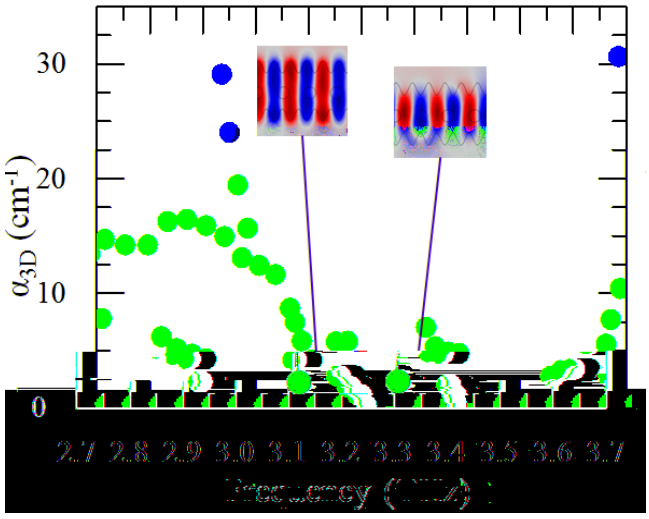

$_{3D}$ plotted as a function of the resonant frequencies for a 40- -wide

e E_z
(x,y) for the fundamental band-edge modes above and below the bandgap. Red (blue) indicates negative (positive) values of E_z.

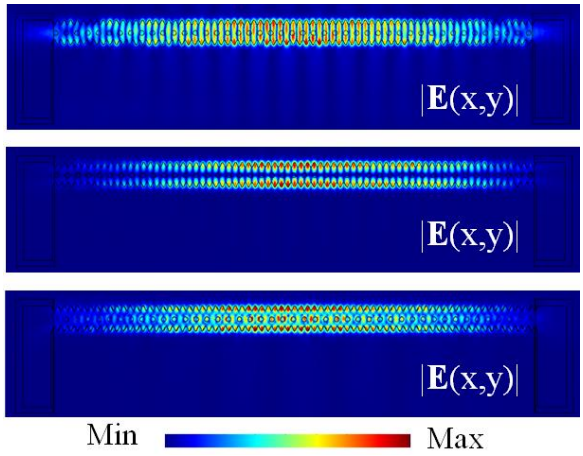

Figure 2.10: Spatial distributions of the normalized electric field |E(x,y)| of the lower-edge states at half height (z =

-

plot), and the second-

A careful analysis of $_{3D}$ in the whole aperiodic structure (figure

fundamental and higher-order modes are perturbed differently. The states at the fundamental upper and lower band edges show comparable losses of about 2.5 cm and their electric field distribution are only slightly altered by the extraction holes (insets to figure 2.9). It is worth mentioning that for the case of the higher-order bandgaps, the upper-edge mode losses are instead significantly increased by the hole patterning, being five times larger than the losses of the corresponding lower- $_{3D} < 1$ cm .

Figure A15 shows the electric field for the fundamental and higher-order modes located below the respective bandgaps, in the presence of an extraction hole -order lateral lower-edge mode is less affected by the presence of the holes, as can be easily seen by the distribution of the electric field which vanishes at the center of the mesa (central subfigure 2.10). The fundamental and second-order lateral modes have high-electric field intensities at the center of the bare feedback resonator, so the addition of the hole array induces distortions in the field distributions and enhances their outcoupling to the free space (top and bottom subfigure 2.10). The 3D simulations furthermore indicate that the eigenfrequencies near the band-edge are only slightly ermined by the feedback geometry.

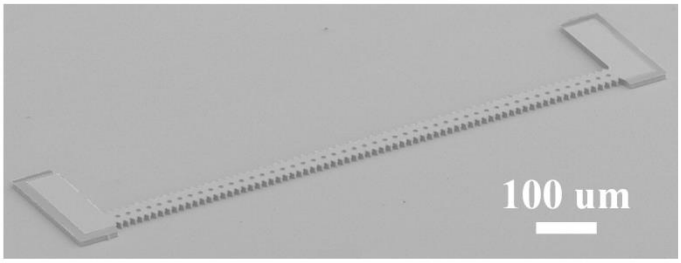

Figure 2.11: Scanning electron microscope (SEM) image of a fabricated aperiodic corrugated wire laser.

2.4 Fabrication methods

For the fabrication of the aperiodic corrugated wire lasers, two different QCL heterostructure were used, both grown by molecular beam epitaxy (MBE) on an undoped GaAs substrate to form a sequence of layers of GaAs and $Al_{0.15}Ga_{0.85}As$. A three-well resonant-phonon architecture [95] is implemented in the material used for the lasers operating in pulsed regime, with a layer sequence: **4.3**/8.9/**2.46**/8.15/**4.1**/<u>16</u> (in nm), where the $Al_{0.15}Ga_{0.85}As$ barrier layers are in bold, GaAs in Roman and the underlined number indicates the presence of a 5 nm-thick Si-doped region at the center of the last well, with an electron density of 6 10^{16} cm^{-3}. The second active material's design exploits a bound-to-continuum QCL with a single-quantum-well phonon extraction stage [96] based on a layer sequence of **5.5**/11.0/**1.8**/11.5/**3.8**/9.4/**4.2**/<u>18.4</u> (in nm), with the last well having a Si doping concentration of 2 10^{16} cm^{-3}. After growth, all the fabrication was carried on in the cleanroom facilities of the NEST Laboratory, using the protocols and techniques detailed in Appendix B. A thermo-compressive wafer bonding was performed, bonding the QCL on an n+-GaAs carrier wafer with Au-Au interface. After a selective etching of the host GaAs substrate and the $Al_{0.5}Ga_{0.5}As$ etch-stop layer, the lateral pads were first defined with optical lithography and thermal evaporation of thin Cr (7 nm) rectangles, implementing strong absorbing boundary conditions. A second optical lithography was performed to define the sinusoidal top metallization with the extraction hole array, with a successive Cr/Au (5 nm/150 nm) thermal evaporation, partly overlapping the Cr pads. The whole deposited metal acted as a mask during the inductively coupled plasma reactive ion etching (ICP-RIE) process, which selectively removed the n+ top contact layer only inside the extraction holes but not elsewhere, where the absorbing boundary provided by Cr and the top contact layer is necessary. The final processing step used the

ICP-RIE etching to define the wire laser ridge, ensuring that the lateral corrugation was properly implemented with sharp and vertical semiconductor sidewalls. Individual devices were soldered onto a copper submount with a conductive Ag/In paste, and then wire-bonded on both lateral pads to provide uniform current injection in the device with area of 0.074 mm^2 (fig. 2.11).

2.5 Experimental results

2.5.1 Electrical and optical characterization in pulsed operation

Figure 2.12 shows the measured current density voltage (J V) and power current density (L J) characteristics of a set of five wire lasers, driven in pulsed operation with a repetition rate of 100 kHz and a pulse width of 200 ns, at a temperature of 20 K in a nitrogen-purged environment. Most lasers produce a maximum peak optical power in the range 5 15 mW. However, when the

output power exceeds 40 mW, due to the combined effect of the enhanced coupling losses and the significant beam reshaping, which have a positive impact on the collection efficiency. The highest optical power is also reflected in the lowest threshold current density J_{th} = 970 A cm , with J_{th} ranging between 1.0 and 1.2 kA cm
values).

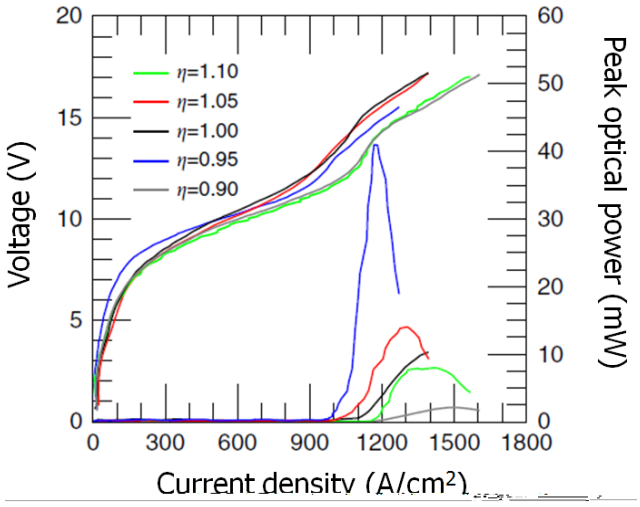

Figure 2.12: Voltage current density (V J) and power current density (L J) characteristics -purged atmosphere. All lasers are driven in pulsed mode with a pulse width of 200 ns and pulse repetition rate of 100 kHz. Optical power scales were corrected to account for the detector collection efficiency and the absorption of the polyethylene cryostat window. The device area is 0.074mm^2.

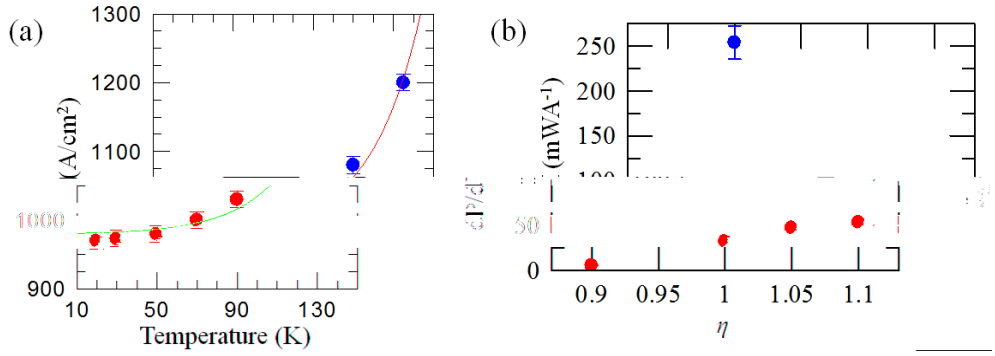

Figure 2.13: a) Threshold - sink temperature. The red line is the fit based on the empirical formula Jth (T) = $J_1 + J_2 \exp(T/T_2)$. The error bars account for errors on the extrapolated threshold current densities. b) conditions shown in a, with error bars derived from the linear fitting procedure of the slope.

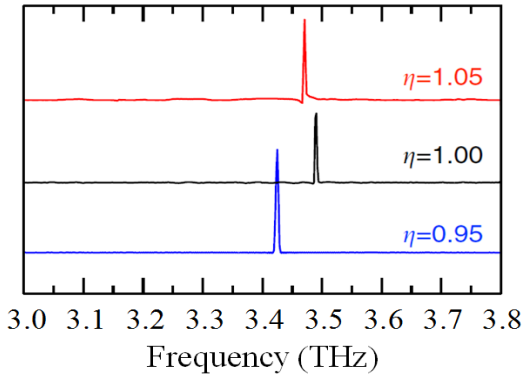

Figure 2.14: Fourier transform infrared emission spectra for selected aperiodic corrugated devices in pulsed operation, measured in rapid scan mode with a spectral resolution 0.125 cm^{-1}.

It is worth mentioning that the measured J_{th} in our wire lasers is comparable or only slightly larger than that measured in standard Fabry Perot (FP) cavities (~1 kA cm for the same epitaxial material) [95].

The thermal behavior of the fabricated devices was further investigated by measuring the variation of threshold current with the increase of the heat sink temperature. As reported in figure 2.13.a, the best-perfoming device operated up to a heat-sink temperature of 135 K, which corresponds to an estimated

lattice temperature T_L

, significantly larger than that achieved (5 - 60 mWA) when the extraction parameters are not properly matched, and much larger than the best third-order DFB THz QCL resonators reported to date (130 - 140 mWA) [B4,B11]. Another important figure of merit for THz QCLs is the wall-plug efficiency (WP), which quantifies the optical to electrical power

larger than corresponding FP double-metal cavities fabricated with the same double-metal sequence and without removing the highly doped top contact.
Furthermore, the spectral properties of the devices were investigated with a Fourier Transform Infrared spectrometer, demonstrating stable single-mode emission. Figure 2.14 shows the Fourier transform infrared (FTIR) emission spectra measured at a heat-sink temperature of 10 K, while driving the QCLs in pulsed mode with a 2% duty cycle. In all cases, a single spectral line is observed across the entire QCL gain bandwidth, with its frequency shifting slightly between 3.43 and 3.49 THz when the extraction parameter is tuned over the selected range. This is in agreement with the simulation results presented earlier, which identifies the lower band-edge mode of the second-order lateral excitation at the frequency of

2.5.2 Far-field intensity patterns in pulsed operation

The influence of the extraction hole array periodicity on the far-field beam pattern was investigated, by sampling the intensity distribution patterns in the far field by scanning a pyroelectric detector in the plane orthogonal to the y z surface at a distance of ~8 cm. As expected, the far-field intensity plots show different divergences as a function of the extraction wavevector as reported in figure 2.15. For the case of -lobed and localized

expected to be reduced by the increase of the cavity length [87,89], which can also have a beneficial effect on the optical power output [89] and the slope efficiency.

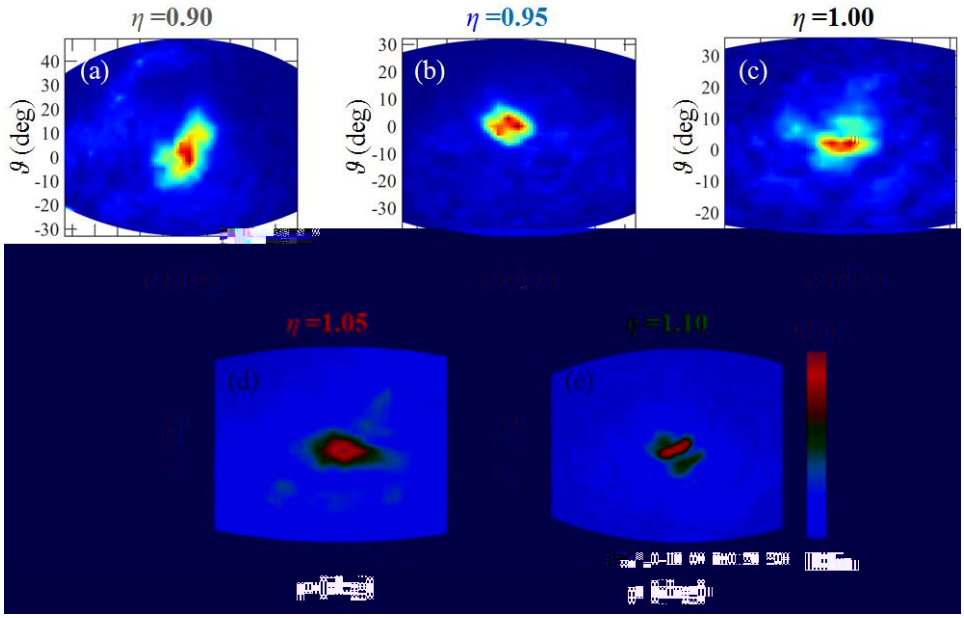

Figure 2.15: Far-field emission patterns measured at 20 K in pulsed mode with 2% duty cycle, 1.10. All the measurements were performed scanning a pyroelectric detector at 8 cm from the device lateral surface. The origin of the plots coincides with the origin of the x-y-z reference system of Fig. A10. The scanned area is 12×12 cm.

2.5.3 Continuous-wave operation

Our architecture also offers the potential for high power, low-divergence continuous-wave (CW) emission. In order to demonstrate this, a second set of resonators was fabricated by using a different active region material[96], whose bandstructure design is optimized to have a lower operating current density and alignment bias, so that self-heating by Joule dissipation is reduced with respect to the previously used gain medium [95]. The resonator width was also varied in the 40 ct on the resonant frequency and output power. The V J and L

temperatures. For comparison the inset of Fig. 2.16 shows the CW performances of an edge-emitting FP THz QCLs, having comparable dimensions and fabricated from the same semiconductor heterostructure. A maximum CW optical power of 6 mW and a slope efficiency of 100 mW/A were measured in our sinusoidal wire laser at a heat-sink temperature of 10 K, in a nitrogen-purged atmosphere, against the 2.5 mW of power achieved in the

corresponding FP laser. The sinusoidal wire laser reaches maximum WP in CW of about 0.23%, about 40% larger than that achieved in perfectly phase-matched third-order DFBs.[87]

The beam divergence of this batch of fabricated devices is similar to the previous case, as reported in fig. 2.17a where the far-field intensity pattern is -field profile (Fig. 2.17b d) show that the diameter of the extraction hole array has a role in tailoring properly the optical beam shape: indeed by reducing the hole diameter by 50% (Fig. 2.17b) the beam shape divergence is slightly reduced in

2.17d) starts to significantly increase the divergence and deteriorate the optical beam shape. Figure 2.18 shows the FTIR emission spectra for two devices with

operation. The 40- -wide wire laser emits single mode at 3.11 THz, while the -shifted peak at 3.08 THz and a much less intense line at 3.22 THz.

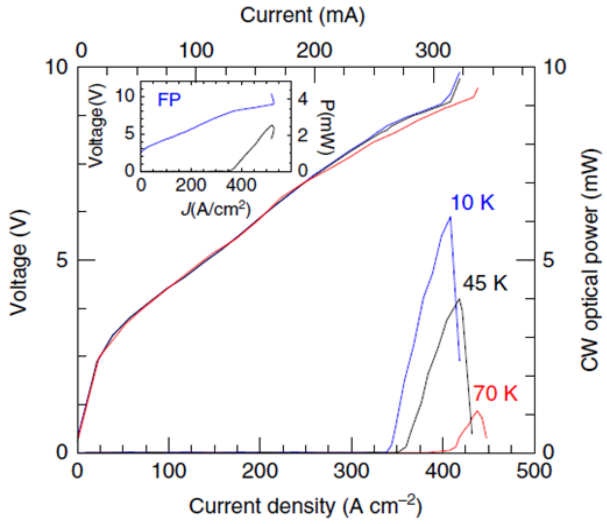

Figure 2.16: Voltage current density (V J) and power current density (L J) characteristics measured in continuous-wave mode and at different heat-sink temperatures, for a representative

scales were corrected with the detector collection efficiency and the absorption of the polyethylene cryostat window. Inset: V J and L J characteristics measured in CW mode at 10 K, for a Fabry Perot (FP) wire laser fabricated from the same semiconductor heterostructure

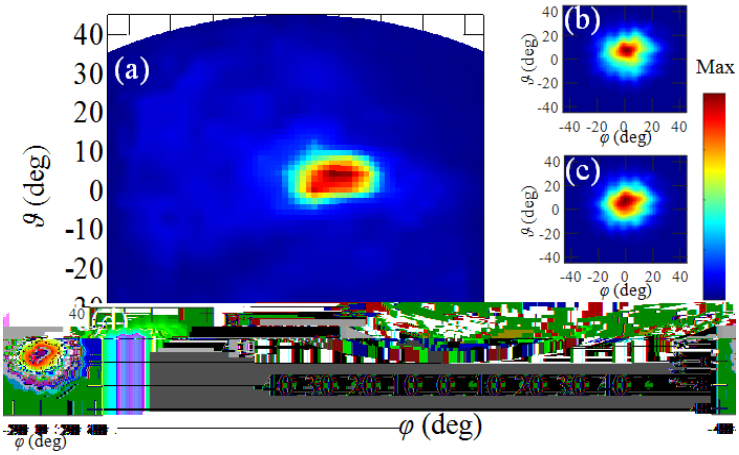

Figure 2.17: a) Far-field intensity pattern of the device in fig. A21, measured at a distance of 8 cm from the laser surface. b) d) Simulation of the far-field emission intensity profile of the emitting optical mode, derived by applying the Stratton-Chu method to the near-field emission

The spectral peak at 3.1 THz correlates well with the frequency of the lower-edge mode of the fundamental photonic bandgap, as computed in our 3D FEM

resonator size. In the case of the 45- -wide resonator, the low intensity high-frequency peak is very close to the computed frequency of 3.21 THz for the lower-edge mode of the second-order lateral bandgap. The variation of the average ridge width is also reflected in the maximum power output, which is ~10% lower for the 40- -wide device with respect to the 45- structure. Since the mode has little overlap with the lateral pads and is mostly confined into the 1 mm-long sinusoidal mesa, the extracted optical power consequently scales with the width of the corrugated region. The ridge width

40-
direction, radiation has a -
-

2.6 Discussion

The presented novel photonic wire THz resonator architecture is based on a sinusoidal lateral ridge corrugation as the feedback grating, and a surface array of holes as the extraction grating. The extraction array periodicity is tuned to optimize the light extraction, so that the optical power and laser efficiency are enhanced, reaching a maximum peak output of 42 mW in pulsed regime, with a

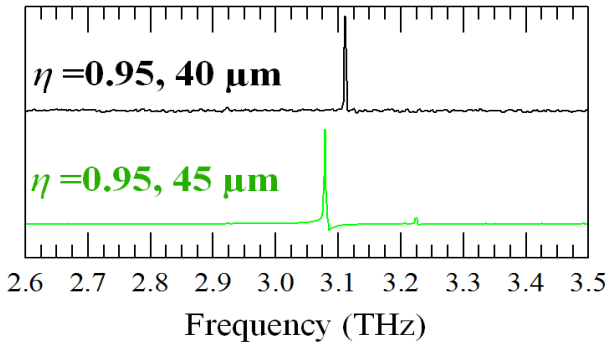

Figure 2.18: FTIR emission spectra collected in rapid scan mode at a 0.125 cm resolution and with an internal deuterated triglycine sulfate (DTGS) pyroelectric detector for a set of devices

slope efficiency SE 250mW/A. CW operation is demonstrated with a maximum power output of 6 mW, corresponding to a maximum WP of 0.23%. The devices show beam divergence with optimal collimation of 10°. The combined effect of the improved coupling losses of the wire laser structure and of the significant beam reshaping which has a positive impact on the collection efficiency lead to the reported high-power performance. Further power and efficiency improvements could be enabled by optimizing the quantum design, with no deterioration in the threshold current density and with only a minor influence on the maximum operation temperature, constrained by the lossy absorbing boundary.

Other strategies to improve the present performances also include: the increase of the wire laser length, which could help increasing the output power and reducing the beam divergence [87,89]; the reduction of the area of the lossy absorbing boundary pads to decrease the overall dissipation and the local lattice temperature; the reduction of the thickness of the top highly doped contact layer underlying the unpatterned top metal surface to lower the waveguide losses, and increase the power extraction. Moreover, the use of broader gain region architectures would allow devising an array of on-chip wire lasers for tuning the laser emission[98] which could also exploit an on-chip mechanical architecture. The devised aperiodic architecture does not require demanding lithographical constraints very differently from other photonic engineering approaches reported to date and is also easily scalable. Therefore, our devices could become an important underpinning platform for future applications in high-resolution spectroscopy, metrology, and quantum manipulation of cold atoms.

CHAPTER 3:
ONE-DIMENSIONAL OCTONACCI QUASI-CRYSTAL LASERS

3.1 Introduction

This chapter focuses on the development of a one-dimensional resonator architecture based on a quasi-crystal grating integrated into double-metal 1D DFB THz QCLs. The photonic pattern exploits a series of rectangular slits whose position is determined according to the Octonacci sequence, producing an aperiodic spatial modulation of the effective refractive index for the THz radiation in the cavity. This induces a distributed feedback (DFB) on light propagation, which can be tuned to control the associated scattering and extraction processes.

As discussed in Chapters 1 and 2, the conventional DFB schemes rely on a periodic distribution of scattering elements (slits, holes or groves) across the laser resonator, which provides the wavevectors interacting with the photon [61,99] and produce a well-defined photonic band structure. This results in the formation of spectral bandgaps associated to forbidden photon propagation, while laser operation is typically achieved at frequencies corresponding to the photonic band edges [63]. Periodic photonic structures have been successfully exploited in combination with miniaturized QCL heterostructures for operation at mid-IR [100] or terahertz (THz) frequencies [101], also using unconventional resonator architectures to tailor the laser optical power,[30] emission frequency,[23,24,30] and beam direction [28] and divergence [25,89], with important applications in spectroscopy, imaging, sensing and metrology. [102-105] Examples of 1D and 2D regular photonic structures include microring mid-IR or microdisk THz lasers [106,107] and photonic crystal lasers. [26,27,64] Distributed feedback (DFB) lasers [22-25, 30, 87, 89, 101] have been devised exploiting the different orders of their harmonics, or architectures [40,90] to finely manipulate the light scattering and the extraction mechanism. As an intrinsic feature, periodic resonators support electromagnetic eigenmodes having well-defined symmetric and anti-symmetric spatial distributions. These regular spatial field profiles lead to mode gain competition, intra-cavity confinement and far-field interference effects, which usually result in a poor extraction of the optical power from the laser. Therefore, the development of photonic structures featuring defects breaking the spatial periodicity by design

allows removing the critical mode symmetry and circumventing the associated optical power limitations.
This issue can be addressed by devising resonator architectures featuring localized defects to perturb, on purpose, the resonator periodicity, such as dual periodicity gratings [28], hybrid DFB patterns [108], graded photonic heterostructures [84,109]. In this respect, the novel one-dimensional photonic architecture reported in chapter 2, based on laterally corrugated wire lasers with surface extraction grating [40], demonstrated high power output in both pulsed and CW regimes, while ensuring tight control over the single-mode emission spectrum and the beam collimation. Even fully non-deterministic disordered patterns have been investigated for THz QCLs, providing an inherently multimode emission for both one-dimensional [110] and two-dimensional random THz lasers [32-34,41], as further detailed in Chapter 4 with the discussion of the random QCLs devised for this thesis [41].

In-between the perfectly periodic architectures and completely disordered ones, photonic quasi-crystal resonators [67] lack a discrete translational invariance, but are generated by a deterministic algorithm and feature long-range order [65,66]. They cannot be described within a classical band structure picture due to the absence of a spatial periodicity. Similarly to periodic photonic crystals, quasi-crystals can support extended band-like states at the edges of their spectral pseudo-gaps, but they can also host localized modes, in analogy with the Anderson modes in completely random structures [71], which is simply not possible in periodic structures. The singular continuous spectrum of a quasi-crystal [67] can be engineered to control independently the frequency spacing and the position of the mode, allowing to separate Bragg resonances for feedback and out-coupling, leading to a controlled collimated emission at a desired angle, without affecting the lasing frequency. In turn, this determines a complex light interference pattern, typically selecting a number of resonating (radiative) eigenmodes having large quality factors which are produced by the interaction of photons with multiple Bragg peaks. Quasi-crystal patterns implemented in THz QCLs have been used to control light feedback and outcoupling, to tailor the emission spectra and to shape the laser beams, exploiting either one-dimensional geometries as Fibonacci gratings [29], or two-dimensional structures such as 5-fold Penrose patterns [30] or 7-fold schemes with different rotational symmetries and degrees of disorder [31].

One-dimensional geometries benefit from the possibility to achieve a good thermal management, due to their the small scale and compact size, as needed for practical applications, as well as from the typical advantages of quasi-periodic structures, such as a directional output independent of the emission frequency and multicolor operation. Up to now, the available reports on one-dimensional quasi-crystal THz QCLs [29] indicate that the laser emission is limited to output peak power below 6 mW with low wall-plug efficiencies (~0.01%), which are detrimental for an extensive use of such technology for applications in chemical and biomolecular sensing or spectroscopy, where high-power monolithic terahertz QCLs with tailored spectra are highly desirable.

In this chapter, a one-dimensional quasi-crystal THz QCL architecture is introduced, detailing the design of the top metal slit grating based on the quasi-periodic Octonacci sequence,[41] which demonstrated a significant increase in the current state-of-the-art performance of surface-emitting THz lasers. By tuning the slit size and the laser ridge width, the interaction between the grating scattering wavevectors and the photon propagation was optimized, achieving a surface THz emission with ≈ 240 mW peak optical power with the highest slope efficiency (≈ 500 mW/A) reported to date in an electrically pumped THz laser. Dual lobe beam profiles, which are symmetrically placed at 25° from the surface normal, irrespective of the geometric parameters, have been measured. By tuning the lithographic patterns, switching between single-mode and multimode emission was achieved over a maximum spectral bandwidth of ≈ 500 GHz, defining the photonic pseudo-bandgaps.

3.2 Quasi-crystal architecture

3.2.1 Octonacci grating design

The devised one-dimensional photonic architecture is based on an array of open rectangular slits, lithographically defined in the top metal surface of the laser. The slit distribution produces a local spatial modulation of the refractive index, providing the photon scattering mechanism for light feedback and extraction similarly to conventional DFB structures.

The pattern of the slits along the laser top metal is generated through a deterministic algorithm implemented in a custom Matlab code based on the Octonacci quasi-crystal sequence [111]. The mathematical definition of this quasi-periodic sequence S_n follows a generation rule which starts with two initial elements S_1 = B and S_2 = A. The nth-order sequence is given by

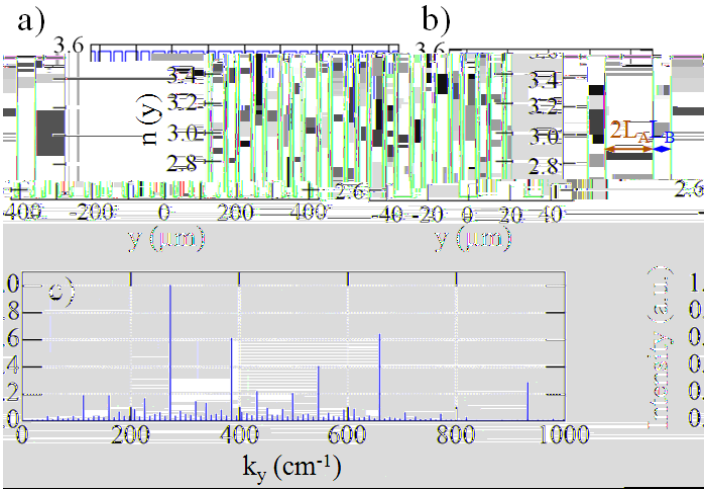

Figure 3.1: a) Spatial modulation of the effective refractive index associated to a one-dimensional pattern of open slits defined according to the 8th-order Octonacci sequence, with the geometric parameters L_A = 11.6 μm and L_B = 8.7 μm and a resulting quasi-$2L_A+L_B$ = 31.9 μm. b) Zoomed section of the refractive index spatial modulation induced by the Octonacci grating, which highlights the length L_A associated to the metal-covered regions and the length L_B associated to the open slit. c) Fourier space representation of the grating wavevectors, with the main Bragg peaks contributing to the photon scattering inside the photonic quasi-crystal pattern.

$$S_n = S_{n-1}S_{n-1}S_{n-2} \tag{37}$$

for n > 2, i.e. the lowest order sequences are S_3 = AAB, S_4 = AABAABA and S_5 = AABAABAAABAABAAAB. The Octonacci series can be defined equivalently by the application of the so-

. The n_{th} order Octonacci sequence is made up of a number n_A of A-elements and n_B of B-elements, giving a total number of elements equal to the Pell number $P_n = n_A + n_B$, defined as $P_n = 2P_{n-1} + P_{n-2}$ for n > 2, with $P_1 = 0$ and $P_2 = 2$. The Octonacci pattern on the top metal surface of a double metal was implemented following this approach: for each B-element, an air slit with size L_B is placed along the top metal surface, while a metal-covered segment with length L_A is added in correspondence of each A-element composing the Octonacci sequence (see Fig. 3.1a). The generated Octonacci quasi-crystal grating is characterized by a quasi- $_A+L_B$, indicated in figure 3.1b, which is associated to a scattering wavevector k_0

by transfer-matrix studies of the Octonacci one-dimensional grating [112], an Octonacci grating supports a number of photonic pseudo-bandgaps appear

$_0 = ck_0/n_{eff}$, where c is the light speed in vacuum and n_{eff}

is the effective material refractive index. The pseudo-bandgaps are concentrated $_0$ - $_0$, and their edge frequencies are usually associated to the presence of electromagnetic modes with high quality factors and large radiative losses, meaning that they are typically responsible for lasing. Considering a two-dimensional effective index model [94] for the target photon frequency of about 3.3 THz, the air slit is described with an effective refractive index $n_B = 2.55$, while in the metal-covered area has $n_A = 3.55$. The characteristic Octonacci lengths are initially to the values $L_B = 8.7$ µm and $L_A = 11.6$ µm, giving a 8th-order Octonacci grating which induces the spatial modulation of the refractive index shown in figure 3.1.a. The corresponding spatial Fourier transform indicates the existence of many Bragg peaks (fig. 1.c), involved in the surface extraction. Indeed these peaks, in the reciprocal space of the quasi-crystal, are exploited to achieve the scattering with the photons propagating in the resonator, providing light feedback and extraction. For a quasi-periodicity transfer-matrix approach predicts multiple photonic bandgaps for TM-polarized light in the range between 2.0 THz and

3.2.2. Three-dimensional numerical simulations

A more in-depth study of the devised quasi-periodic resonators was performed using a finite element method (FEM) commercial software (COMSOL MultiPhysics) to solve a fully three-dimensional electromagnetic model of the Octonacci double metal waveguide. The GaAs/AlGaAs-based active region heterostructure [96] was described with a refractive index $n_1 = 3.6$. The ridge external border is covered by a 7nm-thick Cr layer to suppress undesired modes extending to the resonator edges, so the chromium layer and the heterostructure underneath are modeled with an effective medium having a complex index $n_2 = 4.43 + i0.31$, accounting for the optical losses induced by Cr. The top and bottom metal claddings of the laser are described setting the perfect electric conductor (PEC) conditions, while a finite volume of air with $n_{Air} = 1$ surrounds the laser, as shown in figure 3.2. In order to mimic light propagation in the free space, scattering boundary conditions (SBCs) are implemented at the external boundary domains of the air volume. The resonator geometry is designed with a fixed ridge length of 2.9 mm, including the top metal cladding with the 8th-order Octonacci grating and the Cr-covered pads at the edges of the ridge. A set of resonators, with different ridge widths W = 40 µm, 60 µm, 80 µm, 160 µm,

Figure 3.2: Schematics of the three-dimensional FEM model implemented to compute the resonating modes via the Maxwell's equations. The laser active material is described with a refractive index $n_1 = 3.6$, while the external border of the ridge covered by an optically absorbing 5 nm-thick Cr layer has an effective complex value $n_2 = 4.43+i0.31$. The top and bottom metal layers of the laser are treated as perfect electric conductor (PEC) conditions and the device is surrounded by air with $n_{Air} = 1$. The far- -z plane) and (in the y-z plane).

was conceived to explore the effects of the change in the lateral device size on the resonating eigenmodes and on their quality factors.

Furthermore, the slit width L was changed from the initial value of L_B= 8.7 µm to L = 1.9 µm and 3.5 µm, in order to limit the vertical optical losses, while ensuring the necessary scattering for the electromagnetic radiation. By keeping

igeee-7(a)4(140)-29(fr)5()-7(ture[(to)-413)Q36(L)] TJETQq0.000007435 0 498.96 709.08 r

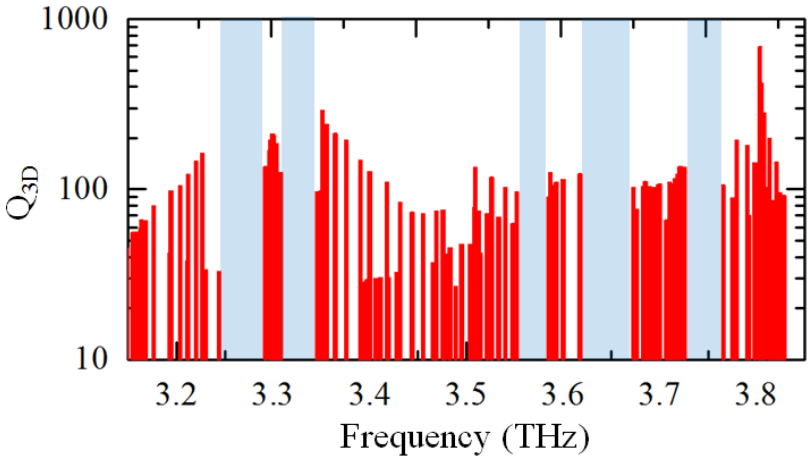

Figure 3.3: Plot of the three-dimensional quality factor as a function of the resonating frequency for a device with ridge width W = 160 µm, slit width L = 1.9 µm, and quasi-
31.9 µm. The light blue areas highlight the photonic pseudo-bandgap associated to the Octonacci quasi-crystal structure.

Octonacci photonic gratings with different slit widths L were also simulated, in order to assess the impact of the aperture size on the radiative efficiency of the resonator eigenmodes, as shown in the plot of figure 3.4. For a ridge width W = 160 µm with slit width L = 1.9 µm (red dots), the simulation indicates that the

rad

rad photonic pseudo-bandgaps. Instead for L =

3.5 µm (blue dots), the frequencies of the most radiative modes are blue-shifted by a few tens of GHz with respect to the case with L = 3.5 µm. The radiative efficiency associated with the lowest band-edge modes around 3.3 THz is 10% higher in the case of L = 3.5 µm, as a consequence of the larger extraction area provided by the quasi-crystal apertures.

3.3 Fabrication methods

The fabrication of the Octonacci lasers is based on the use of a GaAs/$Al_{0.15}Ga_{0.85}As$ QCL heterostructure, grown by molecular beam epitaxy on an undoped GaAs substrate. As reported in [96], the active region is based on a three-quantum-well architecture, with a single extractor well, with the following layer sequence: **5.5**/11.0/**1.8**/11.5/**3.8**/9.4/**4.2**/<u>18.4</u> (in nm), where the

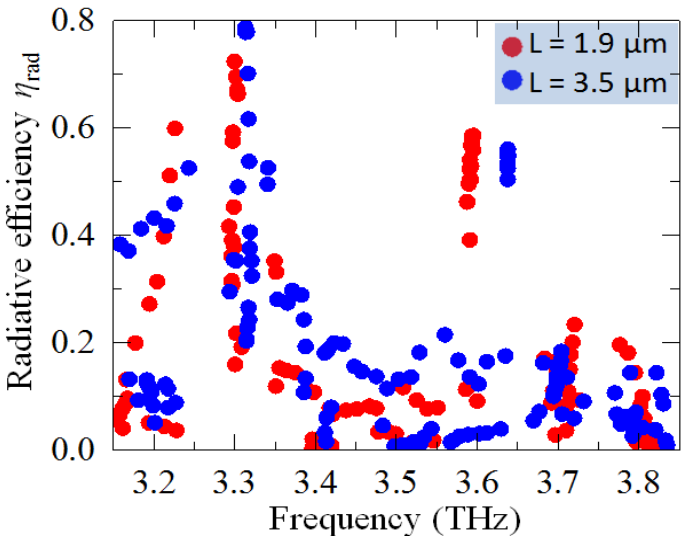

Figure 3.4: Radiative efficiency calculated from three-dimensional simulation of the resonating modes in an Octonacci laser featuring a slit aperture L = 1.9 µm (red) and L = 3.5 µm (blue) and fixed width W = 160 µm. The computed photonic pseudo-bandgaps for L = 1.9 µm are blue-shifted by few tens of GHz with respect to the slit aperture L = 3.5 µm.

$Al_{0.15}Ga_{0.85}As$ layers are shown in bold face, GaAs in roman font, and the underlined number indicates a Si-doped layer with a density of 2 x10^{16} cm^{-3}. A 700 nm-thick highly doped (2 x10^{16} cm^{-3}) GaAs contact layer terminates the active region growth, with a $Al_{0.5}Ga_{0.5}As$ etch-stop layer on the top. After growth, Au-Au thermo-compressive wafer bonding of the QCL wafer onto an n^+-GaAs carrier wafer was performed. The host GaAs substrate and the $Al_{0.5}Ga_{0.5}As$ etch-stop layer were selectively removed via wet etching, so that the sample surface was patterned with UV lithography with air slits, whose center positions are in correspondence with the Octonacci sequence scheme realized with a MATLAB code. These top patterns on the active region were coated with a top metal layer of Cr/Au with thickness of 5 nm/150 nm. The resonators were fabricated with different slit widths L and the laser ridge widths W. The 700-nm-thick n+ top contact layer was totally removed from below the etched slits, using an inductively coupled reactive-ion etching (ICP-RIE) process, reducing the cavity losses and enhancing light extraction. An external Cr border was imprinted on the active region using optical lithography around the gold top metal region, depositing 7 nm-thick layer of Cr to implement strongly absorbing boundary conditions. Below the Cr border, the n^+ top contact layer was not etched away so that the suppression of modes extending towards

the edge of the resonator was further increased. A final ICP-RIE process was required to etch down the ridge with vertical sidewalls, defining the final geometry of the device, reported in figure 3.5a and 3.5b. Finally, the Octonacci resonators were individually cleaved and indium-soldered onto a copper submount and wire bonded at the two edges of the long side of the ridge. In this way, the possible perturbation of the far-field emission profile due to the presence of the gold wires is minimized.

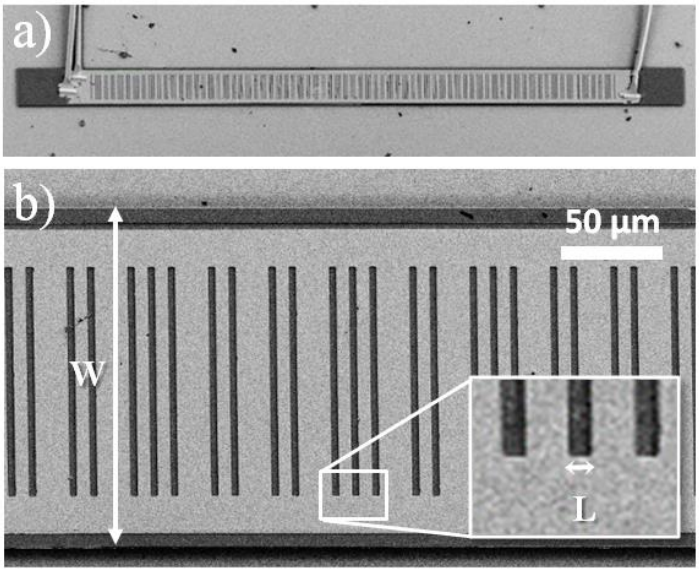

Figure 3.5: a) Scanning electron microscope (SEM) image of a fabricated Octonacci resonator having ridge width W = 160 µm and length of 2.9 mm, and featuring the Octonacci grating on laser top surface with slit width L = 3.5 µm. b) Zoomed view of a section of the device, highlighting the ridge width W and the slit width L (see inset).

3.4 Experimental results

3.4.1 Electrical and optical characterization of multimode devices

Exploiting the performed numerical simulations, a set of devices with different ridge width W and slit size L were fabricated to study the effect of these geometrical parameters on the laser performances.

Figure 3.6: Plot of the current density - voltage (J-V) and light - current density (L-J) characteristics of Octonacci lasers with different ridge widths W = 60 μm and 160 μm, but same ridge length (2.9 mm) and slit width L = 1.9 μm. The lasers were driven in pulsed mode at a 1% duty cycle (pulse width of 200 ns, pulse repetition rate of 50 kHz) at a heat sink temperature of 20 K. The optical power scale accounts for the radiation collection efficiency of the pyroelectric detector and the 75% transmission of the cryostat polyethylene window.

Figure 3.6 shows the experimental current density-voltage (J-V) and current density-peak optical power (J-L) characteristics measured for resonators having the same surface patterning (slit width L = 1.9 μm), but different ridge widths W = 60 μm and 160 μm. All LJV measurements were performed operating in pulsed regime with a duty cycle of 1%, i.e. repetition rate of 50 kHz and pulse width of 200 ns, and at a heat sink temperature of 20 K. A maximum value of peak optical power of ≈ 240 mW is achieved for the device having W = 160 μm, corresponding to a slope efficiency SE ≈ 500 mW/A and a wall-plug efficiency WP ≈ 0.6%. By reducing the ridge width at W= 60 μm, the peak optical power is consequently reduced down to ≈ 57 mW, with SE ≈ 420 mW/A and WP ≈ 0.5%, due to the smaller available volume for laser amplification and to the reduced extraction efficiency related to the smaller slit area. The threshold current densities J_{th} of the devices is almost constant, being between 412 A/cm^2 and 420 A/cm^2 for the different ridge widths W = 160 μm and W = 60 μm, respectively. Figure 3.7 shows the Fourier Transform Infrared (FTIR)

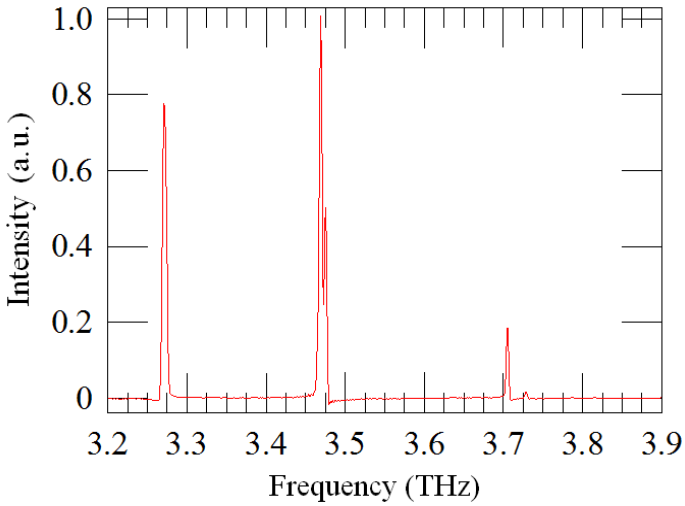

Figure 3.7: FTIR emission spectrum of the device with W = 60 µm and slit width L = 1.9 µm, operated at 12 K with a duty cycle of 4%, acquired with a spectral resolution of 0.125 cm^{-1} and averaging over 32 scans.

The spectrum features 5 optical modes, with the main ones emitted at 3.280 THz, 3.480 and 3.485 THz, with some less intense lines around 3.72 THz, covering a total emission bandwidth of 450 GHz. An even richer multimode emission of this Octonacci architecture with L = 1.9 µm is demonstrated by the FTIR spectrum measured for the larger laser (W = 160 µm), reported in figure 3.8. The laser emission features a dominant optical mode at 3.39 THz with 13 spectral lines comprised between 3.30 THz and 3.78 THz, over a 480 GHz-wide spectral interval. This is in good agreement with the simulations, indicating that larger ridge widths W support a high-quality-factor modes over a large bandwidth. The comparison between experimental data and simulations for W = 160 µm and L = 1.9 µm show that the more intense peak is very close to the upper edge of a photonic pseudo-bandgap centered around 3.35 THz, while the minor peaks between 3.7 THz and 3.8 THz correlate well with the high-quality-factor optical modes located within a frequency bandwidth centered at 3.75 THz. Figure 3.9 reports a scatter plot (top) with the relative mode suppression (MS), defined as MS = 10 $\log_{10}$ (I_{min}/I_{max}), of the experimental spectral peaks. The spectral distribution of the experimental peaks is in reasonably good correspondence with the band-edges of the computed photonic pseudo-bandgap (bottom) for a 2.9 mm-long Octonacci resonator having ridge width W = 160 µm and slit aperture L = 1.9 µm.

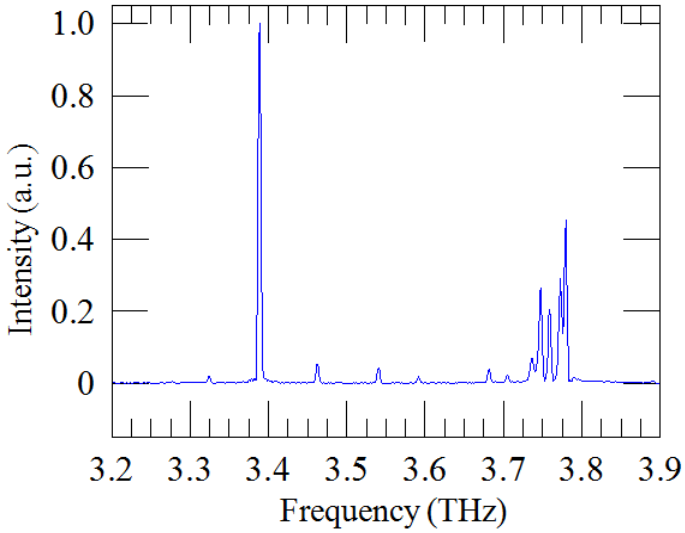

Figure 3.8: FTIR emission spectrum of an Octonacci device with slit aperture L = 1.9 µm and ridge width W = 160 µm, operated at a heat sink temperature of 12 K and a 1 %-duty cycle. Up to 13 distinct modes are visible within -20 dB mode
GHz, measured with a resolution of 0.125 cm^{-1} and averaging over 32 scans.

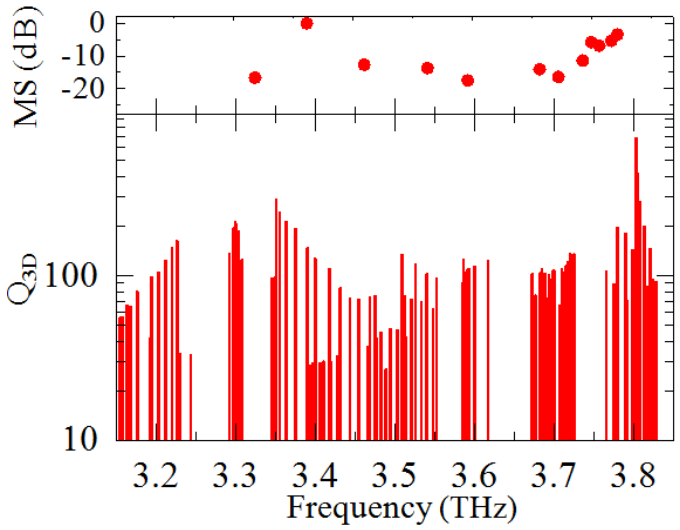

Figure 3.9: Three-dimensional FEM simulation of the quality factor of the eigenmodes for an 2.9 mm-long Octonacci laser having W = 160 µm and L = 1.9 µm. The upper panel shows the relative mode suppression (MS) of the experimental spectral peaks, directly compared to the computed photonic pseudo-bandgap. The rich multimode emission is characterized by a relatively low mode suppression with a maximum of ≈-20 dB.

3.4.2 Electrical and optical characterization of single-mode devices

Another set of devices exploiting the same 8th-order Octonacci grating but with larger slit sizes was fabricated, in order to investigate how light scattering and extraction are influenced by the slit width. LJV characteristic curves were measured while driving the devices in pulsed operation at a 1%-duty cycle with repetition rate of 50 kHz and pulse width of 200 ns, at a heat sink temperature of 20 K.

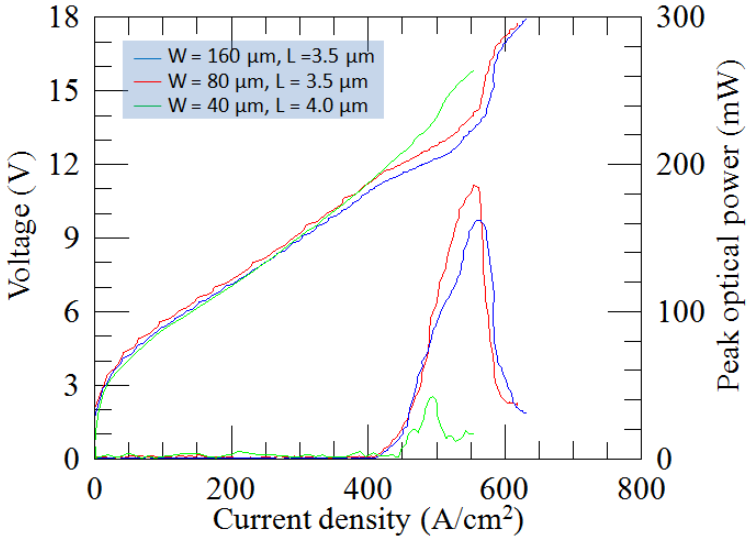

Figure 3.10: V-J and L-J characteristics of a set of 2.9 mm-long Octonacci lasers having ridge widths W = 160 µm, W = 80 µm and W = 40 µm. The slit width ranges between L = 3.5 µm (W = 80-160 µm), and L = 4.0 µm (for W = 40 µm). The L-J-V were measured at a heat sink temperature of 20 K in pulsed regime with 1 %-duty cycle (pulsed width of 200 ns and pulse repetition rate of 50 kHz). The optical power scale was corrected to take into account the radiation collection efficiency of the pyroelectric detector and the 75% transmission of the polyethylene window of the cryostat.

As shown in figure 3.10, lasers with the same slit width L = 3.5 µm and ridge width W = 80 µm and 160 µm show a similar 80 mW

By reducing the ridge width to W = 40 µm and increasing the slit width to L = 4.0 µm, the optical power drops at 40 mW, due to the decreased volume of active material available. The most powerful device (W = 80 µm; L = 3.5 µm) displays a slope efficiency of SE
and a wall-plug efficiency of about 1%, which is a record for double-metal THz QCL resonators.[113] The FTIR emission spectra reported in figure 3.11 show robust single-mode emission with a visible red shift from 3.7 THz to 3.38 THz while varying W in the 40-160 µm range.

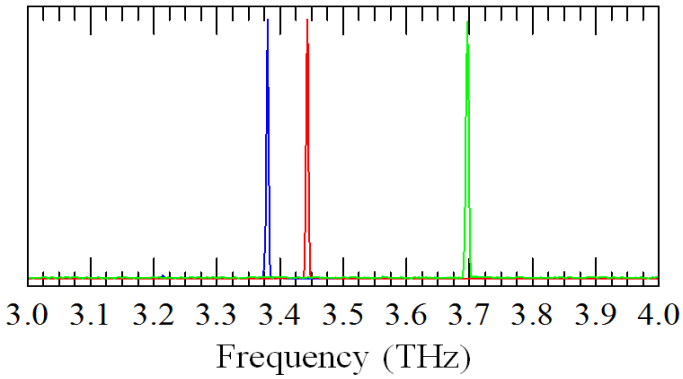

Figure 3.11: FTIR emission spectra of the single-mode devices with W = 160 µm (blue), W = 80 µm (red) and W = 40 µm (green) operated at temperature of 12 K and in pulsed mode with a duty cycle of 4%, as measured with a resolution of 0.125 cm^{-1} and a averaging over 32 scans.

Interestingly, the observed ridge width-dependent shift is in good agreement with the results of the FEM simulations. Comparing the FTIR emission spectra of the fabricated lasers, it is clear that Octonacci resonators with smaller slit aperture (L = 1.9 µm) feature richer multimode emission, while larger slit sizes (L = 3.5 µm, 4 µm) induce much narrower spectral bandwidth, irrespective of the device width W. To further investigate this effect, numerical simulations of the three-dimensional quality factors of the larger slit resonators were performed and compared to the experimental FTIR spectra. Figure 3.12 shows a scatter plot (top) with the relative mode suppression (MS), of the experimental emission peaks for a device with L = 3.5 µm and W = 160 µm. The comparison between the MS factor and the quality factors of the optical modes (bottom) in the investigated frequency bandwidth highlights the presence of multiple, narrow pseudo-bandgap. The mode with highest quality factor lying at the band-edge of the photonic pseudo-bandgap centered at 3.4 THz correlates well with the most intense experimental spectral line at 3.38 THz, while the very -23 dB, is very close to the pseudo-bandgap edge computed at about 3.25 THz.

3.4.3 Far-field beam profiles

The far-field intensity profiles emitted by the Octonacci lasers were measured by scanning a pyroelectric detector mounted on a motorized stage along a spherical surface. Figure 3.13a reports the far-field distribution of multi-mode Octonacci laser having W = 60 µm and L = 1.9 µm, operated in pulsed regime with a 1%-duty cycle, at a heat sink temperature of 20 K and at the maximum

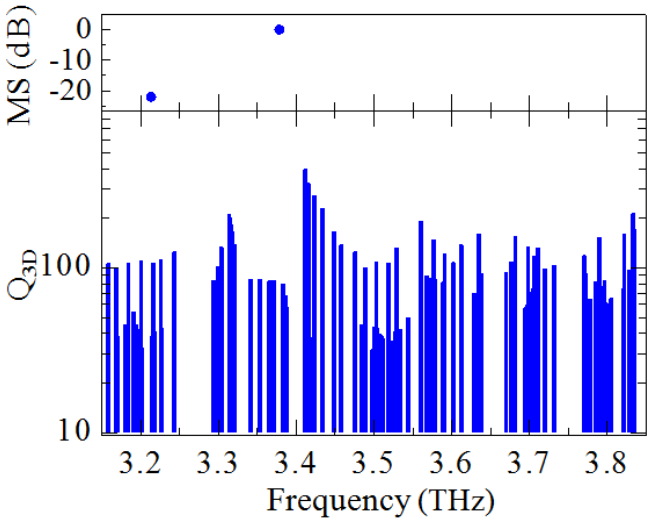

Figure 3.12: Results of the three-dimensional FEM simulation of the quality factor of the eigenmodes for a 2.9 mm-long Octonacci laser having W = 160 µm and L = 3.5 µm. The experimental MS is reported in the upper scatter plot, showing a more effective mode suppression with respect to the case of a laser with L = 1.9 µm.

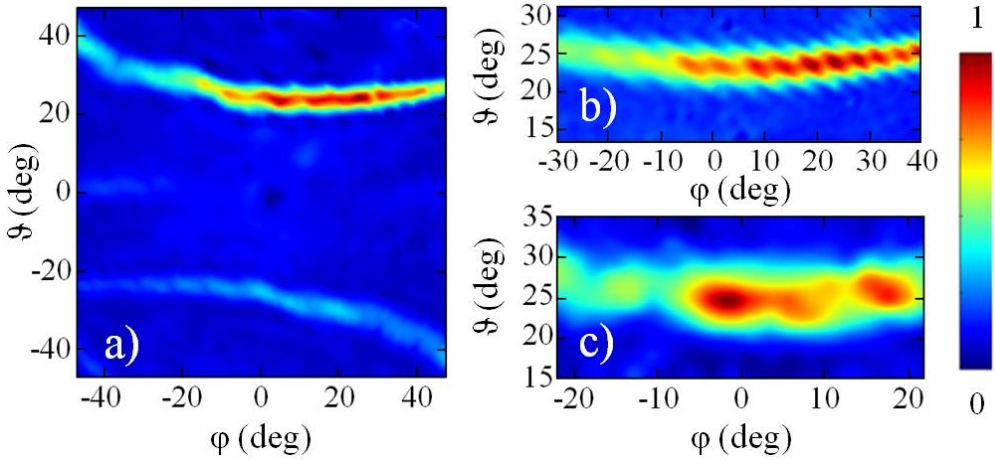

Figure 3.13: a) Far-field intensity pattern of an Octonacci laser having W = 60 µm and L = 1.9 µm, measured by scanning the pyroelectric detector on a spherical surface at a distance of 7 cm from the laser top plane. The laser was driven in pulsed mode (50 kHz , 200 ns), at a heat sink temperature of 20 K and at J =500 A/cm^2. Plot of the most intense far-field emission lobes for the device with W = 60 µm (as also included in fig. 2d) and **f)** of the brightest lobe for the laser having W =160 µm, featuring the same slit aperture L = 1.9 µm. Both devices were operated at peak emission conditions with a 1 %-duty cycle.

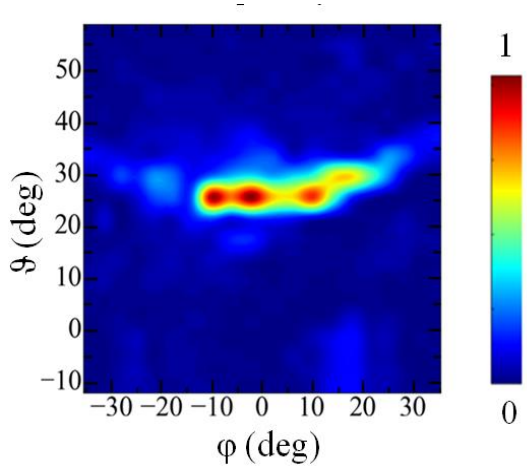

Figure 3.14: Far-field intensity patterns measured at 4 cm away from the top surface of a laser bar having W = 160 µm and L = 3.5 µm, by keeping the heat sink temperature fixed at 15 K with a duty cycle of 1%, at J = 550 A/cm^2.

peak optical power. The surface-emitted radiation is concentrated in two main lobes, which are elongated along the horizontal direction, at elevation angles of ≈ -25° and ≈ +25°. The most intense lobe is comprised within a spot at Δ ≈ 5° and Δφ ≈ 60°. To better compare the far-field profiles of resonators with different W, the spatial resolution of the measurement was increased to scan around the most intense lobe. The comparison between the intensity distribution patterns of two devices sharing the same Octonacci patterns and different ridge widths W = 60 (figure 3.13b) and W = 160 (figure 3.13c) shows that the main lobes have the same elevation angle ≈ +25° with a vertical divergence of ≈5°, as expected in case of photonic structures based on the same grating design. Conversely, the horizontal divergence becomes narrower (Δφ ≈ 40°) when the ridge width is increased, due to the associated longer slit transverse size, which reduces the diffraction effects.

Concerning the single-mode Octonacci lasers, the beam profile of the most powerful device with W = 160 µm and L = 3.5 µm is shown in Figure 3.14, as measured at the maximum emission conditions, at a heat sink temperature of 15 K and operated in pulsed mode with a duty cycle of 1%. The single lobe beam shape is consistent with the results for the multi-mode emitting lasers, and shows a main radiation spot concentrated at an angle of 35°. The horizontal divergence in the single-mode emission case is slightly narrower than that of the multimode devices.

3.6 Discussion

In this chapter, the demonstration of highly efficient surface emission is reported realizing one-dimensional quasi-crystalline distributed feedback photonic patterns on THz QCLs. The resonator is based on a slit grating in the laser top metal surface, following the Octonacci sequence pattern and controlling the light feedback and extraction mechanisms in the cavity. By finely tuning the slit width and the ridge width, the light extraction was

with an associated slope efficiency -plug

her with low-divergence, double-lobed emission patterns. Octonacci lasers with larger slit width (L = 3.5 μm, 4.0 μm) emit in stable single-mode operation within the spectral gain bandwidth of the used active material. Instead, quasi-crystal resonators with smaller aperture size (L = 1.9 μm) feature a rich multimode emission spectrum over a maximum

simulations. Interestingly, this multimode emission can also be manipulated to achieve fine-tuning of selected spectral lines by means of an external cavity coupled to the emitted radiation, as detailed with experiments and simulations in Chapter 5.

CHAPTER 4:
TWO-DIMENSIONAL TERAHERTZ RANDOM LASERS

4.1 Introduction

In this chapter, the design of the first THz random quantum cascade lasers (QCLs) operating in continuous-wave is discussed, as well as the experimental investigation of their performance in both pulsed and continuous-wave regimes. Unlike the one-dimensional aperiodic photonic resonators introduced in the previous chapters, two-dimensional random structures exploit fully a disordered distribution of scatterers, derived from a non-deterministic generation rule: due to the larger dimensionality of the devised random resonators, more complex interference patterns are possible for the propagating photons, giving rise to an inherently rich multimode emission. Similarly to deterministic two-dimensional resonators encompassing quasi-crystal patterns [30,31], light undergoes multiple elastic scattering events, which is indeed due to the random spatial variation of the dielectric function. Therefore the light feedback mechanisms do not require any facets, mirrors or a properly defined cavity, very differently from conventional lasers. Anyhow, random lasers (RLs) still require an active medium for the amplification of radiation.

Random optical systems are among the most complex structures in photonics, featuring fascinating properties owing to their intrinsic structural disorder. Theoretical and experimental studies of random optical systems [71,114] have explored semiconductor powders [115], optical fibers [116], novel photonic glass materials [117], and biological tissues [118]. In all cases, disorder induces intense multiple elastic scattering of light wavelets, inducing either extended or localized states of light inside the material, which are known as Anderson states [119] in analogy with their electronic counterpart. In RLs, the emitted photons can be amplified and scattered many times in the gain medium, preserving the phase relation of the wavelets. The resulting rich interference scheme determines both the frequency and the spatial distribution of the electromagnetic modes, featuring a different degree of localization [70]. Due to the complex interplay between the intrinsic disorder and the nonlinearity of a random active medium [73, 74, 76], intriguing physical phenomena, such as gain competition and nonlinear wave mixing of the optical modes [75] may take place in RLs. Random lasing has been demonstrated in an optically-pumped suspended micro-particle laser dye [79], fine powders [120], bone tissues [81]

and, more recently, in electrically-pumped QCLs, emitting in the mid-IR [82] and THz [32-34] regions of the electromagnetic spectrum. Different photonic approaches have been reported in THz quantum cascade RLs, such as architectures based on air pillars [32], semiconductor pillars [33] or a combination of semiconductor and metal pillars [34]. All the mentioned examples obtained random patterning by etching through the entire active region, demonstrating emission over a 300-400 GHz bandwidth, with peak optical powers ranging from hundreds of microwatts [34] to few tens of milliwatts [32 $_r$ < 10%. Random lasing was only observed at low duty cycles (up to 4%) and at low (5 K) operating temperatures. Indeed, such performance limitations derived from the poor thermal management of the large device areas, needed to ensure a sufficient gain in the radiative optical modes following fabrication of the deep-etched pillars. Miniaturized, electrically pumped RLs, operating in a continuous-wave (CW) regime, are necessary for many spectroscopic and multicolor imaging applications across the THz frequency range. But, CW operation of an RL has yet to be demonstrated at THz frequencies, whether optically or electrically pumped, in the infrared region of the electromagnetic spectrum.

In this chapter, a new double-metal resonator geometry is introduced, with its 2D random distribution of air holes, patterned into the top metal surface, combined with irregular borders to confine the active region. Patterning is, however, only implemented in the upper metal and in the highly doped semiconductor cladding, so that the underlying active region core is left unperturbed. We thus overcome the previous technological limitations with THz RLs, demonstrating the first multimode CW emission. The interference pattern of our RLs has been controlled by accurately engineering the geometric properties of the photonic structures, and by investigating the effects of disorder on power extraction and spectral emission. Narrow-divergence, vertical

to a 115 K heat sink temperature

. [41] As reported in the next chapter 5, fine-tuning of the RL emission spectra is achieved coupling the resonator with an external cavity, obtaining a maximum continuous frequency shift of 11 GHz.

4.2 Random laser design

4.2.1 Design and pattern generation algorithm

The proposed RL architecture employs a QCL active medium sandwiched between two metallic cladding layers forming a double-metal waveguide and ensuring tight confinement of the THz radiation in the growth direction (z-axis) with a nearly unitary confinement factor. Light propagates in the orthogonal x-y plane, producing an almost ideal 2D photonic resonator. The random photonic structure is implemented by lithographically defining circular holes of radius r on the top metal surface, which enable simultaneous control of the optical feedback and extraction mechanisms. The high refractive index optical contrast between the gold-coated semiconductor and the air holes provides the multiple scattering cal

ed 1struc.02q01(c)457 f21aax a[(e)4is fiposein -

scatterers to enhance the optical feedback and extraction mechanisms. The high refractive index optical contrast between the gold-coated semiconductor and the air holes provides the multiple scattering cal(e)7(ed 1struc.02q01(c)457 f21aax a[(e)4is fiposein -5.8(i)-2.2(n)-7.1(t)-6.1(o)-7.8(t)-5.8(h)-2.2(e)-7.1(a)-6.1(i)-7.8(r)-5.8(.)-2.2(T)-7.1(h)-6.1(e)-7.8(r)-5.8(e)-2.2(f)-7.1(o)-6.1(r)-7.8(e)-5.8(,)-2.2(t)-7.1(h)-6.1(e)-7.8(l)-5.8(i)-2.2(g)-7.1(h)-6.1(t)-7.8(p)-5.8(r)-2.2(o)-7.1(p)-6.1(a)-7.8(g)-5.8(a)-2.2(t)-7.1(e)-6.1(s)-7.8(i)-5.8(n)-2.2(t)-7.1(h)-6.1(e)-7.8(o)-5.8(r)-2.2(t)-7.1(h)-6.1(o)-7.8(g)-5.8(o)-2.2(n)-7.1(a)-6.1(l)-7.8(x)-5.8(-)-2.2(y)-7.1(p)-6.1(l)-7.8(a)-5.8(n)-2.2(e)-7.1(,)-6.1(p)-7.8(r)-5.8(o)-2.2(d)-7.1(u)-6.1(c)-7.8(i)-5.8(n)-2.2(g)-7.1(a)-6.1(n)-7.8(a)-5.8(l)-2.2(m)-7.1(o)-6.1(s)-7.8(t)-5.8(i)-2.2(d)-7.1(e)-6.1(a)-7.8(l)-5.8(2)-2.2(D)-7.1(p)-6.1(h)-7.8(o)-5.8(t)-2.2(o)-7.1(n)-6.1(i)-7.8(c)-5.8(r)-2.2(e)-7.1(s)-6.1(o)-7.8(n)-5.8(a)-2.2(t)-7.1(o)-6.1(r)-7.8(.)-5.8(T)-2.2(h)-7.1(e)-6.1(r)-7.8(a)-5.8(n)-2.2(d)-7.1(o)-6.1(m)-7.8(p)-5.8(h)-2.2(o)-7.1(t)-6.1(o)-7.8(n)-5.8(i)-2.2(c)-7.1(s)-6.1(t)-7.8(r)-5.8(u)-2.2(c)-7.1(t)-6.1(u)-7.8(r)-5.8(e)-2.2(i)-7.1(s)-6.1(i)-7.8(m)-5.8(p)-2.2(l)-7.1(e)-6.1(m)-7.8(e)-5.8(n)-2.2(t)-7.1(e)-6.1(d)-7.8(b)-5.8(y)-2.2(l)-7.1(i)-6.1(t)-7.8(h)-5.8(o)-2.2(g)-7.1(r)-6.1(a)-7.8(p)-5.8(h)-2.2(i)-7.1(c)-6.1(a)-7.8(l)-5.8(l)-2.2(y)-7.1(d)-6.1(e)-7.8(f)-5.8(i)-2.2(n)-7.1(i)-6.1(n)-7.8(g)-5.8(c)-2.2(i)-7.1(r)-6.1(c)-7.8(u)-5.8(l)-2.2(a)-7.1(r)-6.1(h)-7.8(o)-5.8(l)-2.2(e)-7.1(s)-6.1(o)-7.8(f)-5.8(r)-2.2(a)-7.1(d)-6.1(i)-7.8(u)-5.8(s)-2.2(r)-7.1(o)-6.1(n)-7.8(t)-5.8(h)-2.2(e)-7.1(t)-6.1(o)-7.8(p)-5.8(m)-2.2(e)-7.1(t)-6.1(a)-7.8(l)-5.8(s)-2.2(u)-7.1(r)-6.1(f)-7.8(a)-5.8(c)-2.2(e)-7.1(,)-6.1(w)-7.8(h)-5.8(i)-2.2(c)-7.1(h)-6.1(e)-7.8(n)-5.8(a)-2.2(b)-7.1(l)-6.1(e)-7.8(s)-5.8(i)-2.2(m)-7.1(u)-6.1(l)-7.8(t)-5.8(a)-2.2(n)-7.1(e)-6.1(o)-7.8(u)-5.8(s)-2.2(c)-7.1(o)-6.1(n)-7.8(t)-5.8(r)-2.2(o)-7.1(l)-6.1(o)-7.8(f)-5.8(t)-2.2(h)-7.1(e)-6.1(o)-7.8(p)-5.8(t)-2.2(i)-7.1(c)-6.1(a)-7.8(l)-5.8(f)-2.2(e)-7.1(e)-6.1(d)-7.8(b)-5.8(a)-2.2(c)-7.1(k)-6.1(a)-7.8(n)-5.8(d)-2.2(e)-7.1(x)-6.1(t)-7.8(r)-5.8(a)-2.2(c)-7.1(t)-6.1(i)-7.8(o)-5.8(n)-2.2(m)-7.1(e)-6.1(c)-7.8(h)-5.8(a)-2.2(n)-7.1(i)-6.1(s)-7.8(m)-5.8(s)-2.2(.)-7.1(T)-6.1(h)-7.8(e)-5.8(h)-2.2(i)-7.1(g)-6.1(h)-7.8(r)-5.8(e)-2.2(f)-7.1(r)-6.1(a)-7.8(c)-5.8(t)-2.2(i)-7.1(v)-6.1(e)-7.8(i)-5.8(n)-2.2(d)-7.1(e)-6.1(x)-7.8(o)-5.8(p)-2.2(t)-7.1(i)-6.1(c)-7.8(a)-5.8(l)-2.2(c)-7.1(o)-6.1(n)-7.8(t)-5.8(r)-2.2(a)-7.1(s)-6.1(t)-7.8(b)-5.8(e)-2.2(t)-7.1(w)-6.1(e)-7.8(e)-5.8(n)-2.2(t)-7.1(h)-6.1(e)-7.8(g)-5.8(o)-2.2(l)-7.1(d)-6.1(-)-7.8(c)-5.8(o)-2.2(a)-7.1(t)-6.1(e)-7.8(d)-5.8(s)-2.2(e)-7.1(m)-6.1(i)-7.8(c)-5.8(o)-2.2(n)-7.1(d)-6.1(u)-7.8(c)-5.8(t)-2.2(o)-7.1(r)-6.1(a)-7.8(n)-5.8(d)-2.2(t)-7.1(h)-6.1(e)-7.8(a)-5.8(i)-2.2(r)-7.1(h)-6.1(o)-7.8(l)-5.8(e)-2.2(s)-7.1(p)-6.1(r)-7.8(o)-5.8(v)-2.2(i)-7.1(d)-6.1(e)-7.8(s)-5.8(t)-2.2(h)-7.1(e)-6.1(m)-7.8(u)-5.8(l)-2.2(t)-7.1(i)-6.1(p)-7.8(l)-5.8(e)-2.2(

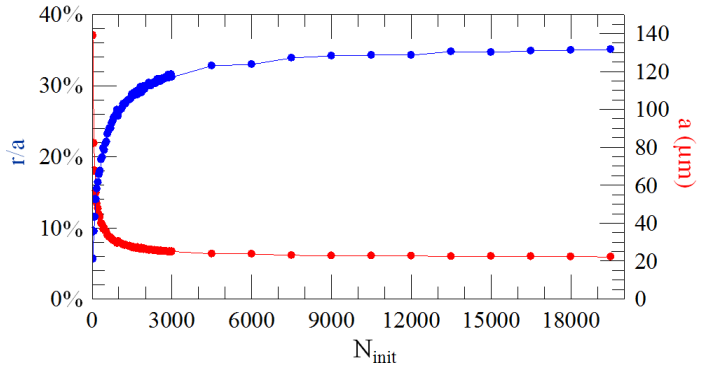

Figure 4.1: For different values of the number of holes N_{init} initially extracted, the random pattern generation code selects the fraction of non-overlapping holes and consequently produces patterns with specific filling factor r/a (blue line) and average intersite distance a (red line) for type-A patterns.

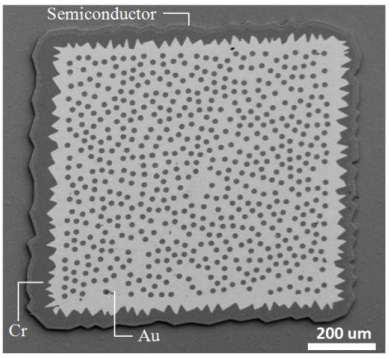

Figure 4.2: Scanning electron microscope image of a fabricated random laser, with the indicated materials of the resonator.

values of N_{init}, when the considered area is already so filled that no more holes can be added due to the edge-to-edge distance constraint. We varied r/a in the range 5% - 34% to investigate the effect of different degrees of scattering on light propagation and outcoupling to free space, resulting from the different optical confinement of the main modes [33,34]. The corresponding filling fraction of our random resonators, determined by the area of the holes with respect to the gold patterned resonator surface, was correspondingly varied in the range 2% - 36%. For type-A and type-B geometries,
chosen to provide sufficient light scattering and extraction for r/a >14%. In

fraction while maintaining the inter- so
that there is a sufficient number of holes (N > 100) from which the light can

scatter. Instead for the much smaller type-C patterns, the radius was set to an

photonic pattern is then surrounded by an irregularly shaped chromium layer

shown in the SEM image of fig. 4.2. The Cr layer was engineered to avoid overlap with the internal holes and so that its average width is kept comparable

same area, the Cr border was kept identical. This partially absorbing border helps suppress undesired electromagnetic modes, such as whispering-gallery modes having little overlap with the central random geometry; unlike in the geometry proposed in [32] such modes are here inherently suppressed by design. Two sets of devices were designed with overall device areas (including the chromium absorbing boundary) of 0.57 mm^2 (type A) and 0.70 mm^2 (type B) in order to ensure a good balance between electric power dissipation and surface-related diffraction.

4.2.2 Statistical analysis

A preliminary statistical analysis of the generated geometries can be performed by calculating their spatial autocorrelation [76], considering a simplified two-

r = x,y) across the mesa. For the metal-

the etched holes, reproducing the random spatial fluctuations of the dielectric function. The resulting autocorrelation

$$K(\Delta\mathbf{r}) = < \varepsilon(\mathbf{r})\varepsilon(\mathbf{r}+\Delta\mathbf{r}) > \tag{38}$$

is then calculated over an ensemble of 100 different random configurations at fixed hole radius and geometrical filling factors (r/a). The autocorrelation has a typical decay length called correlation radius R_c, which can be retrieved through fitting with the exponential function:

$$f(\Delta r) = A\exp(-\Delta r/R_c) + B\,\Delta r/R_2 + C \tag{39}$$

As shown in figure 4.3 for type-

-range disorder, reflected

in a sharper decay of the autocorrelation function (thin black lines). For the

c

c

-range disorder. For patterns

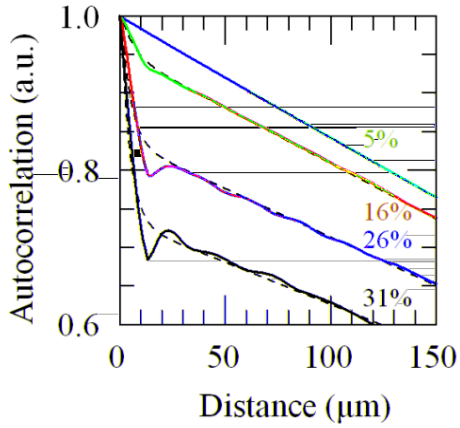

Figure 4.3: Spatial autocorrelation functions for random photonic patterns with area of 0.57 mm^2
31% and filling fractions 8%, 21%, 30%, respectively). The autocorrelation fit functions are the black dashed lines.

, however, the correlation radius reduces as r/a increases down to R_c c the structures with higher density of holes consistently exhibit a far more pronounced signature of short-range disorder.

4.2.3 Three-dimensional modeling

Figure 4.4a shows the three-dimensional schematic model of an RL with a 10 -thick active region and a resonator area of 0.57 mm^2, which was modelled using a commercial finite element method (FEM) to solve Maxwell's eigenvalue problem (see the simulation methods in Appendix C). The optical properties of the materials are implemented indicating their refractive indices, such as n_1 = 3.60 for the QCL heterostructure and n_2 = 4.43+i0.31 for the Cr-covered border. The latter effective index has an imaginary part accounting for the associated to the absorbing effects of the thin Cr layer at the resonator border, featuring irregular protrusions with a typical scale of 20 - comparable with the lasing wavelength in the material (a radiation). The Au double-metal waveguide is modelled using a perfect electric conductor (PEC) condition above and below the semiconductor mesa. The external air has n_{Air} = 1, and the outcoupling of light to free space is mimicked with scattering boundary conditions around the simulated region.

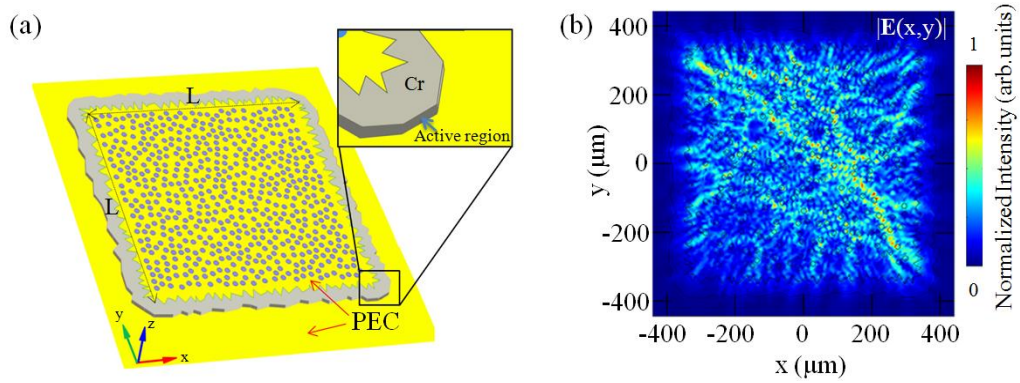

Figure 4.4: a) Schematics of a random resonator model for the FEM computation, with the indication of the Cr border, the active region and gold-patterned surface, with average side length L. b) Electric field modulus |E(x,y)| across the center for the RL resonator, calculated at -A device

For small r/a = 5%, the computations show that the propagation of the optical modes in the resonator is characterized by a quasi-ballistic regime, as intuitively expected owing to the large average inter-site separation due to the low hole density. Conversely, a higher r/a provides a stronger light scattering mechanism, with a much richer interference which produces resonating eigenmodes with a complex electric field distribution; this is illustrated in Fig. 4.4b for a type- and filling fraction 13%

The resonator supports a large number of eigenmodes with a relatively low three-dimensional quality factor Q_{3D} <120 over the investigate frequency range (2.65 - 3.45 THz), as shown in fig. 4.5 for a resonator with area of 0.57 mm^2. This indicates that the generated random patterns do not provide a highly selective feedback on only a few modes, but instead the disordered structure inherently acts over a broad range of frequencies. Even though both weakly localized and extended modes show a very irregular electric field intensity profile, typically the weakly localized modes possess a larger Q_{3d} owing to the tighter light confinement. Since there is a large number of orthogonal electromagnetic eigenmodes that partially overlap inside the resonator, local gain mode competition plays a crucial role in the build-up of the effective lasing modes, as is typical of RLs [75]. Since it is extremely challenging to include such a quantum treatment in the FEM simulations of our RLs [121,122], even in 2D, it is not feasible to investigate numerically the local gain mode

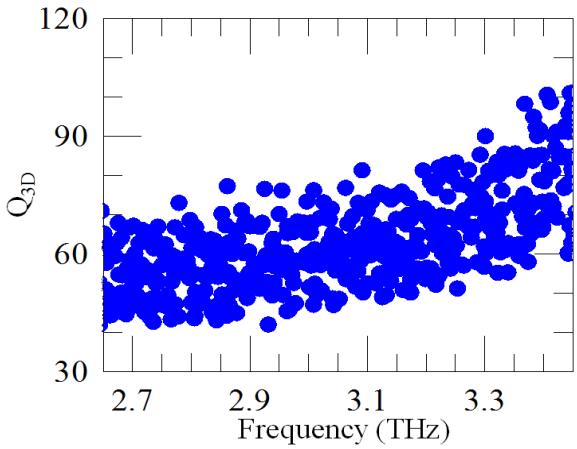

Figure 4.5: Plot of the three-dimensional quality factors Q_{3D} of the eigenmodes of a type-A resonator with r = 8 µm, r/a = 20% and filling factor 13%, as a function of the eigenfrequency as computed with the FEM simulation.

competition dynamics more deeply, or how this influences the steady-state resonating electric fields and the resulting emission frequencies.

From the 3D simulations we can however provide an estimate of the photon $_r$. The vertical radiative losses have been indeed included in the quality factor computation ($Q_{vertical}$), so that the extraction efficiency can be quantitatively assessed. We assume that the $_{3D}/Q_{vertical}$ being $Q_{3D} = (1/Q_{ohmic} + 1/Q_{vertical})^{-1}$. From the 3D simulations we extract an average quality factor for the operating spectral range of our random lasers Q_{3D} =100, ^{3D} $_{3D}$ $^{-1}$. The computed photon loss rate due to surface emission of the $_r$ ~ 5 GHz, corresponding to a $Q_{vertical}$ $_r$ ~16%. Furthermore, the related Q_{ohmic} $_{ohmic}$ channel is expected to be the non-radiative in- $_{ohmic}$ $^{-1}$.

4.3 Fabrication methods

The fabrication of the proposed quantum cascade random lasers required a series of cleanroom techniques detailed in Appendix B. The GaAs/$Al_{0.15}Ga_{0.85}$As QCL active material is a hetereostructure grown by molecular beam epitaxy on an undoped GaAs substrate. The active region

features a three-quantum-well architecture, with a single extractor well [96]. The layer sequence is **5.5**/11.0/**1.8**/11.5/**3.8**/9.4/**4.2**/<u>18.4</u> (in nm), where $Al_{0.15}Ga_{0.85}As$ layers are shown in bold face, GaAs in roman font, and the underlined number indicates a Si-doped layer with a density of $2\ 10^{16}\ cm^{-3}$. The active region is capped by a 700 nm-thick highly doped ($2\ 10^{16} cm^{-3}$) GaAs contact layer, with a $Al_{0.5}Ga_{0.5}As$ etch-stop layer on the top. After growth, Au-Au thermocompressive wafer bonding of the QCL wafer onto an n+-GaAs carrier wafer was performed. After selective wet etching of the host GaAs substrate and the $Al_{0.5}Ga_{0.5}As$ etch-stop layer, the active region was coated with a top metal layer of Cr/Au (5 nm/150 nm). By using a combination of electron beam lithography (EBL) and optical lithography, the sample surface was patterned with air holes, whose center positions were placed with a uniform distribution in a square, as defined by a custom Matlab code. Three sets of devices were fabricated with different areas (0.57 mm^2 for type A; 0.70 mm^2 for type B; 0.06 mm^2 for type C), varying the radius r and number of scatterers N to - 34% and corresponding filling fractions in the range 2%-36%. The holes are comprised within a central square region having hand- -wide gold strip. The 700-nm-thick n+ top contact layer was totally removed from below the etched holes by means of a reactive-ion etching (RIE) process, so that optical losses are minimized.

Strongly absorbing boundary conditions were then realized by adding an external 7-nm-thin Cr border on the active region via optical lithography, with

specifically designed to have size comparable to the expected lasing

the Cr border was not etched away in order to ensure the suppression of modes extending towards the edge of the devices, as the Cr border acts as a protective mask for the underlying active core during the ICP-RIE process, though it is partially removed by the process. Finally, the mesa was etched down using a second ICP-RIE process, calibrated to optimize the vertical sidewalls of the border spikes (figure 4.6) and to avoid lateral current spreading. After processing, individual devices were indium soldered onto a copper submount and wire-bonded regularly along the perimeter to minimize the perturbation of the far-field emission profile and ensure uniform current injection.

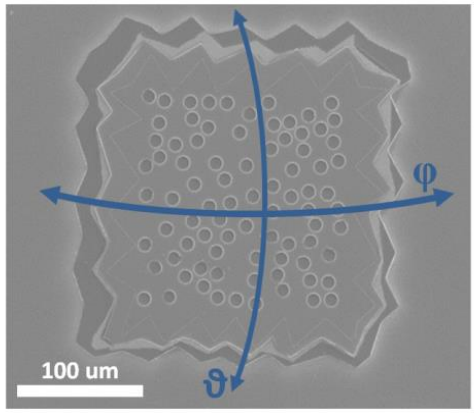

Figure 4.6: SEM image of a RL with area 0.06 mm^2 (type C), r/a = 28%, filling fraction 25%
-field emission experiments are marked in blue.

4.4 Experimental results

4.4.1 Electrical and optical characterization in pulsed regime

Based on the simulation analysis and employing the above-mentioned fabrication techniques, a set of QCL RLs were fabricated using a combination of optical, electron beam lithography, metal deposition and dry-etching techniques. We swept a large range of geometrical filling factors, moving from very low-density random photonic patterns to closely-packed configurations of scatterers. A first batch of devices (type-A, area = 0.57 mm^2) comprises two four

(type-B, area = 0.70 mm^2

30%, and 34%.

A comparison between the pulsed-mode current density-voltage (J-V) and power-current density (L-J) characteristics of type-

(Fig. 4.7

decreases by increasing r/a for a fixed hole radius r. A maximum peak power of

aximum wall-plug efficiency (WP For type- . 4.8a) and r b), measured under the same experimental conditions of figure

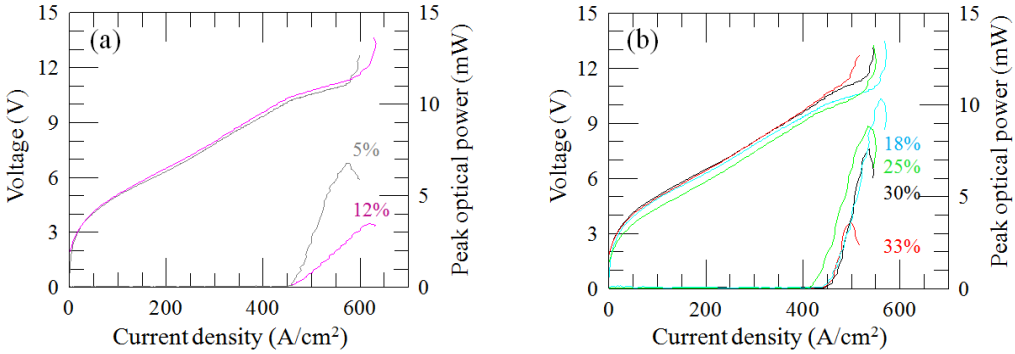

Figure 4.7: a) Plot of the current density-voltage (J-V) and current density-peak optical power (J-L) curves for RLs having an area of 0.57 mm^2
values are labeled on the graph; their filling fractions range between 2% (top curve) and 5% (bottom curve). b) J-V and J-L characteristics for type-
are on the graph; the corresponding filling fractions are 10%, 20%, 28%, 34% (from top to bottom). All LJV measurement were acquired at a heat sink temperature of 15 K, driving the lasers with a pulse width of 200 ns and a repetition rate of 50 kHz (i.e. a 1%-duty cycle) in a nitrogen-purged environment. Optical power scales were corrected with the detector collection efficiency (integrating the optical power over the 3D far-field intensity pattern) and the absorption of the polyethylene cryostat window (75%).

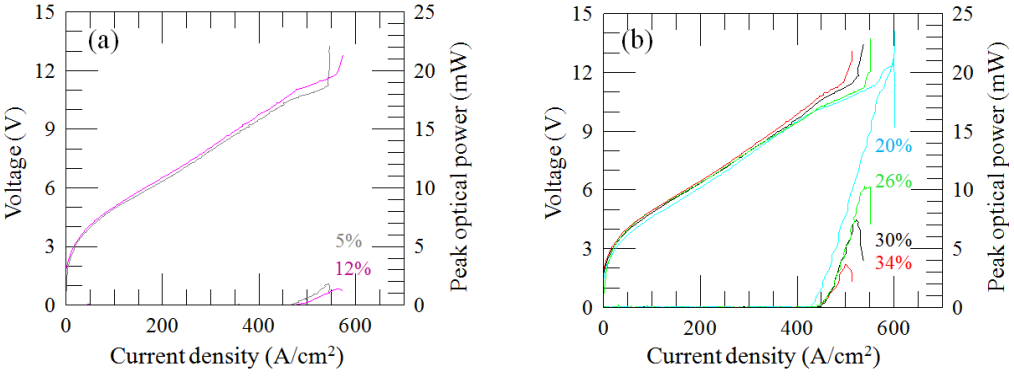

Figure 4.8: J-V and J-L curves for RLs having an area of 0.70 mm2 (type B) and hole radii: (a) r
corresponding
filling fractions are: (c) 2% (top curve) and 5% (bottom curve); (d) (from top to bottom: 13%, 21%, 28%, 36%).The measurements were acquired in the same conditions of figure 4.7.

4.7, confirms that the detected optical power decreases with increasing r/a at a fixed hole radius r. This correlates with the stronger optical confinement achieved for larger gold-

quantum efficiency of 1.5 with a WP of 0.04%.

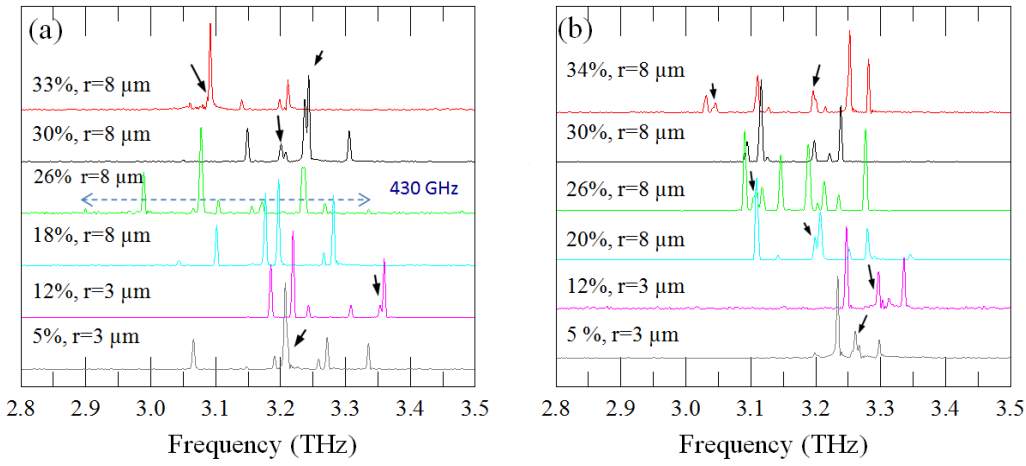

Figure 4.9: a) FTIR emission spectra of the RLs of fig. D7, having different *r/a* (and filling fractions) and area 0.57 mm^2 (type A). The spectra were measured in rapid scan mode using an internal DTGS pyroelectric detector. The lasers were driven with 200-ns-long pulse at a repetition rate of 50 kHz, at the operating current value corresponding to the peak power condition; the heat sink temperature was 8 K. b) FTIR emission spectra of the RLs of fig. D8, with area 0.70 mm^2 (type B) and different *r/a* (and filling fractions) measured under the same experimental conditions as (a). The black arrows in the panels indicate a spectral splitting of spatially overlapping modes.

In the type-A RLs, the dynamic range strongly depends on the values of the geometrical filling factor and of the hole radius. The threshold current density J_{th} only varies weakly in type-A RLs for different values of r/a (between (J_{th} = 410 - 450 A/cm^2), which indicates the optical losses are not deeply altered within the spanned geometric parameters. Instead the current density at the peak optical power (J_{max}), is more strongly affected by r/a, because of the sharp decrease of the optical power and total efficiency at increasing r/a. With r = 3

$_{max}$ reaches a value of 620 A/cm^2 for r/a = 12%, whilst for devices with r =

^{2} for r/a = 33%.

In a similar way, for type-B devices, J_{th} varies between 410 A/cm^2 and 450 A/cm^2, while J_{max}

^{2}

500 A/cm^2 (r/a = 34%).

The FTIR emission spectra show that all RLs studied here (type A, area 0.57 mm^2, fig.4.9a; type B, area 0.70 mm^2, fig. 4.9b) feature a rich multimode emission, mostly comprising sharp, uncorrelated spectral peaks [115]. Some spectra also feature additional closely spaced spectral lines around J_{max}, which can barely be resolved within the FTIR spectral resolution. The emitted spectral

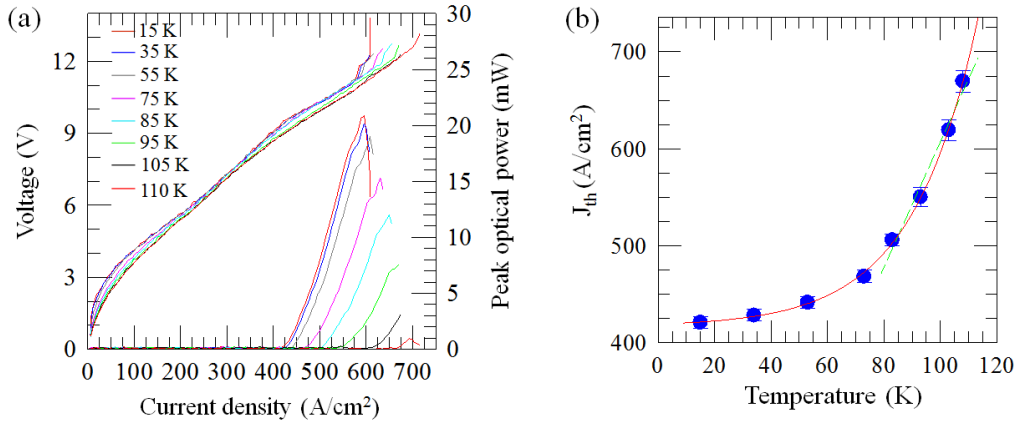

Figure 4.10: a) J-V and J-L curves of the type-B laser with r/a = 20%, filling fraction 13%, r = 8 [2]; devices were measured at different heat sink temperature whilst driving the device with 200-ns-long pulses at a repetition rate of 15 kHz, i.e., 0.3%-duty cycle. b) Threshold current density, Jth, as a function of the heat sink temperature. The red line shows the fit with the phenomenological formula $J_{th}(T) = J_1 + J_2 e^{T/T2}$, while the green dashed line is the linear fit for T 80 K.

lines cover, in the best case, a 430 GHz-wide spectral bandwidth, slightly narrower than the active region gain bandwidth. This can be correlated to the expected gain competition mechanism in RLs, which eliminates the low-Q, spatially separated, modes and can couple out relatively high-Q factor electromagnetic modes with spatial overlap [123]. The frequency separation between adjacent spectral lines is strongly variable in all the spectra, with spacing varying from a minimum of 10-20 GHz to a maximum of 60-90 GHz. No signatures of regularly spaced Fabry-Perot or whispering-gallery modes are present in the FTIR spectra. Indeed, this is as expected owing to the action of the irregular, absorbing chromium border that suppresses all modes extending to the edges of the device, preserving only the ones confined in the center of the random photonic resonator. As a representative example of the rich spectrum of type-A resonators, the RL having r/a = 26% (fig. 4.9a) features ten emission spectral lines spanning a 430 GHz bandwidth, with a peak centered at 3.24 THz, whose half-

FTIR resolution. This indicates that a number of spectrally unresolved modes may co-exist around that frequency. Among type-B devices, the RL having r/a = 34% shows 11 distinct spectral lines (fig. 4.9b), distributed over a 300 GHz bandwidth. Many RLs clearly show a spectral splitting of spatially overlapping modes. In turn, the characteristic presence of multiple lasing modes with

uncorrelated wavefronts determines a low degree of spatial coherence of the laser emission. Remarkably, all fabricated RLs operate up to a maximum heat sink temperature of T_H = 115 K, corresponding to a lattice temperature T_L 120 K [97] as reported in figure 4.10a. The characteristic temperature T_0 = (107 ± 9) K, retrieved by fitting the curve in figure 4.10b with the expression $J_{th}(T)$ $J_0 \exp(T/T_0)$, is comparable with the T_0 value measured for a standard double- confirms that the high-temperature performance of the active region is not damaged by the implemented random photonic structure: the multiple scattering dynamics governing the optical feedback does not perturb the thermal performance of the QCL active material. The corresponding maximum peak optical power is, K) as the heat-sink temperature is increased.

4.4.2 Far-field beam profiles in pulsed regime

The far field intensity profiles of the fabricated devices were measured by moving a pyroelectric detector on a sphere with a 5 cm radius centred on the laser. The surface patterns of representative type-A RLs show in figures 4.11a - 4.11c indicated a well concentrated laser emission spot comprised in an angular

to 26%. In contrast, type-B RLs having a larger area (0.70 mm^2) show a more irregular emission as reported in figures 4.11d - 4.11f with a central spot

intense lobes. The different behaviors are determined by the complex interference patterns of the electromagnetic modes in RLs exploiting different random patterns: due to the possible co-existence of localized and extended modes, the resulting overall far-field intensity pattern is strongly influenced by the specific filling fraction, hole radius r and resonator size.

4.4.3 Continuous-wave THz random laser

Continuous-wave (CW) random lasing was demonstrated with the investigation of another set of resonators (type-C) with a reduced overall device area of 0.06 mm^2

the mesa and the absorbing chromium border was kept, yet with a reduced perimeter, to suppress electromagnetic fields extending to the mesa edge.

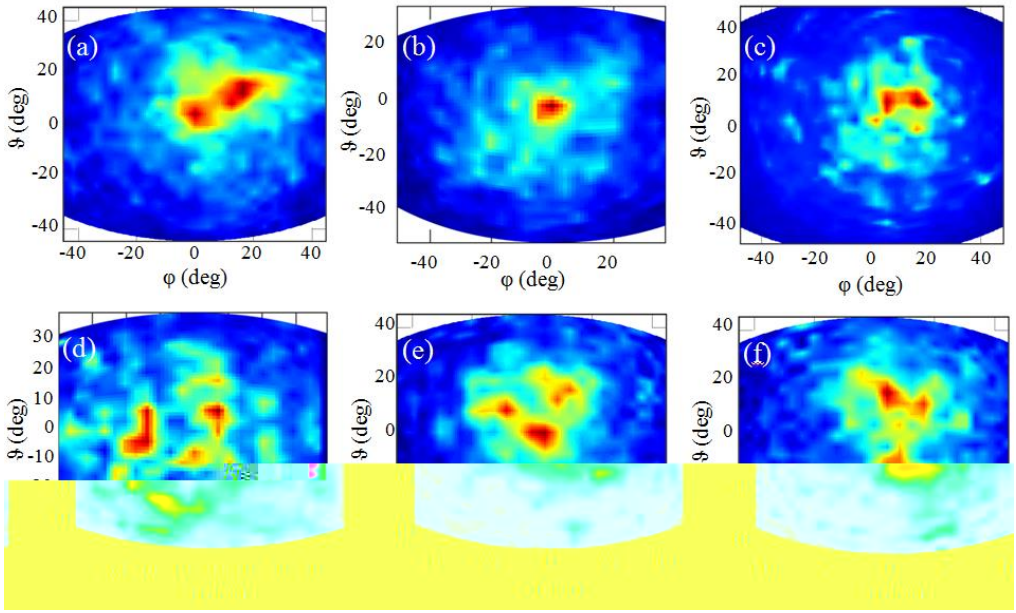

Figure 4.11: a c Far-field intensity patterns measured in pulsed mode (pulse width 200 ns; repetition rate 50 kHz), at a heatsink temperature of 15 K for RLs with area 0.57 mm^2 (type A):

a pyroelectric detector on a sphere with a 5 cm radius centred on the laser surface. The corresponding filling fractions are listed in the caption of Fig. 2a c. d f Far-field intensity patterns measured under the same experimental conditions for RLs with area 0.70 mm^2 (type

Indeed, the typical protrusion size of the Cr border was maintained around 25

with the smaller area covered by the photonic pattern.

mW at a heat sink temperature of 15 K, reaching a differential quantum efficiency of 3.0 and a maximum operating temperature T_H = 63 K, 97]. For comparison, the L-I CW characteristic measured at 15K in a Fabry-Perot (F-P) double-metal THz QCL, fabricated from the same active region and with the same area is shown on the graph. Due to the increased radiative losses in the RL, the threshold current density of the random laser is 15% higher than that of the corresponding F-P laser. Indeed, in a double-metal waveguide the waveguide losses are estimated to be as high as 20 cm^{-1}, while the typical mirror losses are around 1 cm^{-1} $_{tot}$ = 21cm^{-1}. In the reported random lasers,

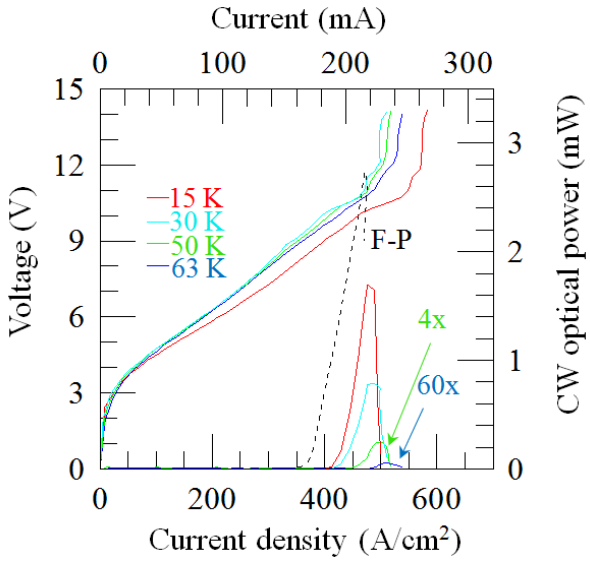

Figure 4.12: J V and J L curves for a type-C RL with r/a = 18% (filling fraction 10%) operating CW at heat-sink temperatures between 15 and 63 K and measured in a nitrogen-purged environment. The optical power is rescaled to take into account the absorption of the poly-4-methylpentene-1 (TPX) window (78%). The dashed line represents the J L characteristic of a Fabry Perot double-metal QCL having comparable area.

$_{tot}$ $_{3D}$ $_{w}$ = 23.7 cm^{-1}, so the threshold current density discrepancy can be attributed to the differences in the larger radiative losses due to the presence of the extraction hole patterns in the top metal. Consistently, the differential quantum efficiency of the F-P laser is 2.07, which is lower than that of the random laser. The FTIR CW emission spectra reported in fig. 4.13a show that all type-C devices feature multimode emission covering a 200 GHz bandwidth, for r/a ranging between 18% and 28%. Similarly to type-A and type-B devices, adjacent emission lines in type-C devices are separated by an irregular frequency spacing, which cannot be associated with whispering-gallery or Fabry-Perot modes. The far-field emission profile of the CW-operating random lasers shows multi-lobe emission, as reported in figure 4.13b with a main spot

miniaturized device cavity.

4.5 Discussion

Random lasers feature laser emission with a very high degree of second-order coherence, which is a measure of the fluctuations of the intensity and an easily tunable spatial coherence [124], which describes the correlation between waves

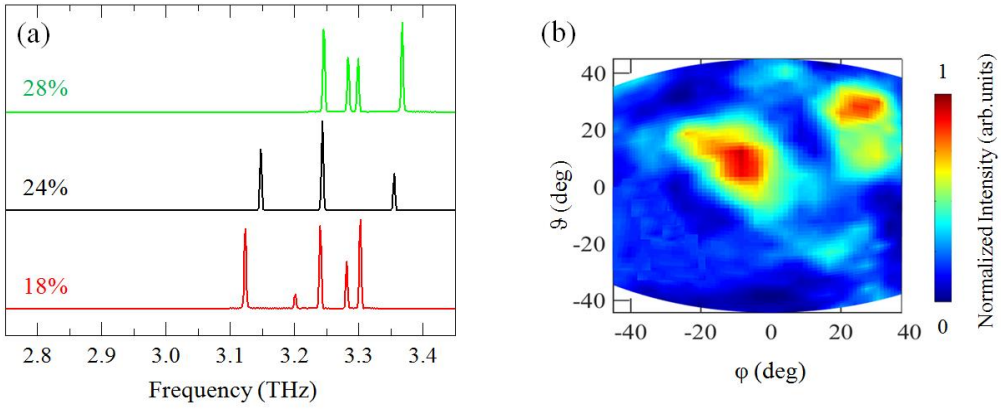

Figure 4.13: a) CW FTIR emission spectra for type-C random lasers with same area (0.06 mm^2), different r/a, indicated on the graph (ie., filling fractions 10%,14%, 21% from bottom to top), measured at a current corresponding to the peak output power; acquisition was performed with a spectral resolution of 0.125 cm^{-1}, and at a heat sink temperature of 15 K. b) Far-field pattern emitted by a type-C RL with r/a= 18%, measured under the same operating conditions as in (a). The spherical coo -field emission experiments are indicated in figure D6.

at different points in the space. The temporal distribution of photons exhibits poissonian statistics, just like a regular laser [125,126], in condition of diffusive scattering and no coherent feedback, above threshold. In this context, electrically pumped random THz lasers offer the potential to be quantum engineered to provide high-radiance, spatially incoherent emission (due to the existence of independent lasing modes with uncorrelated wave-fronts) for imaging applications free of coherent artifacts, like spatial cross-talk or speckles [127].

Furthermore, miniaturized THz random lasers can be highly appealing for applications like blood-flow monitoring during treatment and surgery [128] and high-speed parallel inspection, medical diagnostics [129]. Moreover, the proposed concept can also be exploited to engineer electrically-driven THz random lasers based on Anderson-localized modes, for example by scaling the geometry one-dimensional lattices, which inherently tend to have much shorter localization lengths. As reported in the next Chapter 5, the complex behavior of the fabricated random THz QCLs was further investigated to achieve fine control over the emission spectra, by coupling the radiation to either an external cavity or to multilayer graphene.

CHAPTER 5:
MODE DYNAMICS WITH EXTERNAL MICRO-CAVITY & GRAPHENE

5.1 Introduction

The mode dynamics in THz quantum cascade lasers integrating aperiodic photonic structures is influenced by the presence of disorder, which typically induces multiple elastic scattering of light [71], complex interference schemes and different degrees of localization of the electromagnetic modes in one-dimensional [130] and two-dimensional [131] architectures. The interaction of the electric field in the disordered resonator with the nonlinearity associated to the active material [73-76] gives rise to gain competition and nonlinear wave mixing of the optical modes [70,75], and ultimately determines the emission spectrum and the far-field profile.

As reported in Chapters 2, 3 and 4, the design of the photonic structures for THz QCLs based on dual periodicity, quasi-crystal or random patterns allows optimizing the optical power output, the operation frequencies, as well as the divergence and directionality of the laser beam. However, further flexibility in the operation of these devices can be achieved by controlling the mode dynamics and emission spectra with an external mechanism providing accurate tunability. Among disordered photonic lasers, tunable emission has been reported in random lasers operating in the visible frequency range, either by varying the resonator geometry, scatterers size and/or distribution, absorbing and boundary condition, tuning their spatial and temporal coherence [132] or, post-processing, magnetically [133], thermally [134], through stretching [135], or by electric field modulation [136]. Different approaches for the tuning of QCLs have been proposed, exploiting temperature variation [24], optical excitation from an external near-infrared laser [137], electric field tuning of master-slave interdigitated DFB cavities [138], gas condensation and dielectric deposition [130,140], microelectromechanical systems (MEMS) [141,142], engineering the Vernier resonances of an on-chip coupled cavity [143]. Unlike the previous examples which require a complex external or integrated tuning mechanism and often dramatically modify the laser output power, external-cavity tuning [144] offers a versatile and powerful approach to control the mode dynamics and therefore the emission spectrum with a much simpler experimental configuration. Tuning of laser frequencies with an external cavity

coupling has been successfully demonstrated both at infrared frequencies [145] and in the THz spectral region [146], showing a great potential for spectroscopic applications in biomedical, chemical and environmental analysis [147,148]. Recently, tuning of the operational frequency of one-dimensional DFB THz QCLs coupled to an external microcavity was demonstrated, by using a conventional second-order DFB grating [149] and a grating with a dual slit -tunability for a single-mode surface-emitting THz QCL. The latter approach benefits from the optimized extraction efficiency ensured by the photonic design, allowing a strong coupling with the external cavity via optical feedback. This results in a resonant energy exchange between the laser mode and the external microcavity, which produces a frequency shift of the mixed mode of the coupled system.[151]
Based on this, the tunability of the aperiodic THz QCL architectures, presented in this thesis, was experimentally studied, in order to provide a new route for the fine control of the multimode emission spectra of the devised quasi-crystal and random lasers, by realizing an external coupled-cavity configuration with a movable mirror placed over the top surface. Indeed, a continuous tuning of 20 GHz was reported with a multimode, surface-emitting Octonacci laser [41], while an even more complex spectral dynamics was unveiled with a random laser, with a multiple spectral lines continuously tuned over an 11 GHz-range of

A further investigation and manipulation of the spectral dynamics of aperiodic THz QCLs was carried on with a novel approach, i.e. by studying the interaction of the emitted THz radiation and a graphene film or ink. Indeed electro-optical materials can provide visible alterations on the emitted THz spectrum and/or the temporal waveform, for example for producing ultra-short laser pulses [152] or inducing ultrafast modulation [153] and reflection [154]. Intriguing approaches to achieve modulation and control on the mode dynamics of THz QCLs are possible exploiting the peculiar optical and electronic properties of novel two-dimensional materials, such as semiconducting transition metal dichalcogenides (tungsten diselenide) [155] and graphene [156]. The optical properties of graphene have been intensively studied in recent years [157,158], revealing a promising potential for a number of applications at THz frequencies [159,160]. The optoelectronic properties of graphene have been exploited to demonstrate graphene-based THz emitters

[160, 161] and detectors [35,163,164], as well as optical modulators which can be integrated with the THz source to modify the attenuation and transmission of radiation with large optical bandwidth, high modulation speed and small footprint [165]. Electro-optical graphene modulators exploit the fast carrier dynamics, energy dispersion and absorption properties of graphene, determining the inter-band and intra-band mechanisms used to control the optical absorption and transmission [37]. By changing the Fermi level in the material with by chemical means or by electrical tuning (for example, with a variable gate voltage) [166,167], THz radiation can be modulated, also reaching extraordinary transmission through specially devised patterned structures [168]. Moreover, graphene can also be combined with metal nanostructures to support surface plasmon modes, which are electrically tunable in the THz spectral range [169]. Indeed, this concept has been implemented to demonstrate an integrated graphene plasmon laser [170], exciting plasmons within an aperiodic lattice

with the round-trip gain, obtaining electrical control on the emission spectra.
THz saturable absorption can also be achieved in graphene [171,172] and carbon nanotubes [173] have also been investigated, since they have a promising potential to tailor THz radiation and induce mode-locking, with respect to the conventional semiconductor saturable absorbers (SAs) [174]. Even though the latter can be used from the visible to the mid-infrared spectral range [175,176], they are not well suited for operation in the 1-10 THz range, as they feature strong intrinsic free-carrier absorption losses,[177] limited bandwidth in reflection,[174], and inherently increase the intra-cavity losses when directly integrated in a semiconductor THz laser.[12] As a further limitation, THz QCLs feature population inversion relaxation times as short as a few ps [102,178], due to the intrinsic strong electron-phonon interaction in the QCL polar semiconductor gain material. [18,93]

In this context, graphene can take advantage of its ultrafast recovery time [179], broadband operation and low saturation fluency (i.e., the pulse energy density required to achieve saturation) [180], and ease of fabrication [181] and integration [171,172], which are crucial for the development of integrated SAs in THz QCLs. Graphene SAs can be used to achieve mode-locking operation, which has already been successfully achieved from the visible to the infrared frequencies [173,182-186]. Recently, graphene saturable absorption has been

investigated in the THz range both with multilayer graphene grown on the carbon-face of silicon carbide [38], which showed a 10% absorption modulation but has a challenging intra-cavity integration due to the material growth, and in graphene inks. Liquid phase exfoliation (LPE) of graphite indeed offers a more concrete perspective of easier intra-cavity embedding, since graphene from LPE can be combined in dry or liquid form with a host polymer matrix, and can also be used to produce printable inks [187,188] and SAs [189,190]. Graphene films can be obtained via inkjet printing, with the advantage of conforming to the target substrate features [191], as well as via vacuum filtration [186]. For films derived from graphene inks, this comes at the cost of a typically problematic removal of surfactants/polymers [192], and of solvents due to their high boiling point [193]. The presence of residual traces of solvents and surfactants can drastically hinder the graphene saturable absorption at THz frequencies [194], since such chemicals have absorption coefficients larger than a few cm-1 in this spectral region [195].
Therefore, surfactant-free graphene inks and films obtained via LPE of graphite or vacuum filtration, have the potential for an easier integration with THz QCLs and for higher absorption modulation. Indeed, water-based and surfactant-free ethanol-based graphene inks showed a much more intense absorption modulation (up to -cavity embedding, appealing for the mode-locking of THz QCLs or for the development of ultrafast optical components.

In this chapter, FTIR and Raman characterizations of a sample of multilayer graphene grown on Nickel and transferred onto a silicon substrate are reported, with a measurement of a saturable absorption effect showing a modulation -based graphene ink deposited on an intrinsic silicon substrate were used as reflectors for the surface-emitted radiation of a random laser, showing a higher selective suppression of spectral peaks or the appearance of multiple modes with regular

5.2 Multimode emission tuning with external cavity

5.2.1 External cavity experiment

One intriguing possibility to control and investigate the mode dynamics in a THz QCL exploits the feedback effect of an external cavity, whose geometry

can be finely tuned. In such a system, tunable emission is obtained by changing the cavity size d with a movable optical element, such as a reflecting mirror, so that its resonant frequency varies with the law:

$$\nu_{cav} = m\frac{c}{2d} \tag{40}$$

where c is the light speed in vacuum and m is the order of the bare cavity resonance. The external cavity is brought in resonance with an emission line of $_i$ when the matching condition is reached:

$$d = \frac{1}{2}\lambda_i,\ \lambda_i,\ \frac{3}{2}\lambda_i, 2\lambda_i \ldots \tag{41}$$

In this condition, the resulting strong coupling gives rise to a resonant exchange of energy between the QCL and the external cavity, inducing a frequency shift and intensity modulation of the relative spectral peak. Typically this effect depends on the feedback intensity and the coupling efficiency between the cavity and the single-mode laser [150,151], but the dynamics is even more complex when using an intrinsically multimode THz QCLs, such as the reported Octonacci quasi-crystal or random laser. Indeed, coupled mode theory indicates that each mode of the aperiodic THz QCL exchanges energy via a cross-coupling interaction with the resonant modes of the external cavity. Moreover, the different modes in the random resonator may interact with each other as a result of mirror-induced self-coupling, especially if their frequencies are close [151]. This latter mechanism, expected in RLs, is instead absent in

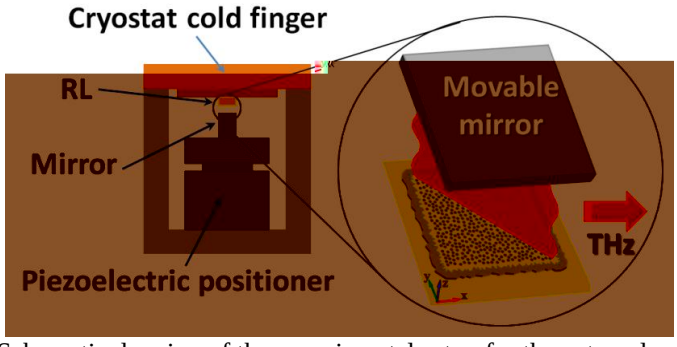

Figure 5.1: Schematic drawing of the experimental setup for the external cavity tuning, consisting of a cold finger hosting the laser chip (for example, a random resonator) and an external mirror mounted on a piezoelectric positioner. Light is guided by the external cavity formed by the laser surface and the parallel gold mirror, in the direction orthogonal to the RL surface, towards the FTIR.

single-mode DFB QCLs [150,151]. In spite of these multiple interactions, the tuning range for a single-mode can be roughly estimated as twice as the photon loss rate, computed neglecting the complex self-coupling dynamics. The surface losses are retrieved computing the power flow through a transparent boundary S of the air domain above the resonator (i.e., integrating the Poynting vector on S), and dividing by the electromagnetic energy stored in the device volume A.
For resonating electric and magnetic fields (**E**, **H**) at the surface S enclosing the

$_{rad}$ is the inverse of the radiative photon lifetime $_{rad}$:

$$\gamma_{rad}(\nu) = \frac{1}{\tau_{rad}(\nu)} = \frac{2}{\varepsilon_0} \frac{\int_S (\mathbf{E} \times \mathbf{H}^*) \cdot \hat{n}\, dS}{\int_A (\varepsilon_r |E|^2 + Z_0^2 |H|^2)\, dV_A} \qquad (42)$$

$_r$ is the relative dielectric constant of the material and Z_0 is the free-space impedance.
The setup employed in our experiments exploits a horizontal cryostat finger for placing the surface-emitting THz QCL (such as an Octonacci quasi-crystal or a random laser) and ensuring the needed cooling for the device, as shown in figure 5.1. A piezoelectric driver with a narrow copper holder on top hosts a piece of intrinsic GaAs, coated with 150 nm of gold acting as a mirror and placed parallel to the laser top surface, to form an external cavity. The piezoelectric driver is controlled with 20 V saw-tooth pulses, producing an

accurately positioned at a distance d from the laser top surface, producing the desired external cavity modulation. Light is then laterally collected via a parabolic mirror and conveyed to the FTIR for the acquisition of the emission spectra.

5.2.2 Frequency tuning of an Octonacci laser

As reported in chapter 3, the devised Octonacci resonators provide multimode emission when the slit aperture is narrow (L = 1.9 μm), so they can be exploited in a coupled-cavity experiment to fine-tune the laser spectral lines and explore the resulting spectral dynamics. An Octonacci resonator with ridge width W = 160 μm and slit aperture L = 1.9 μm was coupled to an external gold-coated mirror, whose position was varied with a piezo driver to scan a distance range d = 80 - -direction (where

5.2a shows the acquired multimode FTIR spectrum of the Octonacci laser, driven at a temperature of 12 K and 1%-duty-cycle. The different spectral lines identified as follows: mode A at 3.243 THz, mode B at 3.235 THz, mode C at 3.386 THz, mode D at 3.396 THz and mode E at 3.440 THz. Figure 5.2b shows the spectral dynamics and mode-hopping of the peaks A and B, while figure 5.2c highlights the evolution of lines C, D, E for mirror distances comprised

relative peak intensities as well as of the frequency position are visible.

reported in the contour plot of the experimental spectra in figure 5.3.a, which underlines that the lower-frequency modes A and B are more affected by the

frequencies of modes C, D, E are much less perturbed by the mirror movement. These experimental results can be compared with a three-dimensional simulation of the quality factors of the eigenmodes of the system made up by the device and the parallel mirror at a distance d from the top metal surface. Figure 5.3b illustrates a contour plot of the quality factor of the simulated resonating modes in the case of the same device (i.e., W = 160 μm, L = 1.9 μm) for mirror distances d comprised between 10 μm and 150 μm. The overall three-dimensional quality factor is strongly enhanced when the mirror is positioned so that the bare external cavity frequency is resonant with a laser eigenmode frequency. This indicates the resonant energy exchange between the two systems, showing good agreement with the coupling effects experimentally retrieved for the spectral peaks at 3.25 THz and 3.39 THz.

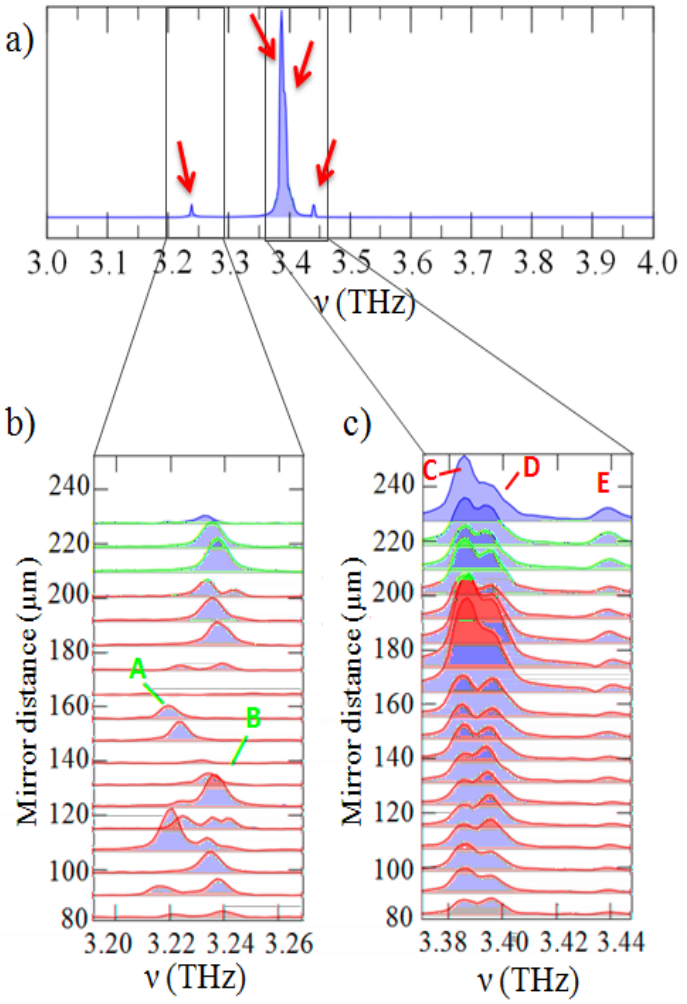

Figure 5.2: a) FTIR emission spectrum of a multimode Octonacci laser with geometrical parameters W = 160 μm and L = 1.9 μm, operated at a temperature of 12 K and 1%-duty-cycle. The spectral dynamics of the emission for modes A and B (b) and for modes C, D and E (c) is reported, for a mirror position swept between 80 μm and 230 μm. Each spectrum is acquired with a mirror shift of 18 μm, as indicated by the offset of its baseline.

5.2. External-cavity control of a random laser in pulsed regime

Following the same experimental scheme described above, an external-cavity experiment was performed to investigate the tunability of the multimode, two-dimensional random lasers, both in pulsed and CW regime.

Figure 5.4a shows an example of FTIR emission spectra from a type-B RL, ^{2} and filling fraction 13%, while figures 5.4b and 5.4c report the evolution of the emission peaks acquired at

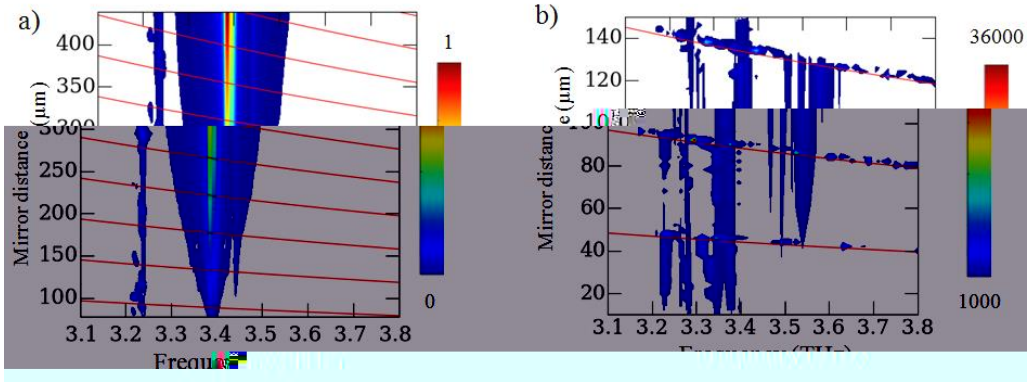

Figure 5.3: a) Normalized contour plot of the spectra of the same laser, for a mirror position d sweep between 80 µm and 430 µm, with a strong frequency dynamics around 3.25 THz (modes

quality factors for mirror distances between 10 µm and 150 µm. In both plots, red lines are the resonant frequencies of the external cavity at different d.

frequency tuning within the resolution limit of the FTIR, indicating that their respective coupling strength with the cavity is low. Instead, the less intense peaks centered at 3.21 THz (mode A), and the three peaks around 3.38 THz (modes B, C, D) undergo a much stronger intensity and frequency modulation at different mirror positions. When the mirror distance approaches a resonant

free-space wavelength of the spectral line), a maximum -10 dB intensity reduction and a maximum continuous frequency s
the measured spectral line. Instead, mode-hopping among the emission peaks B,

central frequency of 3.38 THz. By moving the mirror, a number of peaks disappear periodically, whilst other peaks show an intensity increase, in a complex interplay that depends on the matching condition for the cavity resonance as well as on the competition between modes localized inside the resonator.

This complex mode dynamics can be investigated with a statistical analysis of

correlation C_{ij} $_{i}$ $_{j}$ for all mirror positions (i.e., piezo-driver steps) according to the definition:

$$C_{ij} = \frac{\sum_{steps} [\Delta I(\nu_i) \cdot \Delta I(\nu_j)]}{\sqrt{\sum_{steps} [\Delta I(\nu_i)]^2} \sqrt{\sum_{steps} [\Delta I(\nu_j)]^2}} \tag{43}$$

When the correlation coefficient between two modes is positive, then their intensities show a simultaneous increase/decrease as the mirror moves. A negative correlation coefficient instead indicates that the peak intensities are alternatively increasing or decreasing, so they are actually competing against each other. The B and C modes consistently are negatively correlated with a coefficient C_{BC} -0.34, while C and D have a positive correlation (C_{CD} -0.47 with the most intense peak at 3.26 THz.

For larger frequency spacing between the peaks, the absolute values of the intensity correlations are negligible (e.g. for A and C, C_{AC} -0.08), indicating that the associated intensity fluctuations are not cross-related.

The frequency tunability (11 GHz) of the spectral peak at 3.21 THz is in good agreement with the results of the fully 3D FEM simulation of the structure with transparent boundaries, providing the photon exchange rates. Indeed the frequency-tuning excursion of a single spectral peak with an external coupled cavity can be estimated as twice the photon exchange rates of the optical mode. The numerical results for the computed eigenmodes indicate a photon exchange rate of the resonating mode at 3.21 THz of 5 GHz, with an associated tuning excursion of 10 GHz in presence of a movable mirror. Conversely, the other spectral peaks at 3.11 THz, 3.24 THz, 3.26 THz, 3.28 THz are expected to have an associated photon exchange rates of 2 GHz, meaning that a maximum tuning excursion (4 GHz), which is close to the resolution limits of the FTIR (3.7 GHz), is expected in presence of a movable mirror. The frequency-tunable modes also show a significant intensity modulation IM, defined as follows:

$$IM = 10 \log(I_{min}/I_{max}) \tag{44}$$

For example, spectral lines B, C, D that show a 20 GHz mode-hopping tuning range have an intensity modulation of maximum of -28 dB. In contrast, the two most intense emission peaks at 3.11 THz and 3.26 THz only show a -6 dB intensity modulation, which is consistent with the absence of frequency tuning (at a level that can be measured with the available FTIR resolution).

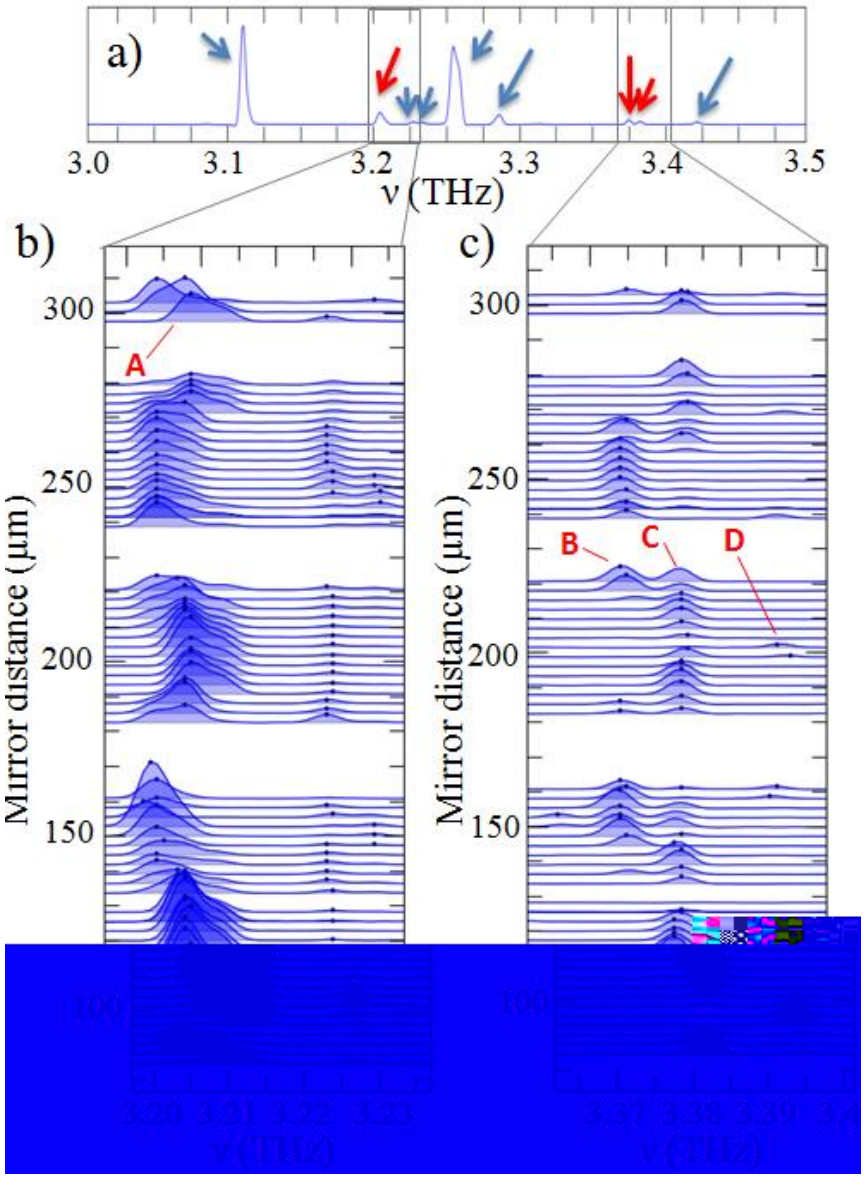

Figure 5.4: a-c) FTIR emission spectra of a type-
mm^2, filling fraction 13%), at a mirror distance d
with at J = 0.52 A/cm^2 at a heat sink temperature of 15K and a resolution of 0.125 cm^{-1}. b)
-
around 3.38 THz. All spectra are offset so that their baseline corresponds to the mirror distance at which they were acquired. All spectra in the insets have been normalized; the blue dot indicates the position of spectral peak.

Figure 5.5: a) Histogram showing the maximum continuous spectral tuning for the most intense modes of figure 5.4. The spectral lines around 3.4 THz are those involved in the mode hopping dynamics with a 20 GHz discontinuous shift, though t

which have the most intense spectral lines mostly unaltered by the mirror position due to a reduced energy exchange with the external cavity.

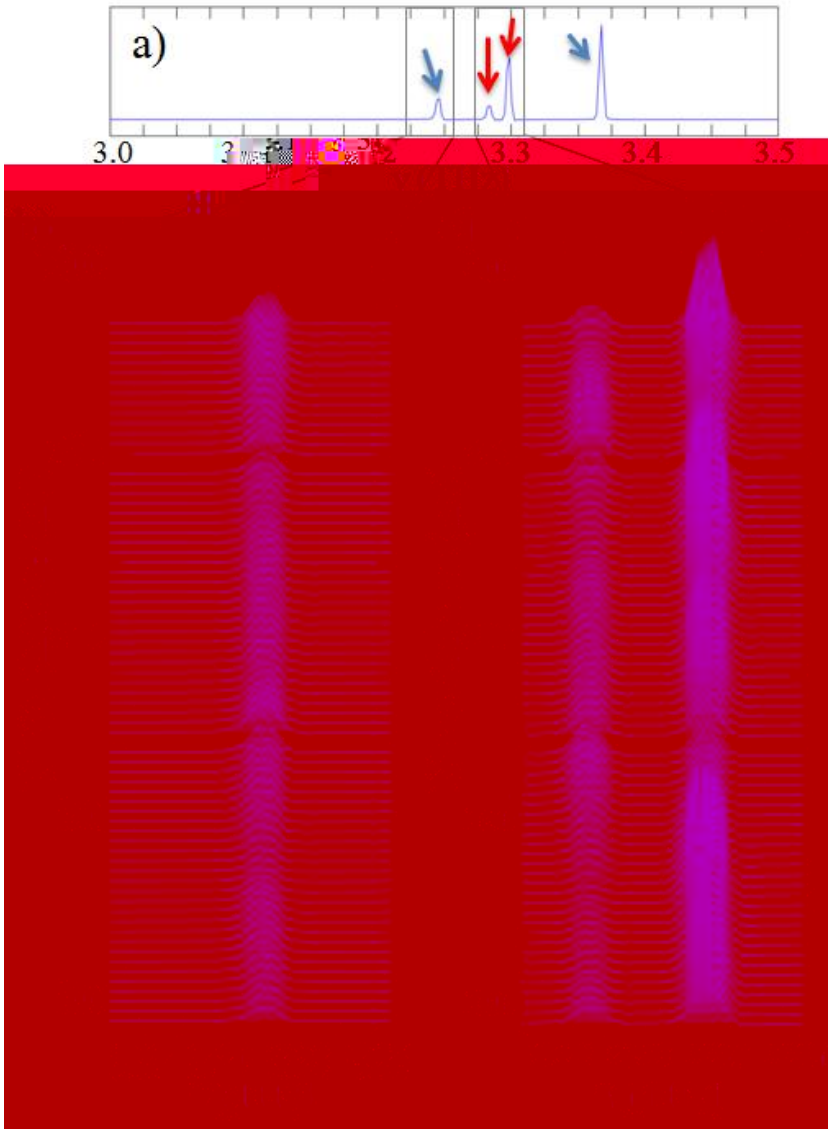

Figure 5.6: a) CW emission spectra of the type-
mm^2, filling fraction 25%, measured at 15 K whilst varying the mirror distance d between 90

c) evolution of the peak at 3.29 THz for different mirror positions. The red arrows identify the peaks studied in the panel c.

5.3 Optical THz mode control with graphene

5.3.1 Graphene and 2D materials for THz QCL engineering

Two-dimensional nano-materials and related heterostructures have recently been investigated as intriguing material systems for the development of novel photonic, electronic, and plasmonic devices.

A number of recent technological applications, from optical communications to photodetectors, from saturable absorbers to optical modulators, employ the unique band-structure and electron transport characteristics of 2D materials such as graphene, black phosphorus and transition-metal dichalcogenides (TMDCs). In particular, the electronic and optical properties of graphene can be easily engineered by accurate layer thickness control, exploiting the high carrier mobility, gapless spectrum, and the possibility to deeply modify its dielectric constant through electrical gating or chemical doping, [172] making it a versatile systems for the development of new-generation devices operating in the THz frequency range [196,197].

Graphene can be also exploited to alter the optical and electronic properties of existing THz emitters; the laser spectral properties can be altered by modulating the laser gain via graphene plasmons, by means of electrical gating[198], or, alternatively to induce intra-cavity effects on the mode dynamics which cannot be self-activated.

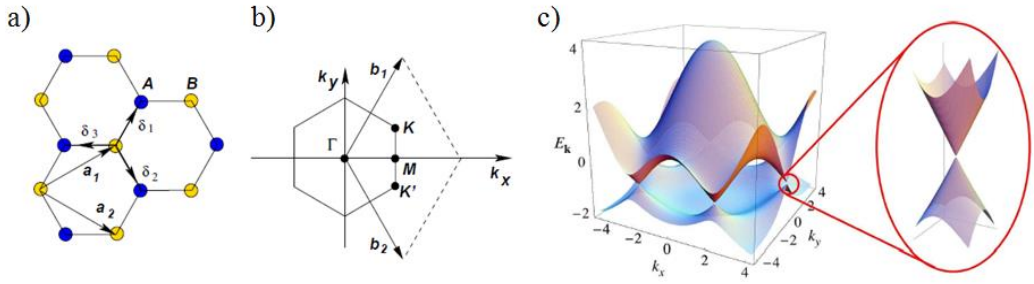

Figure 5.7: a) Two-dimensional lattice structure of graphene, highlighting the fundamental unit vectors $\mathbf{a}_1$ and $\mathbf{a}_2$ and the nearest neighbor vectors $_1$, $_2$ and $_3$. b) Brillouin zone of graphene in the reciprocal space, indicating the K and K' points where the Dirac energy cones converge, as shown in c). From [199].

Graphene possesses a hexagonal lattice of carbon atoms is typically used in single-layer or multi-layer configurations,[199] which have different properties arising from the inter-layer interactions and screening effects. The single-layer graphene crystal is illustrated in figure 5.7a, forming a triangular lattice with a basis of two atoms per cell with fundamental vectors:

$$\mathbf{a}_1 = \frac{a}{2}(3, \sqrt{3}) \qquad \mathbf{a}_2 = \frac{a}{2}(3, -\sqrt{3}) \tag{45}$$

-site distance. Figure 5.7b shows the representation of graphene in the reciprocal space Brillouin zone, with the two **K** and **K'** points in momentum space given by

$$\mathbf{K} = \frac{2\pi}{3a}\left(1, \frac{1}{\sqrt{3}}\right) \qquad \mathbf{K}' = \frac{2\pi}{3a}\left(1, -\frac{1}{\sqrt{3}}\right) \tag{45}$$

The electronic band structure of single-layer graphene can be computed in a tight binding approximation, considering the hopping of electrons to the nearest and next-nearest lattice sites (see figure 5.7c). Near the main **K** reciprocal lattice vector (as well as near **K'**), the wavevector can be written as **k** = **K** + **q** with |**q**| << |**K**|, the dispersion is approximately linear in the two-dimensional momentum **q** measured with respect to **K**:

$$E_{\pm}(\mathbf{q}) \approx \pm v_F|\mathbf{q}| \tag{46}$$

where v_F ^{6} m/s is the Fermi velocity. Due to the linearity of the energy, the effective mass for the electron near **K** and **K'** is zero, very differently from conventional crystalline materials. Therefore, the electrons in graphene are also named "massless Dirac fermions" and their energy dispersion pinned at **K** and **K'** is referred to as "Dirac cone". The positive cone and the negative one touch at the zero-energy level for **q** = 0. Therefore, single-layer is a gap-less material, whose available states are occupied according to the Fermi-Dirac thermal distribution $f_0(E)$ at an equilibrium temperature T_{el}. The chemical potential μ for pristine, undoped graphene lies at the zero-energy level, but it can be tuned to lie in one of the two Dirac bands by adding impurities and dopants. The relationship between the doping level and the resulting chemical potential is defined as follows [200]:

$$n_0 = \frac{2}{\pi\hbar^2 v_F^2}\int_0^\infty d\varepsilon\, \varepsilon[f_0(\varepsilon) - f_0(\varepsilon + 2\mu)] \tag{47}$$

The chemical potential in a sample is influenced by the graphene growth process and substrate [199], and can be further controlled by chemical doping, or dynamically varied by applying a bias via a field effect transistor (FET) lithographically defined on the sample [201].

5.3.2 Conductivity model for graphene optical properties

The optical properties of graphene can be retrieved by investigating the intra-band and inter-band material conductivity. Intra-band processes are associated to the electron-

described with a Drude model response. Inter-band contributions are instead related to direct promotion of electrons from the lower Dirac cone to the upper one, or to the decay in the opposite direction.[202] Inter-band transitions can be achieved only when the optical photon has an energy $\hbar$

principle, preventing a further electron occupation of the energy levels up to μ. For lower photon energies, the intra-band contributions are dominant. At an electron temperature T_{el} and around the Dirac points, the sheet conductivity of a layer of graphene can be written as: [203]

$$\sigma(\omega) = \frac{2e^2 k_B T_{el}}{\pi\hbar^2}\frac{i}{\omega + i/\tau}\ln[2\cosh(\mu/2k_B T_{el})] + \\ + \frac{e^2}{4\hbar}\left[H(\omega/2) + \frac{4i\omega}{\pi}\int_0^\infty d\varepsilon \frac{H(\varepsilon) - H(\omega/2)}{\omega^2 - 4\varepsilon^2}\right] \tag{48}$$

where k_B is the Boltzmann constant and H is the auxiliary function:

$$H(\varepsilon) = \frac{\sinh(\hbar\varepsilon/k_B T_{el})}{\cosh(\hbar\varepsilon/k_B T_{el}) + \cosh(\mu/k_B T_{el})} \tag{49}$$

accounts for the intra-band effects, which are stronger at THz and mid-IR frequencies, while the second term describes the inter-band

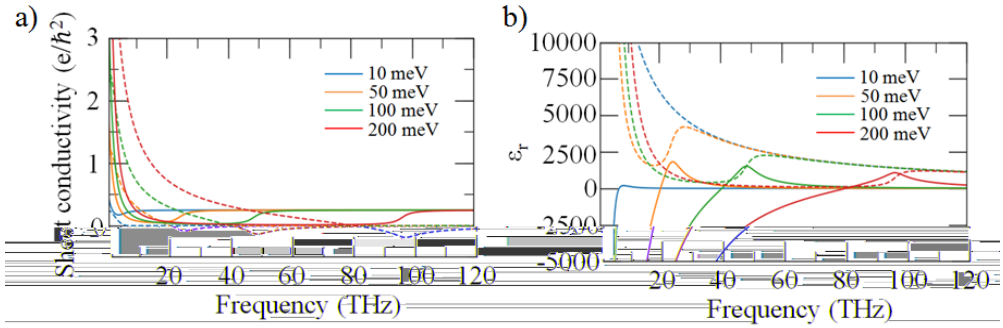

Figure 5.8: a) Plot of the real part (continuous line) and imaginary part (dashed line) of the sheet conductivity of single-layer graphene, for different values of the chemical potential. Plot of the real and imaginary parts (continuous and dashed lines, respectively) of the relative dielectric function for different values of the chemical potential. The results are obtained with a custom-

contributions, mostly deriving from the interaction with near-IR or visible photons. Figure 5.8a shows the graphene sheet conductivity for electron

custom code in the range between 1 THz and 120 THz for different values of the chemical potential. A three-dimensional conductivity can be obtained for multilayer graphen
Å, in the limit of low inter-layer interaction, with the formula: [200]

(50)

This results in an effective complex dielectric function for N layers:

(51)

from which the associated real and imaginary part of the refractive index can be retrieved as:

(52)

Figure 5.8b shows the real and imaginary parts of the dielectric function in the case of 50 weakly-interacting graphene layers with
different μ. However, more complex numerical models can be implemented to treat the multilayer case, accurately accounting for the inter-layer bonds and many-body effects.

5.3.3 Saturable absorption

In presence of high-intensity electromagnetic fields, the interaction between graphene and photons gives rise to non-linear effects sucg3Wr̃498.96 7onistfeeu217(ibl)-5

graphene transmission is strongly perturbed by non-linear effects associated to the non-equilibrium populations of electron and holes produced in the upper and lower Dirac cones, respectively. Considering the simple case of undoped

from the lower band to the upper one (see figure 5.9a), the populations of carriers in the upper and lower bands are increased, so that further absorption of photons with the same energy is suppressed due to the Pauli blocking. This phenomenon is particularly relevant for intrinsic graphene, illuminated by Terahertz radiation, inducing low-energy transitions near the Dirac point, where the available density of state D(ħ
becomes less effective, resulting in enhanced transmission. With a characteristic
$_1$ of a few picoseconds, the non-equilibrium electron and hole populations thermalize via elastic carrier-carrier scattering, as shown in figure 5.9b. As reported in [204] for an initially fully occupied lower Dirac cone and empty upper Dirac cone, an incident light pulse with intensity evolving in time as $I_{in}(t) = I_0 \exp(-t^2 \ ^2)$, induces an additional positive contribution to the graphene. This term describes a temporal evolution of the graphene transmission:

$$T(t) = 1 - \pi\alpha + \frac{\pi^2\alpha^2}{D(\hbar\omega/2)\hbar\omega/2} I_0 G(t) \tag{54}$$

where G(t) is positive time integral (with positive value) describing the interaction of the material with the light pulse.[204] Therefore, a transmission bleaching is obtained in correspondence with the high-intensity part of the light pulse. A similar discussion holds when considering the spatial distribution of the incident radiation, so that the regions with strongest beam intensity induce an increase of transmission, as reported in figure 5.9b.

The transmitted intensity I_t is a function of the linear, non-saturable absorption
$_{NS}$ $_S$, whose contribution is modulated by the incident power I_{in}. In a simple two-level saturable absorption picture, the transmission can be written as:

$$T(I_{in}) = \frac{I_t}{I_{in}} = \left(1 - \alpha_{NS} - \frac{\alpha_S}{1 + I_{in}/I_S}\right) \tag{55}$$

where I_S is the saturation intensity, i.e. the impinging intensity at which the saturable contribution is reduced by 50%.

Successful demonstrations of saturable absorption have been achieved in the last years using different types of graphene samples illuminated by THz QCLs

[38,39]. As illustrated in Chapter 5, this thesis work also encompasses the use of multilayer graphene as THz saturable absorber and modulator to manipulate the emission spectra of aperiodic resonators.

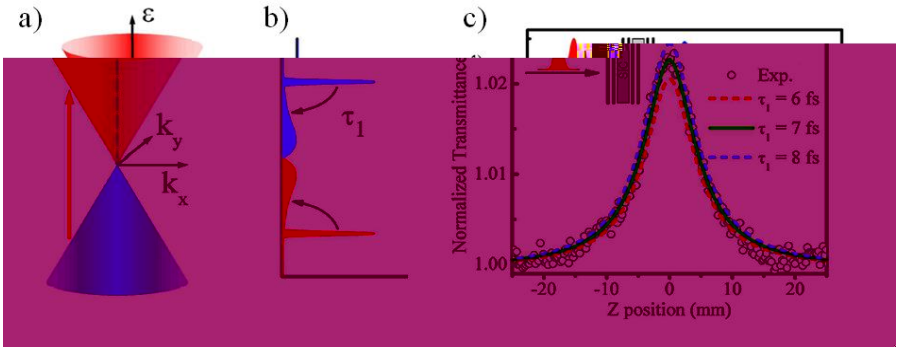

Figure 5.9: a) Depicted optical transition from the valence band (blue) to the conduction band (red), with momentum conservation. The momentum conserved photon absorption process in graphene b) Instantaneous non-equilibrium distributions of electrons (blue) and holes (red) are produced by the photon absorption, which subsequently thermalize towards the Fermi-Dirac distributions via ultrafast intraband carrier-carrier and carrier-optical phonon scattering. c) Typical non-linear transmittance of graphene layers at different Z position (circle dots) compared with simulations exploiting different $_1$. From [64]

5.3.4 Raman and FTIR characterization of the graphene samples

Raman spectroscopy of graphene samples allows monitoring the quality of the deposited material, giving quantitative information on the number of layers, or the presence of defects and disorder due to the specific growth and deposition methods [206-209]. Indeed, the G peak is associated to the high-frequency phonon E_{2g} while the D peak is related to the transverse optical phonons at the K point at the edge of the Brillouin zone, requiring a double resonance process [210] which is activated only by the presence of defects [206,208,209]. Similarly, the D' peak is connected to the transverse optical phonons around the K' point of the graphene band structure. Further peaks called 2D and 2D' are second-order resonances of the D and D' peaks, respectively. Since they are generated by the momentum conservation for two counter-propagating phonons, the 2D and 2D' peaks are always present independently of the presence of defects in the crystal structure [207].

A multilayer graphene sample was grown on a Nickel substrate at the Graphene Lab in Cambridge, using the chemical vapour deposition (CVD) method [211].

This technique allows the production of multilayer graphene with a typical

layers. The material was subsequently transferred onto a target intrinsic silicon substrate, with a thickness of 350 µm and both sides covered by 300nm-thick SiO_2 layer. Figure 5.10 reports a Raman spectrum measured illuminating the CVD-grown graphene sample using a Renishaw InVia instrument, operated with an excitation laser with a wavelength of 514 nm and a power kept below 1 mW to prevent any thermal damage on the sample, taking 2 scans with a 100x ocular and an acquisition time of 60 s each. The Raman spectrum features an intense G peak at 1584 cm^{-1} and a broad 2D peak with maximum at 2730 cm^{-1}.

$^{-1}$,

indicating that the material is strongly multilayer.

A further preliminary optical characterization of the sample was performed via FTIR spectroscopy, investigating the linear absorption in the THz range. Spectra were acquired with deuterated triglycine sulfate (DTGS)-polyethylene detector, with a spectral resolution of 16 cm^{-1} and averaging over 16 scans. The FTIR transmission spectrum of the CVD-grown graphene is reported in figure 5.11, after normalizing to the SiO_2/Si transmittance, showing a relatively flat trend in the frequency range comprised between 2.5 THz and 9.0 THz. The measurements for the normalized transmission of the water-based graphene ink are available in reference, [39], as well as the associated Raman spectrum.

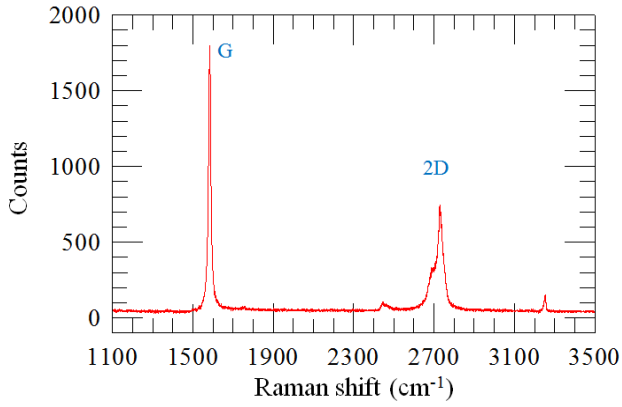

Figure 5.10: Raman spectrum of the sample with the graphene grown on Nickel with CVD, measured with a 100 s acquisition time in extended mode between 1100 cm^{-1} and 2900 cm^{-1}, with an excitation laser wavelength of 532 nm. The plot reveals the G peak (1584 cm^{-1}) and the

$^{-1}$.

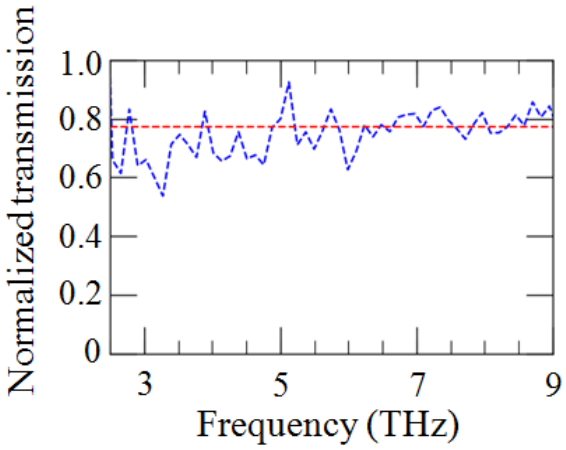

Figure 5.11: Transmission FTIR spectrum (blue) of the sample with graphene grown via CVD and , normalized to the Si/SiO_2 substrate transmission. The red dashed line represents the average transmission value in the shown spectral range. Data were acquired in vacuum conditions (2 hPa), with 16 scans at a resolution of 16 cm^{-1}.

5.3.5 Saturable absorption experiment

In order to study the non-linear absorption of the graphene sample grown via CVD on Nickel and transferred onto an intrinsic silicon substrate, an open aperture z-scan transmission experiment [38,39] was performed with the setup reported in figure 5.12, using a single-plasmon pump QCL with an emission frequency of 2.7 THz. The device was operated in pulsed regime with a pulse width of 1000 ns and repetition rate of 40 kHz, i.e. a duty cycle of 4%, at a heat sink temperature of 37 K. This laser pulses were further modulated by a 33 Hz-square wave signal with a 50% duty cycle, to provide the synchronous reference for the detector and the lock-in system. The THz radiation emitted by the QCL was collected by two convergent lenses (L1 and L2), with same focal length f = 3 cm, and conveyed onto the sample with perpendicular incidence. The graphene sample was hosted on a custom-made holder and its position was swept with a micrometric stage along the optical axis (z direction) between L2 and the pyroelectric detector, kept in a fixed position. The bare SiO_2/Si substrate transmittance was also measured, so that the transmittance data could be normalized to retrieve the multilayer graphene properties. By moving the sample along the z direction, the beam spot size changes, reaching a minimum at the focal point, where the power intensity on the sample is maximum.

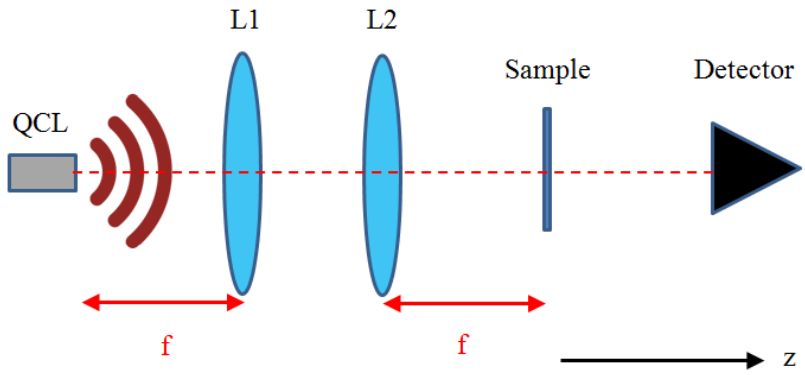

Figure 5.12: Optical setup for the open aperture z-scan measurement to investigate the saturable absorption effect in the graphene sample. The THz light emitted by the QCL is focused by the convergent lenses L1 and L2 onto the graphene sample. The transmitted signal is then collected by the pyroelectric detector. The sample is moved along the optical axis (dashed red line).

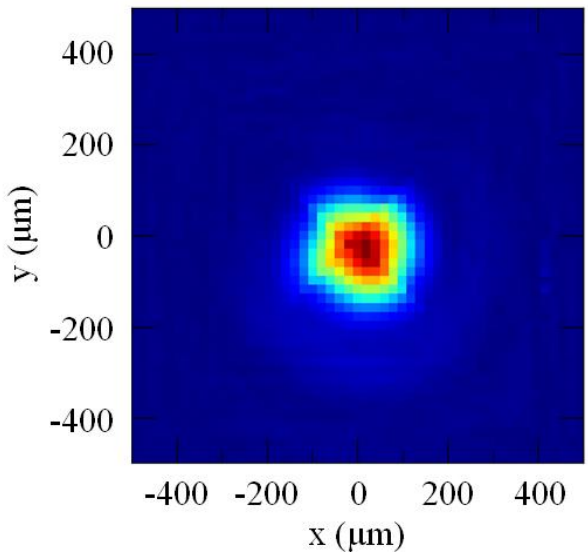

Figure 5.13: Intensity profile of the THz QCL beam used in the saturable absorption experiment, measured in the x-y focal plane orthogonal to the beam propagation axis with a FET graphene detector moved a step size of 20 μm.

The beam spot size was estimated by directly measuring the beam profile at the focal point, with a high-resolution scan of the x-y plane orthogonal to the optical axis z with a graphene-based FET thermoelectric detector with a step

size of 20 μm, as shown in fig. 5.13. A two-dimensional fitting procedure was implemented to evaluate the beam radial waist w_0 considering a gaussian beam profile, giving w_0 = (108.6 ± 0.1) μm. For a gaussian beam, another important parameter is the Rayleigh length z_R, that is the distance along the beam propagation direction, from the waist to the point where the cross-section area is doubled. The Rayleigh length is related to the beam size of a laser emitting at a

$$z_R = \frac{\pi w_0^2}{\lambda} \tag{56}$$

and in this case the value is z_R

Gaussian spatial profile in the x-y plane, the intensity of the beam along the z axis can be expressed as

$$I(z) = \frac{I_0}{1 + (z/z_R)^2} \tag{57}$$

considering z = 0 μm the position where the beam is focused at the minimum beam waist. From the measured power and the beam waist, the pump laser provided an average value I_0 ^{2} at the focal point. The total absorption coefficient depends on the pump intensity of the THz QCL with the formula [38,39]:

$$\alpha(I) = \alpha_{NS} + \frac{\alpha_S}{1 + (I(z)/I_S)} \tag{58}$$

which accounts for the non- $_{NS}$ and the $_S$. The parameter I_S is the saturation intensity, at which the saturable absorption contribution is reduced by a factor 1/2. When the pump laser is off, the absorption coefficient only accounts for the linear optical effects:

$$\alpha_0 = \alpha(I = 0) = \alpha_{NS} + \alpha_S \tag{59}$$

The overall normalized transmittance in a saturable absorption z-scan experiment can be written as [212]:

$$T(z) = \left[1 - \alpha_0 + \alpha_S - \frac{\alpha_S\left(1 + (z^2/z_R^2)\right)}{1 + (z^2/z_R^2) + (I_0/I_S)}\right] \frac{1}{1 - \alpha_0} \tag{60}$$

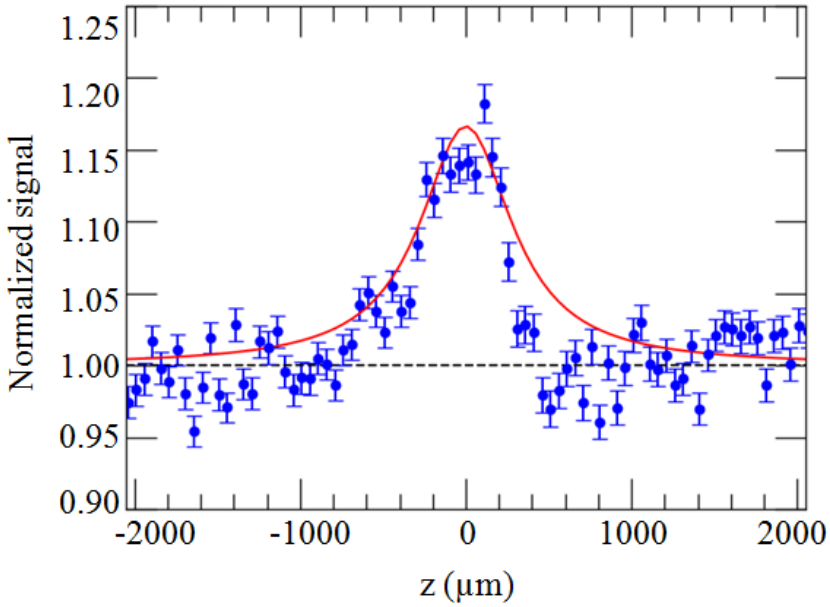

Figure 5.14: Plot of the z-scan normalized transmittance signal (blue dots) of the multilayer graphene sample grown on Nickel via CVD and transferred onto a SiO_2/Si carrier substrate. s of the Si/SiO2 substrate transmittance. The red line is the fit with equation 60 for the normalized transmittance T(z) as a function of the sample position along the optical axis of the setup.

Figure 5.14 shows the measured z-scan transmittance, normalized to the one of the SiO_2/Si substrate. The plot indicates an increase in the transmission around

the sample. This absorption bleaching increases the graphene sample

Si/SiO2 substrate shows no significant variation of the transmission along the z-direction, confirming that the saturation effect is associated to the multilayer graphene film. The experimental normalized transmittance was fitted with the above- $_S = 0.39 \pm$ 0.07 and a non- $_{NS} = 0.12 \pm 0.05$. The saturation intensity, instead, is estimated to be $I_S = (5.8 \pm 0.9)$ W/cm^2.

As reported in reference [39],the other water-based graphene sample showed an even stronger signature of saturable absorption effects, featuring a saturable $_S = 0.68 \pm 0.1$ and a non- $_{NS} = 0.17 \pm 0.02$, with a saturation intensity $I_S = (6.7 \pm 1)$ W/cm^2. In this case, the transmittance modulation reached a maximum increase of about +80%.

5.3.6 External modulation of a THz random laser with graphene

To further investigate and exploit the optical properties of the CVD-grown multilayer graphene and the water-based graphene ink samples, the graphene samples were coupled to the surface-emitting random lasers, employing an experimental setup, similar to the one shown in figure 5.1. A two-dimensional random THz QCL with filling fraction r/a = 26% and area of 0.70 mm^2 was mounted on a cryostat head, while a single graphene sample placed on a copper holder tightly fixed on top of the piezoelectric positioner, as shown in figure 5.15. The piezo-driver was u

200 μm from the laser top metal surface, ensuring the sample and the laser surface were parallel to each other. The above configuration also ensure that the laser beam impinge over a surface fully covered by the multilayer graphene ink.

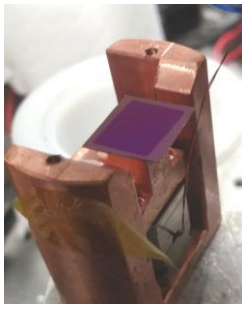

Figure 5.15: Mounting of the SiO_2/Si substrate coated with multilayer graphene (grown on Nickel via CVD), placed on top of a copper holder tightly screwed to the piezoelectric positioner. The whole mount was then connected to the cryostat head hosting the two-dimensional random laser.

The random THz QCL was driven in pulsed regime with a pulse width of 200 ns and a repetition rate of 75 kHz (i.e., a 1.5%-duty cycle) at a temperature of 10 K. The emitted radiation was coupled to the graphene sample (whose

could be collected by the FTIR optics and conveyed to its internal DTGS detector for the acquisition of the interferograms. The spectra were averaged over 32 scans, with the maximum available resolution of 0.075 cm^{-1} and in vacuum. Figure 5.16a reports the spectrum of the laser driven at 470 A/cm^2, acquired in presence of the SiO_2/Si substrate coated with the multilayer graphene (MLG) grown on Nickel via CVD (blue line), compared to the spectrum of the bare random laser with no other material in figure 5.16b (red line).

The spectral dynamics of the laser coupled to the multilayer graphene was investigated by varying the driving current and the applied bias, in between the threshold and the power-roll off condition associated to the negative differential resistance at high fields. As shown in figure 5.16c for an injected current density of 470 A/cm^2, a cluster of 4 spectral peaks between 3.03 THz and 3.08

GHz, while only three peaks are present with the bare substrate. Moreover, another spectral line is ac
THz, which is instead missing when the same experiment is repeated coupling the random laser with the bare silicon substrate, which is conversely keeping the dynamics of the laser modes spectrally unperturbed. This behavior is persistently reported also driving the laser at higher current densities, such as 510 A/cm^2 (fig. 5.16d) and 540 A/cm^2 (fig. 5.16e). In the spectral range between 3.09 THz and 3.30 THz, the laser radiation coupled to the graphene

45 GHz, each made of two unresolved peaks, as shown in figure 5.16f for a current density of 470 A/cm^2. Interestingly, the presence of graphene activates an additional emissio
spectrum of the bare laser, as shown also in figures 5.16g and 5.16h.

The experimental scheme described above was also used to couple the same random laser with the water-based graphene ink sample. The FTIR emission spectrum of the laser operated with a current density of 470 A/cm^2 in presence of the graphene ink is shown in figure 5.17a, while figure 5.17b reports the spectrum of the bare laser in the same driving conditions. In this case, the spectral range between 3.05 THz and 3.09 THz features a cluster of three modes with a regular spacing of 11 GHz (see fig. 5.17c), which is compatible with the behavior in presence of the CVD graphene which actually enhanced the emission of a further fourth spectral line at 3.03 THz. These effects indicate that the presence of graphene redistributes the spectral power density among the different peaks with respect to the emission of the bare laser, as consistently reported even for higher injected current densities of 510 A/cm^2 (figure 5.17d) and 540 A/cm^2 (figures 5.17e). In the frequency region between 3.09 THz and 3.30 THz, the spectra at different operation conditions indicate the presence of
by at
least two unresolved peaks. Similarly to the effect of MLG, an extra cluster

injection conditions (figures 5.17f, 5.17g, 5.17h). Conversely, minor modes having a different frequency separation with respect to the main modes are selectively suppressed in presence of the graphene ink sample. The reported FTIR spectra of the THz random laser coupled to the external graphene samples

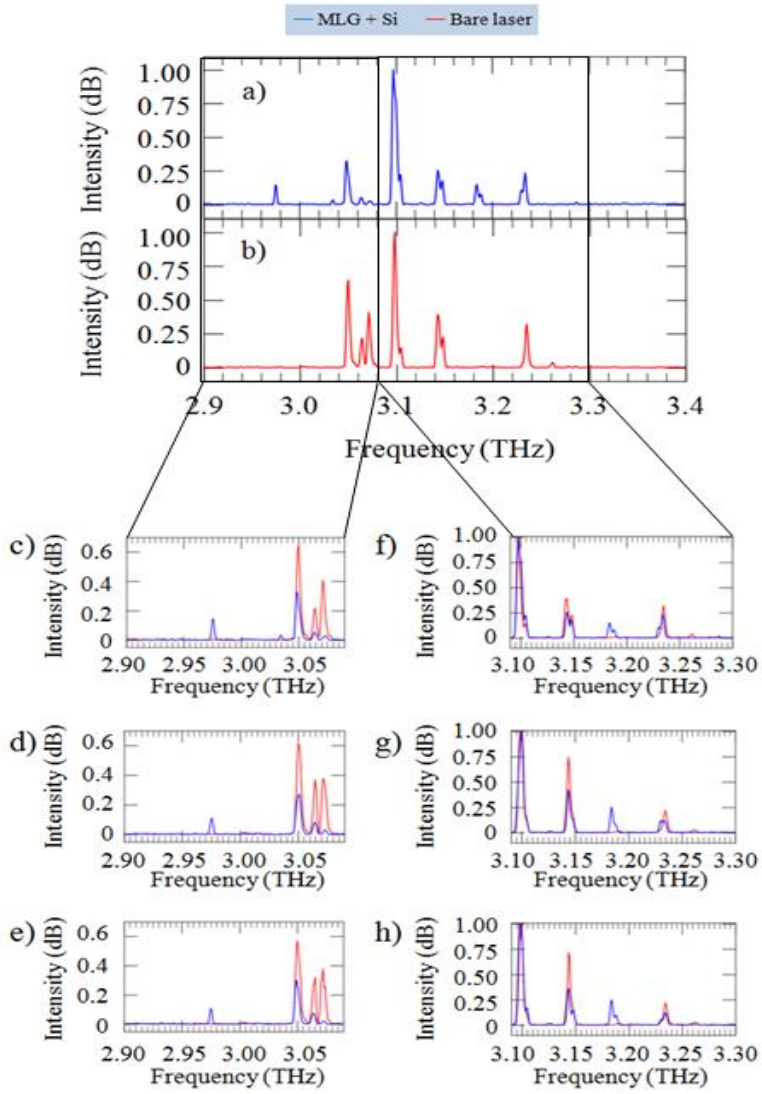

Figure 5.16: a) FTIR spectra of the radiation emitted by the random laser with r/a =26% and area of 0.70 mm^2, driven with of 470 A/cm^2 in presence of the SiO_2/Si sample coated with the multilayer graphene (MLG) grown on Nickel via CVD (blue line). b) Comparison with the FTIR spectrum of the bare laser (red line) in the same operating condition as abocve. The spectral dynamics in the region 2.90 THz - 3.09 THz is reported for an injected current density of 470 A/cm^2 (c), 510 A/cm^2 (d) and 540 A/cm^2 (e). For the range 3.10 THz - 3.30 THz, plots are shown for an injected current density of 470 A/cm^2 (f), 510 A/cm^2 (g) and 540 A/cm^2 (h).

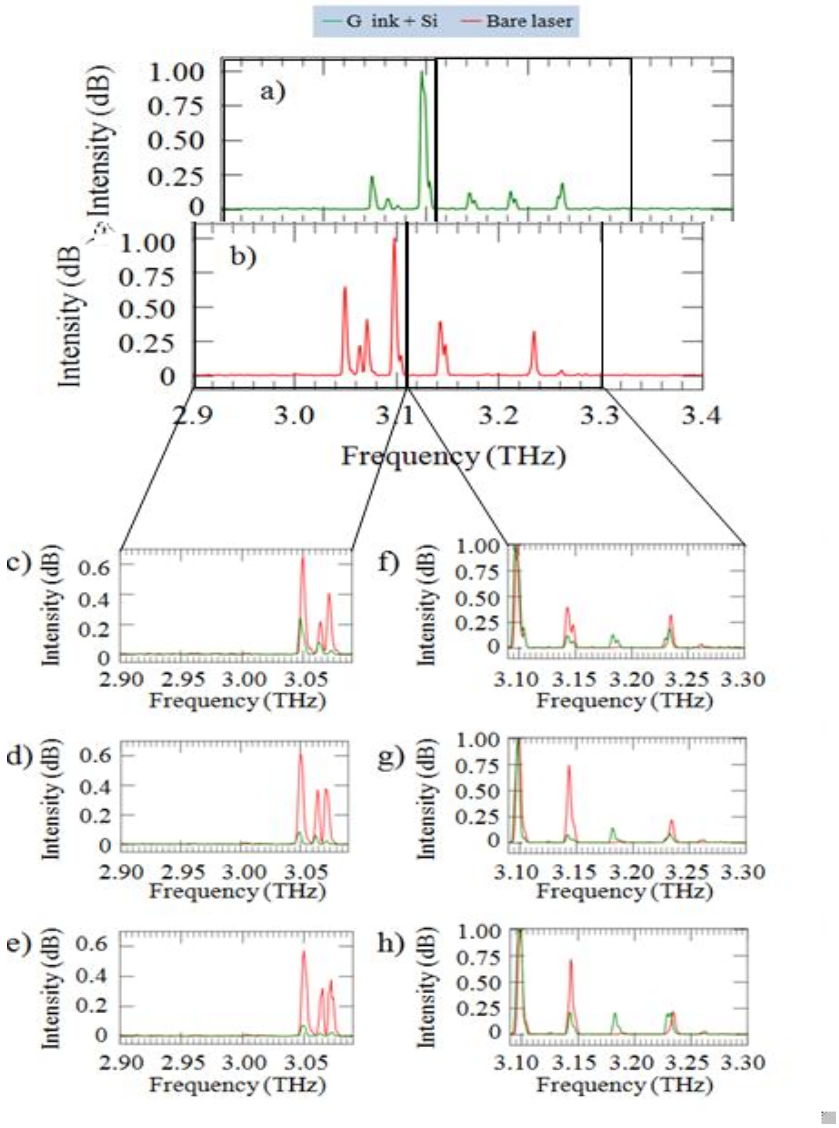

Figure 5.17: a) FTIR spectrum of the radiation emitted by the random laser with r/a =26% and area of 0.70 mm^2, driven with a current density of 470 A/cm^2 in presence of the SiO_2/Si sample coated with the water-based graphene ink (green line). b) Emission spectrum of the bare laser in the same condition as above (red line). The spectral peaks in the range 2.90 THz - 3.09 THz are shown for an injected current density of 470 A/cm^2 (c), 510 A/cm^2 (d) and 540 A/cm^2 (e). In the frequency interval comprised between 3.10 THz and 3.30 THz, plots are shown for an injected current density of 470 A/cm^2 (f), 510 A/cm^2 (g) and 540 A/cm^2 (h).

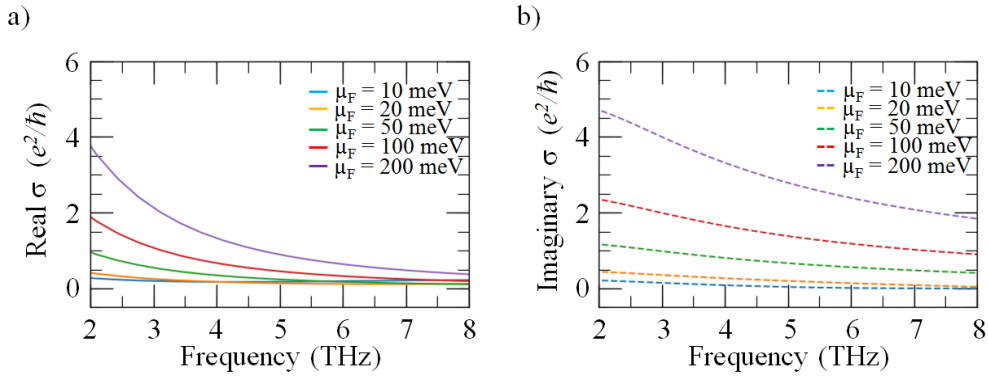

Figure 5.18: a) Real part of the sheet conductivity numerically computed for a graphene layer potential μ_F varied between 10 meV and 200 meV. b) Imaginary part of the sheet conductivity simulated for a graphene layer with the same parameter as in (a).

indicate that the emission of two sets of spectral modes is enhanced and tuned for two distinct frequency separation of 11 GHz (around 3.05 GHz) and 45 GHz (between 3.10 THz and 3.25 THz). The demonstrated feedback provided by the external graphene induces a redistribution of the peak intensity with respect to the bare laser spectra, associated to the non-trivial interaction between the graphene ink or film and the electromagnetic modes, which are emitted from the disordered top metal pattern with a complex spatial distribution.

The laser beam intensity impinging on the graphene samples can be estimated by considering a cone of radiation propagating from the laser top surface to the

range is below the far-field region, we can make a simple approximation assuming the cone has an aperture comparable to the far-field divergence (with an angular half- 0°) and defines a circle with a uniform field intensity on the target sample, while the laser signal vanishes to zero outside this circle. In these conditions, for a peak optical power of 11 mW, the ^{2}, which is one order of magnitude larger than the saturation intensity of both the graphene ink and multilayer graphene samples employed in the experiment. Therefore, we can estimate that the instantaneous emitted THz power is high enough to excite a strongly non-linear response from the 2D material, which in turn provides a feedback to the laser due to back-reflection effects. In this respect, the presence of the 350 µm-thick substrate of high-resistivity silicon does not influence significantly the THz

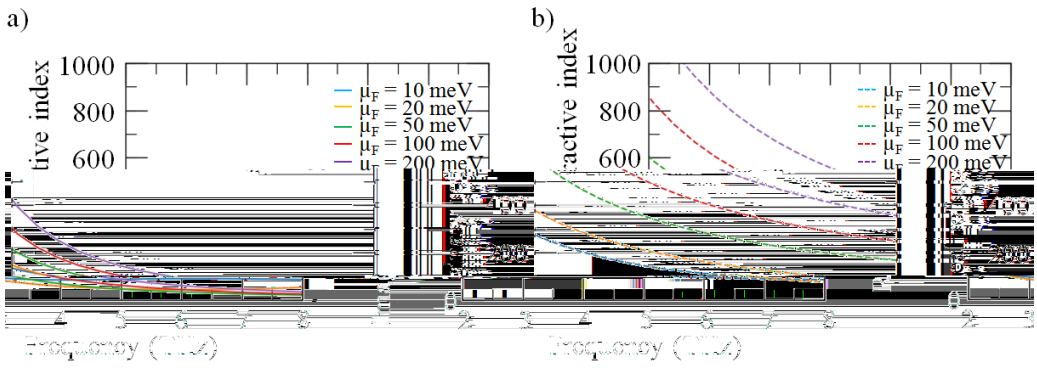

Figure 5.19: a) Real part and b) imaginary part of the refractive index of a multilayer graphene sample with a thickness of 50 layers, computed in a simplified model of low inter-layer interaction. The material conditions are an electron temperature of 20 K, a total scatter = 0.1 ps and a chemical potential μ_F varied between 10 meV and 200 meV.

$^{-1}$,[213] inducing an absorption rate below 10^{-4} per each double-pass path for light with orthogonal propagation.

However, the emission profile of a random laser is typically irregular, therefore radiation impinges on the graphene sample with regions of higher and lower field intensities, which in turn produce different degrees of coupling. Due to the intrinsic complexity of simulating the electromagnetic modes in a random laser and obtain an accurate prediction of the lasing modes, it is not feasible to describe numerically the details of the coupling between a random laser and the external graphene sample. Nonetheless, it is possible to model the conductivity and dielectric function of graphene at the operation frequencies of the laser and retrieve its optical properties. Based on the model for the graphene interband and intraband conduction introduced in Chapter 1, the real and imaginary parts of the sheet conductivity are reported in figure 5.18a and 5.18b respectively, as computed sweeping the chemical potential μ_F between 10 meV and 200 meV and

Since the graphene samples employed in the present thesis are multilayer, the model implemented the computation of the refractive index for the case of 50 layer-thick sample, cor

of low inter-layer interaction, the resulting real part of the refractive index

F F

as illustrated in figure 5.19a. In the range of emission of our random laser, the

μ_F $_F$ = 200 meV), indicating that the material thickness (see figure 5.19b). Therefore, for an increasing level of chemical potential, the graphene film is expected to damp the THz field so that it cannot penetrate too deeply and is mostly reflected back towards the THz QCLs, acting as metal-like layer. This phenomenon can be further enhanced by using a larger number of layers, which may also lead to stronger saturable absorption effects [38,39] not implemented in the proposed model for the graphene conductivity and dielectric function.

5.4 Discussion

The coupling of the radiation emitted by aperiodic THz QCLs to either an external mirror or multilayer graphene samples demonstrated an intriguing potential to achieve fine control over the spectral dynamics. While the implemented quasi-crystal and random resonator geometries allowed a coarse tuning of the emission spectra by design, the rich multimode emission was engineered with the frequency tuning and intensity modulation induced by the external coupling feedback.

Exploiting a movable mirror, a 20 GHz continuous tuning was achieved with a one-dimensional Octonacci laser, while a continuous frequency shift up to 11 GHz was demonstrated with a two-dimensional random THz QCL. The random laser tunability was further increased to 20 GHz with the discontinuous shift of multiple spectral peaks, with a periodic intensity quenching producing a mode-hopping scheme.

Using multilayer graphene grown via CVD and a water-based graphene ink as external modulators, the emission spectra of a two-dimensional random laser was modified as well. Indeed, graphene induces visible changes in the optical mode dynamics inducing two main clusters of spectral peaks with an almost

interaction between the complex radiation pattern of the laser modes and the graphene optical properties at THz frequencies. The observed phenomenon is extremely appealing for the development of mode-locked random sources. [78]

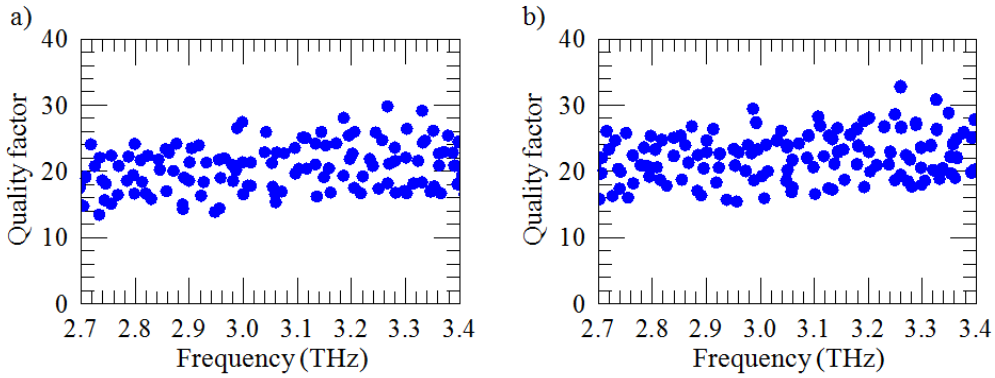

Figure 5.20: a) Plot of the three-dimensional quality factor of the eigenmodes for a random resonator (r/a = 9%, area of 0.06 mm^2) as a function of frequency. b) Simulated three-dimensional quality factors for the same resonator, having the extraction holes in the top metal surface covered by multilayer graphene with 50 layers, μ_F

The reported frequency tuning and intensity modulation of multiple spectral lines make these resonator architectures a promising platform for the development of compact multimode THz sources for pulsed and CW operation with tunable emission spectra.
This could have applications in high-resolution, multi-wavelength spectroscopy across the far-infrared spectral range, as well as high-speed parallel detection.

Moreover, a future option could be the direct integration of two-dimensional materials in the aperiodic photonic structures, in order to reach a higher degree of coupling between the THz fields and the graphene layers. Indeed, the eigenmodes of random lasers for CW operation with integrated graphene were investigated numerically, revealing that the average quality factors of the modes are increased by coating the extraction holes of the top metal surface with multilayer graphene with high chemical potential (see figure 5.20a and 5.20b). However, the presence of multilayer graphene could also lead to higher free carrier absorption losses, but stronger saturable absorption effects are also expected, associated to the high intensity of the electric fields close to the surface of the lasers. In this perspective, preliminary calibrations of the wet transfer process of graphene onto the target random photonic structures were performed, as reported in figure 5.21, showing a good yield of transfer for graphene grown on copper. By optimizing the transfer process for different

types of graphene, it could be possible to realize aperiodic THz QCLs exploiting the material's optical response and the reported saturable absorption effects. This could open new perspectives to use the ultrafast dynamics of graphene to control the spectral and temporal dynamics of the laser emission and possibly achieve passive mode-locking in the THz frequency region.

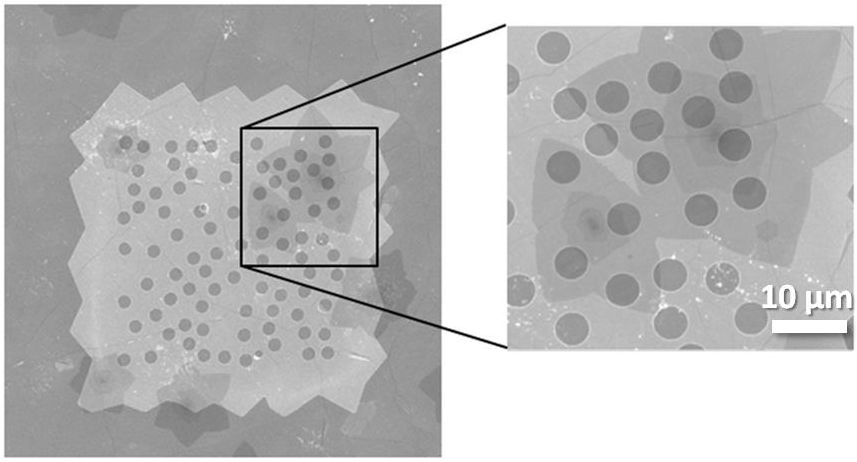

Figure 5.21: SEM image of a metal random pattern defined by optical lithography, after the transfer of a graphene layer initially grown on copper, which is mostly single-layer. The inset shows some multilayer regions corresponding to nucleation points formed during the growth.

CONCLUSIONS AND PERSPECTIVES

The present thesis aims to provide a deep understanding on the possibilities to tailor the emission and mode dynamics of THz QCLs, either by devising novel disordered photonic resonators or by exploiting the external modulation provided by multilayer graphene or coupled micro-cavities.

This thesis describes the quantum design, the fabrication and the electrical and optical characterization of double-metal quantum cascade leser resonators at THz frequencies, with the aim of demonstrating high-power emission, collimated beam profiles, fine control over the single-mode or multimode emission spectra, continuous-wave operation, record slope efficiency, fine spectral tuning.

Laterally corrugated wire lasers with a hole array lithographically defined in the top metal surface provide separate control over the light feedback and the extraction mechanism, as described in Chapter 2. Indeed, the sinusoidal corrugation of the ridge provides the main feedback wavevector and tunes the emission frequency via the definition of a photonic band structure, while the periodicity of the hole grating defines the extraction wavevector for the longitudinal edge-emission. By tuning the hole array periodicity, the optimal scattering condition was explored, reaching a maximum peak optical power of 42 mW and slope efficiency of 250 mW/A, corresponding to a narrow beam collimation (
demonstrating a maximum power of 6 mW, while maintaining robust single-mode emission at a frequency corresponding to photonic band-edge modes.

An alternative, yet deterministic aperiodic resonator concept was also investigated, based on the implementation of quasi-periodic Octonacci sequence via a slit grating in the laser top metal layer. This design supports multiple photonic pseudo-bandgaps and high quality-factor modes, which can be selectively enhanced or suppressed by changing the slit width. As illustrated in Chapter 3, multimode surface emission was demonstrated over a bandwidth of 500 GHz up to a peak power of 240 mW and a slope efficiency of ≈ 500 mW/A, while single-mode emitting devices provided around 180 mW with a spectral peak shift in frequency according to the ridge width. The grating

wavevectors induce a scattering with light producing a far-field profile consisting in two main elongated lobes at symmetric elevation angles.

In order to investigate the effect of an increased degree of disordered, two-dimensional random THz lasers were also conceived and realized, as reported in Chapter 4. Their structural disorder produces complex interference patterns for THz radiation, controlled by the size and density of the holes imprinted in the waveguide and by the absorbing boundary conditions. This results in intrinsically multimode spectra extending over a 430 GHz-wide frequency range, with a peak output power of ≈ 21 mW in pulsed regime, with surface-emitted beam profiles collimated down to a 10°-divergence. This geometry was also engineered to enable stable CW operation, with a power of at 15 K and a maximum CW operating temperature of 63 K.

Finally, manipulation and tuning of the emission of the fabricated THz QCLs were achieved with two different types of external modulations. In one case, a coupled micro-cavity provided feedback to Octonacci and random THz lasers, which could be controlled by varying the size of the external cavity, moving a mirror on a piezoelectric stage. In this way, intensity modulation and continuous frequency tuning of selected spectral lines were obtained, up to 20 GHz for an Octonacci laser and 11 GHz for a random laser.

Moreover, the possibility of exploiting the optical response of multilayer graphene was also explored, showing a visible activation of additional random modes and enhancing clusters of peaks with a regular frequency separation of 11 GHz and 45 GHz, respectively. Future investigations of the mode dynamics in aperiodic THz QCLs could benefit from the use of multilayer graphene with increased thickness to achieve even stronger non-linear effects, such as the saturable absorption reported in Chapter 5. This feedback dynamics could be further studied in future experiments, for example measuring the intermode radio-frequency beatnote associated to the coupling between distinct modes of the spectrum of aperiodic lasers operating in CW regime.

The quantum methodologies to control the emission of the THz QCLs devised and discussed in this thesis offer novel, concrete solutions to finely engineer the spectral features of the lasers as well as to optimize the photon extraction,

leading to tailored beam profiles and enhanced power output and efficiency. The possibility of using broader gain region heterostructures would provide further flexibility in tuning the single-mode or multimode emission over an even larger frequency interval, while the development of on-chip mechanical architectures would add more integrated functionalities for the laser frequency tuning.

The proposed technologies would be extremely appealing for many applications requiring fine control over the spectra in CW operation, while ensuring high spectral purity [93], such as high-resolution spectroscopy, metrology and cold atom manipulation. The tuning of the broad emission spectra of aperiodic THz QCLs offers new routes for multi-wavelength spectroscopic sensing across the far-infrared spectral range, multicolor imaging, and parallel, non-invasive inspection techniques. Moreover, the demonstrated engineering of the beam shape and direction paves the way to the control of the spatial coherence of the laser. Indeed, disordered THz QCLs offer the potential to be quantum engineered to provide high radiance and spatially incoherent emission (due to the existence of independent lasing modes with uncorrelated wave-fronts), which are really intriguing for imaging applications without coherent artifacts, such as spatial cross-talk or speckles. As an example, THz detector-less near field optical microscopes [214] can highly benefit from a spatially incoherent source for mapping locally plasmons, plasmon polaritons, carrier conductivity of 2D material-based nanodevices.

Finally, the integration of these aperiodic lasers with graphene or other novel two-dimensional materials would open completely new perspectives in the development of THz QCLs. Mode locking, as well as spatial and spectral hole burning, can be deeply altered by the non linear properties of 2D materials, opening new routes for the operation of QCLs in unexplored physical regimes.

APPENDIX A:
HETEROSTRUCTURE GROWTH SHEETS

A.1 Crystal sample V788

The sample V788 features a of a bound-to-continuum diagonal active region coupled by resonant tunneling to a single-quantum-well extractor as described in [96].
The heterostructure layers are reported below according to the chronological sequence of the growth, starting from a semi-insulating wafer of GaAs. Steps from 5S1 to 12S1 are repeated 160 times to form the active region for light amplification.

Layer	Material	[nm]	Ratio	Doping (cm^{-3})
1	GaAs	250		
2	AlGaAs	250	$Al_{50}Ga_{50}As$	
3	GaAs	700		2.00E+18
4	AlGaAs	5.5	$Al_{15}Ga_{85}As$	
Start of 160 repeat periods				
5S1	GaAs	18.4		3.00E+16
6S1	AlGaAs	4.2	$Al_{15}Ga_{85}As$	
7S1	GaAs	9.4		
8S1	AlGaAs	3.8	$Al_{15}Ga_{85}As$	
9S1	GaAs	11.5		
10S1	AlGaAs	1.8	$Al_{15}Ga_{85}As$	
11S1	GaAs	11.0		
12S1	AlGaAs	5.5	$Al_{15}Ga_{85}As$	
End of repeat periods				
13	GaAs	18.4		3.00E+16
14	AlGaAs	4.2	$Al_{15}Ga_{85}As$	
15	GaAs	20		
16	GaAs	80		5.00E+18

A.2 Crystal sample L1023

The sample L1023 is based on a laser active material with the quantum design described in [95], engineered for optimized high-temperature performance. Indeed, this material demonstrated emission up to the record temperature of 200 K.

The heterostructure layers are reported below in the chronological sequence of the growth, starting from a semi-insulating wafer of GaAs. Steps from 8S1 to 15S1 are repeated 228 times to form the active region for light amplification.

Layer	Material	[nm]	Ratio	Doping (cm^{-3})
1	GaAs	250		
2	AlGaAs	300	$Al_{50}Ga_{50}As$	
3	GaAs	70		5.00E+18
4	AlGaAs	43	$Al_{15}Ga_{85}As$	
5	GaAs	5.5		
6	GaAs	5		6.00E+16
7	GaAs	5.5		
Start of 228 repeat periods				
8S1	AlGaAs	4.1	$Al_{15}Ga_{85}As$	
9S1	GaAs	8.15		
10S1	AlGaAs	2.46	$Al_{15}Ga_{85}As$	
11S1	GaAs	8.9		
12S1	AlGaAs	4.3	$Al_{15}Ga_{85}As$	
13S1	GaAs	5.5		
14S1	GaAs	5		6.00E+16
15S1	GaAs	5.5		
End of repeat periods				
16	AlGaAs	4.1	$Al_{15}Ga_{85}As$	
17	GaAs	50		5.00E+18

APPENDIX B:
FABRICATION METHODS

B.1 Fabrication overview

Microfabrication of quantum cascade lasers needs to be performed in highly controlled environment to ensure low level of contaminating particles, air cleanliness, and specific temperature and pressure. Indeed the device production was completely carried on in cleanroom facility of the NEST (National Enterprise for nanoScience and nanoTechnology) Laboratory in Pisa, encompassing two areas with different cleanliness levels (class ISO 6 and class ISO 7).

The microfabrication procedure for a THz QCL integrating a photonic pattern in its double-metal waveguide includes the following steps:

1. A cleaved sample of the MBE-grown heterostructure and a carrier wafer of highly doped GaAs are both covered with a gold layer with thickness of 400 nm. These two pieces are then mounted with the Au surfaces in direct contact and undergo a thermocompressive wafer-bonding process at a temperature of 316°C and a pressure of 4.5 MPa for 30 minutes. In this way, the two gold layers are brought in atomic contact and form a single crystal due to the diffusion processes driven by heat and pressure.
2. The initial GaAs sample layer where the heterostructure was grown by MBE is removed by mechanical thinning and chemical etching. The lapping method is initially applied with a fine abrasive powder to thin the sample substrate down to a thickness of 50 - 100 μm. Then, the remaing part is chemically attacked with a solution of citric acid and water (1:1), with the addition of 1/3 volume of H_2O_2. The chemical etching is highly selective and stops when the protective etch-stop layer of $Al_{0.5}Ga_{0.5}As$ is reached, leaving the active region below untouched.
3. The etch-stop layer is etched using a solution of fluoridric acid (HF) at a concentration of 48%, so the active region is then directly exposed.
4. Optical ultraviolet (UV) lithography is used to define the shape of the absorbing border which are typically implemented at the edges of the laser resonators (see fig. B.1a-b).

5. The lithographically defined patterns are then covered with a chromium layer of 8 nm in a high-vacuum thermal evaporator at a pressure of

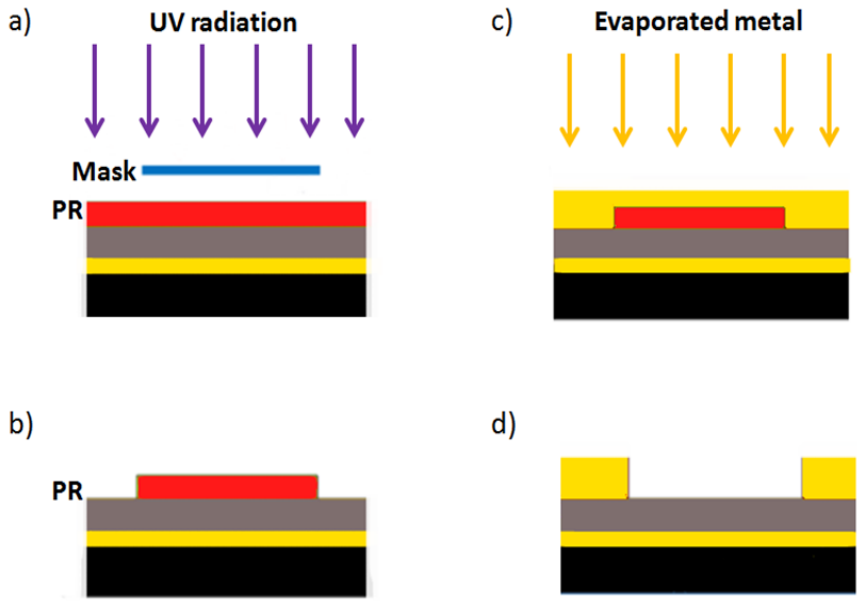

Figure B.1: Schematics of some microfabrication steps: a) the optical lithography exposure employs UV radiation passing through the transparent regions of the photomask (blue) to impress the positive photoresist (PR, in red), previously spun over the active material (gray); b) after the development only the unexposed area of the PR is left on the active material, reproducing the desired pattern; c) thermal evaporation of metal layers (such as Cr and Au, in yellow) is performed over the sample and the remaining PR; d) after the acetone-based lift-off, the PR is completely removed while the metal layer covers only the exposed region, reproducing the desired pattern.

about 10^{-5} - 10^{-6} mbar). Acetone-based lift-off methods are used to strip the metal away from all the sample, apart from the UV-exposed regions, where the Cr layer forms the absorbing boundary.

6. A second UV lithography or electron beam lithography is used to pattern the sample with the photonic structures, carefully aligned with the pre-existing Cr patterns.
7. Metal evaporation of Cr/Au (5 nm / 150 nm) is performed to define the top metal pattern. The thinner Cr layer is used as adhesive for the gold layer, whose thickness is chosen to be larger than the penetration depth

confinement. Again, lift-off with acetone is used to remove the metal

from the unexposed areas, such as slits or holes in the photonic pattern (see fig. B.1c-d)

8. Plasma-assisted dry etching is performed using a ICP-RIE (inductively coupled plasma reactive ion etching) process in order to remove the highly doped top contact layer beneath the slit and holes of the photonic geometries, while the metal-covered regions are protected by the presence of Cr and Au layers.
9. A final ICP-RIE dry-etching is used to define the device ridge/mesa, ensuring vertical sidewalls along the typical heterostructure thickness of about 10 µm. In this case, a final litography of an protective resist mask is performed on the deposited structures.
10. After mechanically thinning the back µm, the back metallization is realised evaporating Cr/Au (10 nm / 50 nm) to enable proper electrical contact of the device across the top and bottom metal claddings.
11. Manual cleaving of the sample with a diamond tip is used to separate the produced devices in pairs, which are then indium-soldered on a copper submount to provide mechanical support.
12. Finally, ultrasonic wire-bonding is used to connect each single laser to a dedicated gold-coated ceramic pad with gold wires having a diameter of 25 µm.

B.2 Optical UV lithography

Optical UV lithography is a technique which allows patterning a photosensitive polymer (resist) deposited on the target substrate, employing the interaction of UV light with the resist [215] to reproduce complex structures (i.e. photonic patterns) pre-printed on a photomask. A photolithography system (mask aligners MJB3 and MJB4 by SUSS Microtec) consists of a light source (typically, a Hg lamp), a photomask, and an optical system to convey and focus the UV radiation on the target substrate.

A uniform thin film of a a light-sensitive resist is spin-coated on top of the active region and is selectively illuminated by UV radiation through to the photomask, so that the designed geometries are transfered to a "positive" resist, i.e. a type of photoresist which becomes soluble to a specific developer in the exposed zones. There are two main protocols used for the fabrications reported

in this thesis: the single-polymer recipe with the resist s1818 and the bilayer recipe based on the resists LOR3A and s1813.
The steps required for the UV lithography with single-layer s1818 are detailed as follows:

1. Spin coating: a droplet of photoresist (s1818) is deposited on the sample and made flat by a 1 minute-long rotation at 4000 RPM, with a final . Non-uniform thick regions at the sample corners are removed with a delicate mechanical movement.
2. Soft-baking: to ensure a good adhesion of resist to the sample, while keeping the standard photosensitivity of the resist, an initial soft baking at 90°C is performed for 1 minute.
3. Pre-development: the resist-coated sample is immersed in the MF319 developer for 20s and then rinsed in water to stop the reaction, before UV exposure.
4. UV exposure: the sample is placed under the optical microscope of the high-precision MJB3 and MJB4 mask aligner. By inserting the photomask between the sample and the mirrors focusing UV radiation, UV light passes through the transparent regions of the mask and illuminate the photoresist. It is crucial that the photomask and the sample are as much in contact as possible, minimizing diffraction effects at the borders between transparent and dark regions and optimizing the exposure. The two fundamental parameters are the UV ^{2}) and the).
5. Hard-baking: immediately after the exposure, the resist is heated at 110°C for 20 s. In order not to damage the pattern tranfered to the film, a very careful control of the baking time is needed.
6. Final development: the sample is immersed in the MF319 developer for nearly 30 s and then in water again for 30 s.

The UV lithography protocol is applied different times in a fabrication, using specific regions of the photomask. First it is used for the definition of the chromium border of each device. After metal evaporation and lift-off, UV lithography is repeated to reproduce the top metallization pattern and finally for the etching mask, protecting the laser ridge or mesa from the dry-etching.
For defining structures with smaller features (down to a typical size below 2 - 3 µm), a different recipe is better suited: the bilayer protocol using a bottom

coating of LOR3A and a top coating of s1813 (having lower density than s1818), which optimize the final lift-off. The bilayer recipe consists of the following steps:

1. First spin coating: a droplet of LOR3A on the sample is spun with a 500 RPM/s acceleration for 5 s up to 500 RPM, then the rotation is brought to 3000 RPM for 60 s.
2. First pre-baking: the sample is heated at 120°C for 5 minutes.
3. Second spin coating: the sample is covered with a drop of s1813 and rotated with an initial 500 RPM/s acceleration for 5 s up to 500 RPM, then it rotates an angular speed of 4000 RPM for 60s.
4. Second pre-baking; the sample is kept at 90°C for 60 s.
5. UV exposure: the sample is placed under the optical microscope of the mask aligner. With the same procedure and lamp power described above, the optimal exposure time for the bilayer recipe is 6 s.
6. Development: the sample is immersed in the MF319 developer for 35 s and rinsed in water again for 30 s.

The choice between the two recipes also implies a different lift-off procedure: for the single-layer s1818 the simple rinsing in acetone is sufficient to remove all the residuals, while for the bilayer LOR3A + s1813 rinsing in acetone only removes the s1813 top coating and the excess metal regions. Instead the LOR3A bottom coating requires a period of 30 s in MF319, which acts as a solvent and cleans the sample surface.
Independently of the specific recipe, a proper alignment of the mask with the metal features already deposited on the target sample is critical, so that the different structures have appropriate overlap according to the preliminary CAD of the resonator, within a shift tolerance of 2 - 5 μm due to the technological limitations of the mask aligner.

B.3 Electron beam lithography

Electron beam lithography (EBL) is a technique exploiting a scanning beam of electrons which is focused on a substrate coated with an eletron-sensitive film, also called resist [216]. By exposing a region of resist to the flow of electrons, a certain dose of energy is deposited in this region making it soluble in a developer liquid. Therefore a pattern of resist-coated areas and exposed

substrate is defined on the sample for further metal evaporation and processing. Energy is transferred to the film via two processes: primary electrons from the incident beam lose energy by inelastic scattering in the material, while secondary electrons can be generated in the material by the collision of the primary ones, and can further break chemical bonds at some distance from the impact point. Current electron beam systems can reach a resolution limit of some tens of nanometers, depending on the patterning parameters.

The EBL system used in the fabrication process (based on Zeiss and Raith hardware) is made up of an electron source, a focusing system of electron optics to accelerate and funnel the electron beam and control its dispersion and aberration, and a mechanical stage in a vacuum chamber, which exploits a laser interferometry system to achieve high positioning accuracy. Unlike UV lithography, no mask is required, as the EBL directly imports CAD files with the desired patterns and translates them into machine instructions to control the beam deflection and the movements of stage on which the sample is placed during the lithography. The CAD is logically divided into separate regions (working areas, WA) by the Elphy Multibeam control software for the exposure. The patterning of the whole area is instead determined by the writefield (WF): for large structures like the random top metal patterns, the WF size is set to 1 mm with a magnification of 50x. A proper WF alignement is critical to avoid overlap between adjacent regions of the patterns and minimize the relative tilting, which could be highly detrimental for the next fabrication steps.

By selecting the appropriate beam aperture (i.e. the current flow), the acceleration voltage of the electron beam (extra high tension or EHT), the writefield parameters and the focus and astigmatism conditions, it is possible to optimize the EBL patterning. Since the structures of interest have large areas (at ^{2}) and the typical feature size is few microns, the required resolution allows reducing the patterning time while ensuring good quality with the following parameters:

- Beam aperture = 120 µm
- Beam current = -3.29 nA
- EHT = 10kV
- Dose = 105 µC/cm^2

The recipe for the electron-sensitive resist deposition and development is detailed here:

1. Spin-coating: a drop of PMMA resist (AR 679.04) covers the sample and is spun for 60 s at an angular speed of 4000 RPM, resulting in a resist thickness of about 270 nm
2. Pre-baking: the sample is heated at a temperature of 120°C for 12 minutes
3. EBL exposure: the patterning is performed setting the above-mentioned parameters
4. Final development: the exposed sample is rinsed in the developer AR 600-56 for 2 minutes, then in isopropanol for 1 minute

B.4 Thermal evaporation of metals

After a previous step of optical lithography or EBL, metal evaporation is required to deposit metals on the exposed patterns of the sample.
Thin-film deposition of metals is performed by evaporating a source material in a custom thermal evaporator by Sistec with a vacuum chamber operated at a very low pressure (between 10^{-5} mbar and 10^{-6} mbar). For uniform deposition and optimal adhesion of the evaporated metals on the target sample, the latter needs to be positioned as flat as possible and the chamber pressure needs to be very low to minimize contamination due to other materials. Control over the deposited metal thickness is provided by a quartz crystal used as a micro-scale. At the end of the evaporation, the whole sample surface is completely coated. A successive lift-off rinsing in acetone helps removing the excess metal and leaves the desired metal patterns on the sample surface. The final quality of the deposition process result is determined by the undercut profile given by the UV exposure and the correct development of the resist.

B.5 Wet etching

Wet ecthing reactions exploit liquid-phase etchants to remove material layers from the sample. The etching process needs to be highly selective, so that only the target layers are removed with a high corrosion rate, leaving the underlying layers untouched due to a much lower local etching rate. Moreover, anisotropic etching is required to form well-defined, vertical structures such as the side-walls of laser ridges and mesas. This effect for some etchants and materials

(like GaAs) [217] depends on the crystallographic orientation of the substrate, since it gives different etching rates along the different material directions and produces strong anisotropy.
In the microfabrication of double-metal THz QCLs wet etching is used twice:

1. the initial GaAs substrate on top of the heterostructure is removed using a solution of citric acid and water (1:1), with the addition of 1/3 volume of H2O2. The citric etching is highly selective and stops when the underlying $Al_{0.5}Ga_{0.5}As$ etch stop layer is exposed.
2. This protective layer which caps the laser active material is removed by immersing the sample in a small amount of fluoridric acid (HF) with a concentration of 48%.

B.6 Plasma-assisted dry etching

Plasma-assisted dry etching is based on the ICP-RIE technology, i.e. the "inductively coupled plasma for reactive-ion etching", which can be calibrated to achieve controlled etching rate and vertical sidewalls. In this machine (Sentech SI 500), the sample is loaded in the high-vacuum chamber where different type of gases (BCl_3, Cl_2 and Ar) are pumped with dedicated mass flow controllers at specific rates. This gas mixture is transformed into a plasma by a high frequency source field oscillating at 13.6 GHz with power of hundreds of Watt, while a separate radiofrequency field at 2.4 GHz accelerates the ions with voltages up to hundreds of Volts: therefore ICP-RIE allows independent tuning of the concentration of the chemicals in the plasma and the ion energy of impact on the sample. Indeed, the process exploits two etching mechanisms:

- chemical etching: it is controlled by the concentration of chlorine gases (BCl_3, Cl_2), which have high oxidizing action;
- physical etching: it is dominated by the mechanical impact of the accelerated particles (in particular, Argon).

By calibrating the source power and the acceleration power, as well as the chemistry of the reaction, dry etching provides more control over the undercut and the etching depth.
ICP-RIE dry-etching is employed twice in the THz QCL fabrication protocol: it is used for defining the ridge or mesa of the final devices (with a typical thickness of 10 μm), and to remove the top contact layer (with a standard thickness of 700 nm) in correspondence of the patterned apertures (slits, holes)

in the top metallization (see fig. B.2), to enhance light extraction and reduce the ohmic losses.

The dry etching of ridges/mesas exploits a mixture of BCl_3:Cl_2:Ar (5:5:5) at a pressure of 0.2 Pa, with an acceleration RF power of 30 W and a source power of 500 W, with an average etchin .

The etching of the top contact layer is based on a concentration of BCl_3:Cl_2:Ar (6:1:10) at a pressure of 0.2 Pa, with an acceleration RF power of 25 W and a source power of 100 W. The resulting etching ra

25 μm-diameter, pinned on the metal layers using an ultrasonic wedge-bonder by Kulicke & Soffa Industries. By contacting each laser with a dedicated gold-coated pad, each device can be electrically driven independently when mounted in a cryostat for low-temperature operation.

B.8 Graphene wet transfer

A calibration of the graphene wet transfer on random top metal patterns was performed. The used graphene was grown via CVD on Copper (Cu) and kindly provided by Dr N. Mishra (Italian Institute of Technology, NEST Laboratory).
The transfer procedure involves the protection of the graphene with a polymer (PMMA), the etching of the Cu substrate and the subsequent transfer on the target semiconductor material. The detailed steps are reported below:

1. Sample cleaning in acetone (1 minute) and isopropanol (1 minute)
2. PMMA spin coating at 4000 RPM for 1 minute
3. Sample baking at 90°C for 2 minutes
4. Cleaning of the back side of Cu with a cotton bud and acetone
5. Removal of the of graphene residuals on the back of Cu with standard graphene etching recipe in RIE for 1 minute (80 sccm Ar, 5 sccm O_2).
6. Overnight etching of the Cu substrate in a copper etchant solution (3 g of ammonium persulfate, APS, in 100 ml of water).
7. Dilution of the solution by triple washing of the graphene membranes with water for 5 minutes each time
8. Keeping the graphene membranes in water for further 30 minutes
9. Final fishing of graphene films with the target substrate
10. Complete drying of the films on the substrate, kept under the hood for 60 minutes.
11. Gaphene baking at 150°C for 3 hours for optimal adhesion to the substrate
12. Removal of the PMMA residuals keeping the samples in acetone for 2 hours, followed by rinsing in isopropanol.
13. Drying of the graphene and the substrate with N_2 blower.

APPENDIX C:
NUMERICAL METHODS

C.1 Finite element method

The finite element method (FEM) is a numerical approach often exploited in computational photonics to solve Maxwell's partial differential equations when analytical solutions are not feasible. Unlike the conventional analytical approach, FEM does not consider the problem domain as a continuous region, but splits the space into a set of basic geometric elements, forming a "mesh". Considering the whole meshed geometry, the continuous problem is mapped into a discrete one, and the solution is locally computed in each element. The typical mesh element is a segment in 1D, a triangle in 2D and a tetrahedron in 3D (figure C.1). Specific algorithms govern the discretization of the domain, in order to reproduce as accurately as possible the physical system geometry. Using an unstructured grid, it is possible to achieve a different spatial resolution to characterize system features with different sizes, for example, slits and holes in the top metal surface, irregular protrusions in the device border, etc.

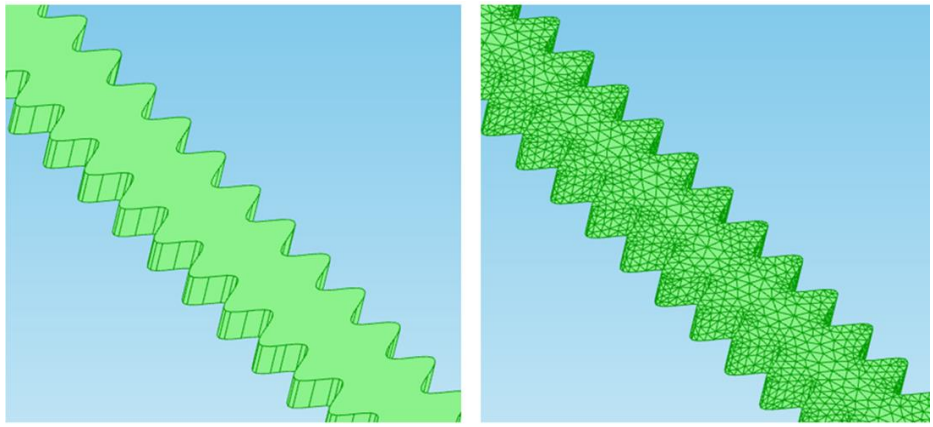

Figure C.1. Example of sinusoidal laser cavity (left) composed as a tetrahedral mesh (right) on which Maxwell's equations are numerically solved.

The physical properties of the different parts of the system can be described by introducing their specific material properties, such as refractive index, conductivity, dielectric function or other appropriate quantities.

Once the initial conditions of the model are defined, the system of partial differential equations is converted into a matrix problem by introducing a basis of functions (for example, polynomials) for each mesh elements, whose values are to be determined.
Subsequently, the simulation program (COMSOL Multiphysics) proceeds with the assembly of the so-called "stiffness matrix" which contains all the unknowns and associated relations. A number of different algorithms are available to find the solutions to the problem, exploiting advanced linear algebra techniques: in most cases, these algorithms employ iterative methods, consisting in an initial guess of the solving functions which is later refined in successive steps of approximations. Once the solutions converge to stable values within the required tolerance, the results are available for analysis and visualization. A proper solution needs to be stable with respect to slight changes or errors in the initial input. In this respect, the mesh quality is central, since it needs to be accurate and sufficiently regular: for example, spiky mesh elements (triangles or tetrahedrons with small angles) are very detrimental for the stiffness matrix quality and lead to typically unstable solutions.
Another crucial point of the model definition is the proper implementation of the boundary conditions to provide a realistic description of the physical problem, for example, to mimic the propagation of light to free space or to introduce metallic surfaces acting as mirrors.

C.2 Mathematical description and optimization

A discretized unknown function f (**r**), such as the electric/magnetic field components, defined over the spatial coordinates **r**, can be written on using a set of N basis functions $\{b_n(\mathbf{r})\}$ [63] so that:

$$f(\mathbf{r}) = \sum_{n=0}^{N} c_n b_n(\mathbf{r}) \tag{61}$$

with unknown coefficients c_n. The system of differential equations can be written in terms of an operator L such that:

$$\widehat{L} f(\mathbf{r}) = g(\mathbf{r}) \tag{62}$$

By taking the inner product with N weight functions $\{w_m\}$, these equations can be transformed into algebraic formulae:

$$\sum_{n=0}^{N} (w_m, \widehat{L} b_n)\, c_n = (w_m, g) \tag{63}$$

Depending on the chosen weight functions wm, different methods of solution can be implemented, which lead to a matrix formulation of the problem. In the case of the numerical computation of the resonating electromagnetic modes is reduced to the form of a generalized stationary eigenproblem:

$$Ax = \omega^2 Bx \tag{64}$$

where A and B are N x N complex matrices and x is the eigenvector. This problem could be attacked [2]
and the corresponding eigenvector x. However, this traditional diagonalization method requires a computer memory proportional to N^2 and a computation time growing as fast as N^3.
A much more efficient approach exists, exploiting the fact that only a few of the N eigenvectors are physically relevant, for example because only the low-energy solutions need to be investigated. A number of iterative methods (such as Lanczos or Arnoldi iterations) have been developed to provide a fast solution for a small number $p << N$ of desired eigenvalues and eigenvectors. By setting an initial guess x_0 for the eigenvector, i.e. a string of random values, the matrix operator is applied repeatedly, resulting in a rapid convergence to the true eigenvector. Indeed, the matrix-vector products Ax and Bx can be computed in a time which scales linearly with N and these matrices are typically sparse in FEM models, these iterative methods are much more efficient than the full conventional diagonalization. At each iteration step the needed computer memory scales with pN, while the computation time grows as $\sim pN^2 << N^3$.

C.3 Quality factor simulation

FEM electromagnetic models are always limited to a finite-size volume, light propagation from the resonator to free space requires special conditions to be realistically simulated. Some boundaries of the volume needs to be implemented in such a way that radiation hitting them is not reflected back but propagates toward infinity, therefore accounting for radiation losses. Two main conditions are available for this scope:

- the perfectly matched layer (PML) which is a thick external region around the resonator is designed as an effective, artificial material to absorb light with minimal back reflection;
- the scattering boundary condition (SBC), which is a line (in 2D) or a surface (in 3D) at the border of the simulated volume, which does not reflect at all light propagating orthogonally to it. For other directions of light propagation the back-reflection cancellation is less effective.

In this way, finite quality factors can be retrieved for the eigenmodes, indicating which ones are more efficiently confined and therefore more likely to be amplified and give laser action. Indeed, the associated eigenfrequencies have complex values:

$$\nu = \frac{\omega_0 - i\delta}{2\pi} \tag{65}$$

from which the quality factor is obtained:

$$Q = \frac{\omega_0}{2\delta} \tag{66}$$

Other particular conditions can be imposed on the system surfaces (not necessarily on the domain borders. [218] In the work presented in this thesis, the metal layers are treated as perfect electric conductor (PEC) surfaces. For a PEC surface with normal direction **n,** any incident electric field **E** is completely reflected with no losses, independently of its frequency, according to the condition:

$$\mathbf{n} \times \mathbf{E} = 0 \tag{67}$$

C.4 Far-field computation

Apart from the computation of the stationary resonating modes in a resonator, a FEM model can be used also to simulate the beam propagation of an electromagnetic mode in the far-field region. This can be used to predict the beam divergence, in particular when the resonator supports high-quality-factor modes which can be correlated to the FTIR emission spectra of the devices.

Let us consider the near-field electric field **E** and magnetic field **H** in the plane S where the top metal surface of the resonator lies, with a normal direction **n**

and coordinate **r** = (x,y). In the far-field region, at a point $\mathbf{r_0}$, the propagating electric field is given by the Stratton-Chu transform formula [219]:

$$\mathbf{E_{ff}} = \frac{ik_{rad}}{4\pi}\mathbf{r_0} \times \int (\mathbf{n} \times \mathbf{E} - \sqrt{\frac{\mu_0}{\varepsilon_0}}\mathbf{r_0} \times (\mathbf{n} \times \mathbf{H}))e^{ik_{rad}\mathbf{r}\cdot\mathbf{r_0}}dS \tag{68}$$

where k_{rad} is the free-space radiation wavevector, and μ_0 $_0$ are the vacuum permittivity and dielectric constants respectively.
Finally, the emitted far-field profile I_{ff} is proportional to the Poyinting vector modulus, therefore:

$$I_{ff} \sim |\mathbf{E_{ff}}|^2 \tag{69}$$

APPENDIX D:
EXPERIMENTAL METHODS

D.1 Cryogenic cooling

THz QCLs require cryogenic cooling due to the intrinsic limitation of the heterostructure design which currently limit the operation temperature to 210 K in pulsed mode[19].

For the transport characterization of the fabricated devices, a dedicated cryostat was used, exploiting a closed-circuit helium mechanism, based a chamber through which cold helium vapor is pumped and then recycled. The helium chamber is in thermal contact with an oxygen-free copper cylinder, on top of which the laser chip holder, called "cold finger", is placed (see figure D.1). The thermal cycles allows reaching a stable minimum temperature of about 10 K on the cold finger, as measured with a local temperature probe, but an external heater can be used to vary the temperature to the desired setpoint value, so that the laser performance can be measured for different temperatures. The copper cylinder and the cold finger are surrounded by a metal vacuum chamber pumped at a low pressure (10^{-5} mbar). The electrical injection to drive the laser is ensured by a system of micro-coaxial cables which allows driving up to two devices per chip at once, while a system of resistors provides the required impedance matching for the laser drivers. A similar criostat was also used for the FTIR measurements, using a continuous flow of liquid helium to reach a miminum temperature of about 8 K on the cold finger, with the laser off.

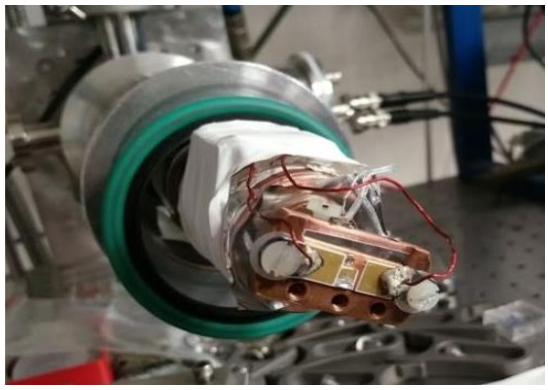

Figure D.1: Photograph of the cryostat cold finger used for the transport and optical charazterization of surface-emitting THz QCLs.

D.2 Electrical drive

Depending on the type of THz QCL, laser operation can be achieved either in pulsed mode or in continuous-wave (CW) regime.

In the first case, THz QCLs are electrically driven by a pulser, i.e. a voltage generator providing a train of short, periodic voltage pulses, typically square waves. By setting the output voltage, the pulse width (PW) and the pulse repetition rate (f), the laser reaches a given operation condition in terms of supplied bias and current injection. The pulse train is also characterized by the percentage of time in which the signal is non-zero, called "duty cycle" (DC), which is given by the formula $DC = PW \cdot f$.

Depending on the explored duty cycle range, different pulsers were used in the experiments reported in this thesis. The pulser by Avtech Electrosystems allowed reaching a maximum DC = 10%, while the one by Agilent provided at most a DC of 95%. Moreover, a driver for positive bias (QCL2000+ by Wavelength Electronics Inc.) was used to drive some resonators in CW regime, limited to a maximum current output of 2 A.

D.3 Terahertz radiation detection

For the optical characterization of the fabricated resonators, different detectors were chosen to measure the optical power and the emitted beam shape.

A pyroelectric sensor by Infrared Systems Development Corp. was used, exploiting the temporary voltage produced by a temperature variation on a crystal, illuminated by the impinging THz radiation

mm^2). Then a voltage signal is produced and amplified by the sensor, with a value correlated to the intensity of the beam at the position of the detector. This signal needs also to be filtered by a lock-in amplifier, sensitive to both frequency and phase, reducing the noise thanks to a square wave modulation with a frequency of 33Hz. In this way, the generation of the THz pulses from the QCL and their detection on the sensor are synchronized. The sensitivity of the detector is assessed in terms the noise-equivalent power (NEP), which is the signal power giving a signal-to-noise ratio equal to 1, in an integration time of 0.5s. In this case, the sensor has NEP = 0.5 $nW/Hz^{1/2}$.

For the measurements of the current-voltage characteristics, the pyroelectric sensor was placed in front of the device, at a fixed distance of 1.5 cm, to collect the radiation emitted by the laser and transmitted through the thermoplastic cyclic olefin cryostat window, with a transmission coefficient of 75%.

A second detector, the TK absolute terahertz power meter by Thomas Keating Ltd., was also used to accurately assess the laser output power. This sensor has ^{2}) formed by a two partly transparent, parallel membranes enclosing a small air volume and separated by a thin metal film. The temperature variation of the gas due to the incident THz radiation corresponds to a pressure variation, which is measured by a trasducer and correlated to the THz power, thanks to an initial self-calibration done dissipating a known amount of ohmic power in the film. The TK power meter has a typical NEP of 5 W/Hz$^{1/2}$ and features a dedicated lock-in system.

D.4 Far-field intensity pattern measurements

The far field intensity profile of a laser is measured at a distance much larger than its typical emission wavelength. This is achieved by mounting the pyroelectric sensor on a holder at a given distance of more than 6 cm, typically, from the surface of the laser hosted on the cryostat cold finger. The position of the detector was scanned along a spherical surface by moving a system of linear and angular stages by Physik Instrumente GmbH, controlled by a LabView program. The spatial resolution of the far-field scan was typically set to 3 mm, with the appropriate waiting time set to be twice the lock-in integration time.

D.5 FTIR spectroscopy

The Fourier transform infrared (FTIR) spectroscopy is a high-sensitivity technique allowing the collection of signal over a broad frequency spectrum, collecting all the THz laser emission wavelengths simultaneously. The FTIR is based on a Michelson interferometer, consisting of a fixed mirror, a beam splitter and a mirror that translates back and forth, with high spatial resolution. In the performed experiments, the external source of radiation is a fabricated THz QCL, whose radiation is conveyed to the beamsplitter (BS) which divides light in two beams. While the first beam is transmitted through the BS and reaches the fixed mirror, the second beam is reflected by the BS to the moving mirror. The fixed and moving mirrors reflect the radiation back to the BS, and this results in one beam passing to the detector and the second back to the source (see figure D.2).

The optical path difference between the beams travelling through the two arms of the interferometer depends on the position of the moving mirror. The initial distance of the moving mirror from the BS is the same as the one between the

fixed mirror and the BS, but then a mirror displacement , inducing an optical path difference OPD = 2n , where n is the refractive index of the medium filling the interferometer volume. For different discrete values of , the intensity of radiation is measured by a detector, producing an intensity profile ("interferogram") as a function of the mirror displacement. For a zero OPD, all the collected wavelengths are in-phase and interfere constructively. The achievable resolution depends only on the maximum optical path difference. For the experiments reported in this thesis, two different a FTIR spectrometers were used. The one by Thermo Fisher Scientific Inc. provided a maximum resolution of 0.125cm^{-1}, while the FTIR spectrometer by Bruker (Vertex 80v) gave a maximum resolution of 0.06 cm^{-1} and benefited from the vacuum pumping of the FTIR volume (down to a pressure of 2 hPa), which strongly reduced the effects of air absorption which is crucial at THz frequencies. In both cases, he measurements were performed using a deuterated triglycine sulfate-based detector (DTGS-KBr), and the laser emission spectra were retrieved by applying the Fast Fourier Transform to the spatial interferogram.

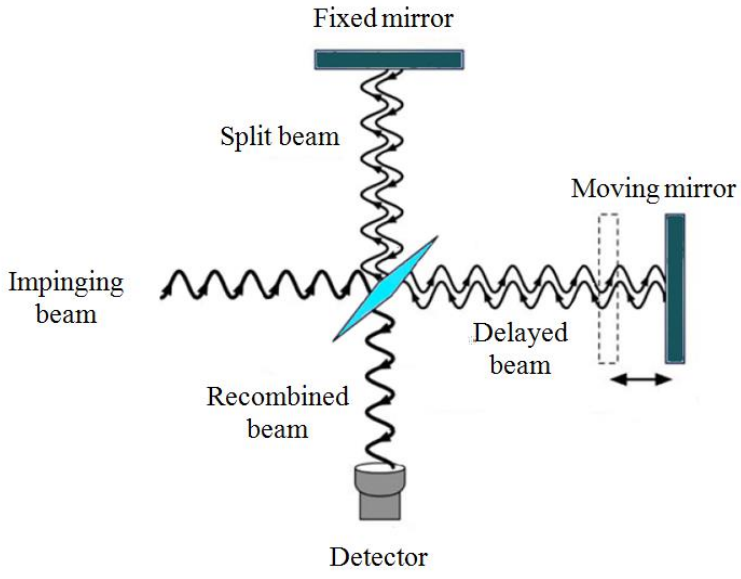

Figure D.2: Schematic diagram of the FTIR interferometric arms and optics, showing the beam propagation from the source to the internal detector.

BIBLIOGRAPHY

[1] Tonouchi, M., Cutting-edge terahertz technology, Nat. Photon. 1, 97 105 (2007) DOI: 10.1038/nphoton.2007.3

[2] Eisele, M., Cocker, T.L., Huber, M.A., Plankl, M., Viti, L., Ercolani, D., Sorba, L., Vitiello, M.S., Huber, R., Ultrafast multi-terahertz nano-spectroscopy with sub-cycle temporal resolution. Nat. Photon. 8, 841 845 (2014) DOI: 10.1038/nphoton.2014.225

[3] Zhao, G., Schouten, R. N., van der Valk, N.,Wenckebach,W. T.& Planken, P. C. M., Design and performance of a THz emission and detection setup based on a semi-insulating GaAs emitter, Rev. Sci. Instrum. 73, 1715 1719 (2002) DOI: 10.1063/1.1459095

[4] Bonvalet, A., Joffre, M., Martin, J.-L., Migus, A., Generation of ultrabroadband femtosecond pulses in the mid-infrared by optical rectification of 15 fs light pulses at 100 MHz repetition rate, Appl. Phys. Lett. 67, 2907 2909 (1995) DOI: 10.1063/1.114838

[5] Kaindl, R. A., Eickemeyer, F.,Woerner, M. & Elsaesser, T., Broadband phasematched difference frequency mixing of femtoseconds pulses in GaSe: Experiment and theory, Appl. Phys. Lett. 75, 1060 1062 (1999) DOI: 10.1063/1.124596

[6] Ryzhii,V., Khmyrova, I., Shur, M. S., Terahertz photomixing in quantum well structures using resonant excitation of plasma oscillations, J.Appl. Phys. 91, 1875 1881 (2002) DOI: 10.1063/1.1431436

[7] Williams, G. P., Far-IR/THz radiation from the Jefferson Laboratory, energy recovered linac, free electron laser, Rev. Sci. Instrum. 73, 1461 1463 (2002) DOI: 10.1063/1.1420758

[8] Brown, E. R.,McIntosh, K. A., Nichols, K. B., Dennis, C. L., Photomixing up to 3.8 THz in low-temperature-grown GaAs, Appl. Phys. Lett. 66, 285 287 (1995). DOI: 10.1063/1.113519

[9] Kawase, K., Sato, M., Taniuchi, T., Ito, H., Coherent tunable THz-wave generation from LiNbO3 with monolithic grating coupler, Appl. Phys. Lett. 68 2483 2485 (1996) DOI: 10.1063/1.115828

[10] Shikata, J., Kawase, K., Sato, M., Taniuchi, T., Ito, H., Enhancement of Terahertz wave output from LiNbO3 optical parametric oscillators by cryogenic cooling, Opt. Lett. 24, 202 204 (1999) DOI: 10.1364/OL.24.000202

[11] Ferguson, B., Zhang, X.-C., Materials for terahertz science and technology, Nature Materials, 1, 1, pp. 26 - 33 (2002) DOI: 10.1038/nmat708
[12] Köhler, R., Tredicucci, A., Beltram, F., Beere, H.B., Linfield, E.H., Davies, A.G., Ritchie, D.A., Iotti, R.C., Rossi, F., Terahertz semiconductor-heterostructure laser, Nature 417, 156 159 (2002) DOI:10.1038/417156a
[13] Cho, A. Y., Molecular Beam Epitaxy, AIP Press, Woodbury, USA (1997)
[14] Liu, H. C., Capasso, F., Intersubband transitions in Quantum Wells: Physics and Device Application I, Academic Press, San Diego, USA (2000)
[15] Vitiello, M.S., Scalari, G., Williams, B., De Natale P., Quantum Cascade Lasers: twenty years of challenges, Opt. Express 23, 4, 5167 - 5182 (2015) DOI: 10.1364/OE.23.005167
[16] Li, L., Kundu, I., Dean, P., Linfield, E.H., Davies, A.G., High-power GaAs/AlGaAs quantum cascade lasers with emission in the frequency rage 4.7-5.6 THz, International Quantum Cascade Laser School and Workshop - IQCLSW (2016)
[17] Brandstetter, M., Deutsch, C., Krall, M., Detz, H., MacFarland, D.C., Zederbauer, T., Andrews, A.M., Schrenk, W., Strasser, G., Unterrainer, K., High power terahertz quantum cascade lasers with symmetric wafer bonded active regions, Appl. Phys. Lett. 103(17), 171113 (2013) DOI: 10.1063/1.4826943
[18] Li, L., Chen, L., Zhu, J., Freeman, J., Dean, P., Valavanis, A., Davies, A.G., Linfield, E.H., Terahertz quantum cascade lasers with >1 W output powers, Electron. Lett. 50(4), 309 311 (2014) DOI: 10.1049/el.2013.4035
[19] Bosco, L., Fanckié, M., Scalari, G., Beck, M., Wacker, A., Faist, J., Thermoelectrically cooled THz quantum cascade laser operating up to 210 K, Appl. Phys. Lett 115, 010601 (2019) DOI: 10.1063/1.5110305
[20] Wienold, M., Röben, B., Schrottke, L., Sharma, R., Tahraoui, A., Biermann, K., Grahn, H. T., High-temperature, continuous-wave operation of terahertz quantum-cascade lasers with metal-metal waveguides and third-order distributed feedback, Opt. Express 22, 3334 3348 (2014) DOI: 10.1364/OE.22.003334
[21] Mahler, L., Köhler, R., Tredicucci, A., Beltram, F., Beere, H.E., Linfield, E.H., Ritchie, D.A., Davies, A.G., Single-mode operation of terahertz quantum cascade lasers with distributed feedback resonators. Applied Physics Letters, 84, 26, pp. 5446 to 5448 (2004) DOI: 10.1063/1.1767957

[22] Williams, B. S., Kumar, S., Hu, Q., Reno, J.L., Distributed-feedback terahertz quantum cascade lasers with laterally corrugated metal waveguides, Optics Express, 30, 21 (2005) DOI: 10.1364/OL.30.002909
[23] Fan, J. A., Belkin, M. A., Capasso, F., Khanna, S., Lachab, M., Davies, A. G., Linfield, E. H., Surface emitting terahertz quantum cascade laser with a double-metal waveguide, Opt. Exp., 14, pp.11672 11680, (2006) DOI: 10.1364/oe.14.011672
[24] Kumar, S., Williams, B.S., Qin, Q., Lee, A.W., Hu, Q., Reno, J.L., Surface-emitting distributed feedback terahertz quantum-cascade lasers in metal-metal waveguides, Opt. Exp., vol. 15, pp. 113 128 (2007) DOI: 10.1364/oe.15.000113
[25] Amanti, M. I., Fischer, M., Scalari, G., Beck, M., Faist, J., Low-divergence single-mode terahertz quantum cascade laser, Nature Photonics 3, 586 590 (2009) DOI:10.1038/nphoton.2009.168
[26] Chassagneux, Y., Colombelli, R., Maineult, W., Barbieri, S., Beere, H. E., Ritchie, D. A., Khanna, S. P., Linfield, E. H., Davies, A. G., Electrically pumped photonic-crystal terahertz lasers controlled by boundary conditions, Nature, 457, 174-178 (2009) DOI:10.1038/nature07636
[27] Zhang, H., Dunbar, L. A., Scalari, G., Houdré, R. & Faist, J., Terahertz photonic crystal quantum cascade lasers. Opt. Express 15, 16818 16827 (2007)
[28] Castellano, F., Zanotto, S., Li, L.H., Pitanti, A., Tredicucci, A., Linfield, E.H., Davies, A.G., Vitiello, M.S., Distributed feedback terahertz frequency

broadband directional emission, Optica, 3, 10, 1035-1038 (2016) DOI: 10.1364/OPTICA.3.001035
[33] Zeng, Y., Liang, G., Liang, H.K., Masha, S., Meng, B., Liu, T., Hu, X., Tao, J., Li, L., Davies, A.G., Linfield, E.H., Zhang, Y., Chong, Y., Wang, Q.J. Designer multimode localized random lasing in amorphous lattices at terahertz

10.1021/acsphotonics.6b00711
[34] Zeng, Y., Liang, G., Qiang, B., Wu, K., Tao, J., Hu, X., Li, L. Davies, A.G., Linfield, E.H., Liang, H.K., Zhang, Y., CHong, Y., Wang, Q.J., Two-Dimensional Multimode Terahertz Random Lasing with Metal Pillars, ACS Photonics, 5 (7), pp 2928 2935, (2018) DOI: 10.1021/acsphotonics.8b00260
[35] Vicarelli, L., Vitiello, M.S., Coquillat, D., Lombardo, A., Ferrari, A.C., Knap, W., Polini, M., Pellegrini, V., Tredicucci, A., Graphene field-effect transistors as room-temperature terahertz detectors, Nature Materials, 11, 10, pp. 865-871 (2012) DOI: 10.1038/nmat3417
[36] Lee, S. H., Choi,M., Kim, T.T., Lee, S., Liu, M., Yin, X., Choi, H.K., Lee, S.S., Choi, C.G., Choi,S.Y., Zhang, X., Min, B., Switching terahertz waves with gate-controlled active graphene metamaterials, Nat. Mater. 11, 936 941 (2012) DOI: 10.1038/nmat3433
[37] Sensale-Rodriguez, B., Fang, T., Yan, R.S., Kelly, M.M., Jena, D., Liu, L., Xing, H.L., Unique prospects for graphene-based terahertz modulators, Appl. Phys. Lett. 99, 11 (2011) DOI: 10.1063/1.3636435
[38] Bianco,F., Miseikis,V., Convertino,D., Xu,J.X., Castellano,F., Beere,H.E., Ritchie,D.A., Vitiello,M.S., Tredicucci,A., Coletti,C., THz saturable absorption in turbostratic multilayer graphene on silicon carbide. Opt. Express 23, 11632 11640 (2015) DOI: 10.1364/oe.23.011632
[39] Bianchi, V., Carey, T., Viti, L., Li, L., Linfield, E.H., Davies, A.G., Tredicucci, A., Yoon, D., Karagiannidis, P.G., Lombardi, L., Tomarchio, F., Ferrari, A.C, Torrisi, F., Vitiello, M.S., Terahertz saturable absorbers from liquid phase exfoliation of graphite, Nature Communications, 8, 15763 (2017) DOI: 10.1038/ncomms15763
[40] Biasco, S., Garrasi, K., Castellano, F., Li, L., Beere, H.E., Ritchie, D.A., Linfield, E.H., Davies, A.G.,Vitiello, M.S., Continuous-wave highly-efficient low-divergence terahertz wire lasers, Nature Communications, 9, 1122-1 - 1122-8 (2018) DOI:10.1038/s41467-018-03440-4

[41] Biasco, S., Ciavatti, A., Beere, H.E., Ritchie, D.A., Li, L., Davies, A.G., Linfield, E.H., Vitiello, M.S., Highly efficient surface-emitting semiconductor lasers exploiting quasi-crystalline distributed feedback photonic patterns, *manuscript submitted*
[42] Biasco, S., Beere, H.E., Ritchie, D.A., Li, L., Davies, A.G., Linfield, E.H., Vitiello, M.S., Frequency-tunable continuous-wave random lasers at terahertz frequencies, Light: Science & Applications 8, 43 (2019) DOI: 10.1038/s41377-019-0152-z
[43] Faist, J., Quantum Cascade Lasers. Oxford University Press, Oxford, UK (2013)
[44] Kazarinov, R.F., Suris, R.A., Possibility of the amplification of electromagnetic waves in a semiconductor with a superlattice. Soviet Physics-Semiconductors, 5, 4 (1971)
[45] Faist, J., Capasso, F., Sivco, D.L., Sirtori, C., Hutchinson, A.L., Cho, A.Y, Quantum Cascade Laser, Science, 264, 5158, pp. 553-556 (1994) DOI: 10.1126/science.264.5158.553
[46] Liu, H.C., Capasso, F., Intersubband transitions in Quantum Wells: Physics and Device Application I. Academic Press, San Diego, USA (2000)
[47] Williams, B.S, Terahertz quantum-cascade lasers. Nature Photonics, 1, 517 (2007) DOI: 10.1038/nphoton.2007.166
[48] Lu, Q.Y, Razeghi, M., Recent advances in room-temperature, high-power terahertz quantum cascade laser sources based on difference-frequency generation, Photonics, 3 (3), 42 (2016) DOI: 10.3390/photonics3030042
[49] Razeghi, M., Recent progress of widely tunable, CW THz source based QCLs at room temperature, Terahertz Science and Technology, 10, 4 (2017) DOI: 10.11906/TST.087-151.2017.12.07
[50] Belkin, M. A., Capasso, F., Xie, F., Belyanin, A., Fischer, M., Wittman, A., Faist, J., Room temperature terahertz quantum cascade laser source based on intracavity difference-frequency generation, Appl. Phys. Lett., 92, 201101 (2008).
[51] Lu, Q. Y., Wu, D. H., Sengupta, S., Slivken, S., Razeghi, M., Room temperature continuous wave, monolithic tunable THz sources based on highly efficient mid-infrared quantum cascade lasers, Sci. Rep., 6, 23595 (2016).
[52] Lu, Q. Y., Bandyopadhyay, N., Slivken, S., Bai, Y., Razeghi, M., Room temperature single-mode terahertz sources based on intracavity difference-

frequency generation in quantum cascade lasers, Appl. Phys. Lett., 99, 131106 (2011).
[53] Lu, Q. Y., Bandyopadhyay, N., Slivken, N., et al. ,Widely-tuned room temperature terahertz quantum cascade laser sources based on difference frequency generation, Appl. Phys. Lett., 101, 251121 (2012).
[54] Lu, Q. Y., Wang, F., Wu, D., Slivken, S., Razeghi, M., Room temperature terahertz semiconductor frequency comb, Nature Communications 10, 2403 (2019) DOI: 10.1038/s41467-019-10395-7
[55] Faist, J., Wallplug efficiency of quantum cascade lasers: Critical parameters and fundamental limits, Applied Physics Letters, 90, 253512 (2007) DOI: 10.1063/1.2747190
[56] Yu, P., Cardona, M., Fundamentals of Semiconductors, Springer, Berlin Germany (1996)
[57] Köhler, R., Terahertz Quantum Cascade Lasers, Ph.D. thesis, Scuola Normale Superiore, Pisa, Italy (2003)
[58] Yariv, A., Yeh, P., Photonics, Oxford University Press, Oxford, UK (2006)
[59] Kogelnik, H., Shank, C.V., Stimulated emission in a periodic structure, Appl. Phys. Lett. 18, 152 (1971) DOI: 10.1063/1.1653605
[60] Vitiello, M.S.; Tredicucci, A. Tunable Emission in THz Quantum Cascade Lasers, IEEE Trans. Terahertz Sci. Technol. 1, 76-84 (2011).
DOI: 10.1109/TTHZ.2011.2159543
[61] Kogelnik, H.; Shank, C.V. Coupled-wave theory of distributed feedback lasers, J. Appl. Phys. 43, 2327 (1972). DOI: 10.1063/1.1661499
[62] Joannopoulos, J.D., Johnson, S.G., Winn, J.N., Meade, R.D., Photonic Crystals: Molding the Flow of Light, Princeton University Press, Princeton, USA (2003)
[63] Yablonovitch, E., Inhibited spontaneous emission in solid-state physics and electronics, Phys. Rev. Lett. 58, 2059 2062 (1987) DOI: 10.1007/978-1-4615-1963-8_41
[64] Halioua, Y., Xu, G., Moumdji, S., Li, L.H., Davies, A.G., Linfield, E.H., Colombelli, R., THz quantum cascade lasers operating on the radiative modes of a 2D photonic crystal, Optics Letters, 39 ,13,3962-3965 (2014) DOI: 10.1364/OL.39.003962
[65] Levine, D., Steinhardt, P.J., Quasicrystals. I. Definition and structure, Phys. Rev. B, 34, 596 616 (1986) DOI: 10.1103/PhysRevB.34.596

[66] Socolar, J.E.S., Steinhardt, P.J., Quasicrystals. II, Unit-cell configurations. Phys. Rev. B, 34, 617 647 (1986) DOI: 10.1103/PhysRevB.34.617
[67] Vardeny, Z.V., Nahata, A., Agrawal, A., Optics of photonic quasicrystal, Nat. Photonics, 7, 177 187 (2013) DOI: 10.1038/nphoton.2012.343
[68] Mahler, L., Photonic structures for Terahertz Quantum Cascade Lasers, Ph.D. thesis, Scuola Normale Superiore, Pisa, Italy (2012)
[69] Notomi, M., Suzuki, H., Tamamura, T., Edagawa, K., Lasing action due to the two-dimensional quasiperiodicity of photonic quasicrystals with a Penrose lattice, Phys. Rev. Lett., 92, 12 (2004) DOI: 10.1103/physrevlett.92.123906
[70] Wiersma, D.S., The physics and applications of random lasers, Nature Physics 4, 359 - 367 (2008) DOI: 10.1038/nphys971
[71] Wiersma, D.S., Disordered photonics, Nature 7, 188-196 (2013) DOI: 10.1038/nphoton2013.29
[72] Segev, M., Silberberg, Y., Christodoulides, D.N. Anderson localization of light. Nature Photonics, 7, 197-204 (2013) DOI: 10.1038/nphoton.2013.30
[73] Letokhov, V.S., Generation of light by scattering medium with negative resonance absorption, Soviet Phys. JETP 26, 4, 835-840 (1968)
[74] Wiersma, D.S. and Lagendijk, A., Light diffusion with gain and random laser, Phys. Rev. E, 54, pp.4256-4265 (1996) DOI: 10.1103/PhysRevE.54.4256
[75] Andreasen, J., Sebbah, P., Vanneste, C., Nonlinear effects in random lasers, J. Opt. Soc. Am. B, 28, 12, 2947-2955 (2011) DOI: 10.1364/JOSAB.28.002947
[76] Cao, H., Review on latest developments in random lasers with coherent feedback, J. Phys. A: Math. Gen., 10497 10535, 38 (2005) DOI: 10.1088/0305-4470/38/49/004
[77] Ioffe, A. F., Regel, A. R. Non-crystalline, amorphous and liquid electronic semiconductors, Prog. Semicond. 4, 237 291 (1960)
[78] Leonetti, M., Conti, C., Lopez, C.,, The mode locking transition in random lasers. Nature photonics, 5, 10 (2011) DOI: 10.1038/nphoton.2011.217
[79] Lawandy, N. M., Balachandram, R.M., Gomes, A.S.L., Sauvain, E., Laser action in strongly scattering media, Nature 368, 436-438 (1994) DOI: 10.1038/368436a0
[80] Wiersma, D. S. & Cavalieri, S., A temperature-tunable random laser, Nature 414, 708 709 (2001) DOI: 10.1038/414708a

[81] Song, Q., Xiao, S., Xu, Z., Liu, J., Sun, X., Drachev, V., Shalev, V.M., Akkus, O., Kim, Y.L., Random lasing in bone tissue, Optics Letters, 35, 9, 1425-1427 (2010) DOI: 10.1364/OL.35.001425
[82] Liang, H.K., Meng, B., Liang, G., Tao, J., Chong, Y., Wang, Q.J., Zhang, Y., Electrically Pumped Mid-Infrared Random Lasers, Adv. Mater. 25, 6859 6863 (2013) DOI:10.1002/adma.201303122
[83] Wienold, M.; Tahraoui, A.; Schrottke, R.; Sharma, R.; Lu, X.; Biermann, K.; Hey, R.; Grahn, H.T. Lateral distributed-feedback gratings for single-mode, high-power terahertz quantum-cascade lasers, Opt. Express 20, 11207-11217 (2012). DOI: 10.1364/OE.20.011207
[84] Xu, G.; Colombelli, R.; Khanna, S.P.; Belarouci, A.; Letartre, X.; Li, L.; Linfield, E.H.; Davies, A.G.; Beere, H.E.; Ritchie, D.A. Efficient power extraction in surface-emitting semiconductor lasers using graded photonic heterostructures, Nat. Commun., 3, 952(2012). DOI: 10.1038/ncomms1958
[85] Xu, G.; Li, L.; Isac, N.; Halioua, Y.; Davies, A.G.; Linfield, E.H.; Colombelli, R., Surface-emitting terahertz quantum cascade lasers with continuous-wave power in the tens of milliwatt range, Appl. Phys. Lett. 104, 091112 (2014). DOI: 10.1063/1.4866661
[86] Kao, T.-Y.; Reno, J.L.; Hu, Q. Phase-locked laser arrays through global antenna mutual coupling, Nat. Photon. 10, 541 546 (2016). DOI: 10.1038/nphoton.2016.104
[87] Kao, T.-Y.; Hu, Q.; Reno, J.L. Perfectly phase-matched third-order distributed feedback terahertz quantum-cascade lasers, Opt. Lett. 37, 2070-2072 (2012). DOI: 10.1364/OL.37.002070
[88] Xu, L.; Curwen, C.A; Hon, P.W.C.; Chen, Q.-S.; Itoh, T.; Williams, B.S. Metasurface external cavity laser, Appl. Phys. Lett. 107, 221105 (2015). DOI: 10.1063/1.4936887
[89] Amanti, M.I.; Scalari, G.; Castellano, F.; Beck, M.; Faist, J. Low divergence Terahertz photonic-wire laser, Opt. Express 8, 6390-6395 (2010). DOI: 10.1364/OE.18.006390
[90] Wienold, M.; Röben, B.; Schrottke, L.; Sharma, R.; Tahraoui, A.; Biermann, K,; Grahn, H.T. High-temperature, continuous-wave operation of terahertz quantum-cascade lasers with metal-metal waveguides and third-order distributed feedback, Opt. Express 22, 3334 3348 (2014). DOI: 10.1364/OE.22.003334

[91] Kao, T.-Y.; Cai, X.; Alan, W.M.; Reno, J.L., Hu, Q. Antenna coupled photonic wire lasers, Opt. Express 23, 17091-17100 (2015). DOI: 10.1364/OE.23.017091
[92] Wu, C.; Khanal, S.; Reno, J.L.; Kumar, S. Terahertz plasmonic laser radiating in an ultra-narrow beam, Optica, 3, 7, pp. 734-740 (2016). DOI: 10.1364/OPTICA.3.000734
[93] Vitiello, M.S.; Consolino, L.; Bartalini, S.; Taschin, A.; Tredicucci, A.; Inguscio, M; De Natale, P., Quantum-limited frequency fluctuations in a terahertz laser, Nat. Photonics 6, 525 (2012). DOI: 10.1038/nphoton.2012.145
[94] Qiu, M. Effective index method for heterostructure-slab-waveguide-based two-dimensional photonic crystals, Appl. Phys. Lett. 2002, 81, 1163 1165 (2002). DOI: 10.1063/1.1500774
[95] Fathololoumi, S.; Dupont, E.; Chan, C.W.I.; Wasilewski, Z.R.; Laframboise, S.R.; Ban, D.; Matyas, A.; Jirauschek, C.; Hu, Q.; Liu, H. C. Terahertz quantum cascade lasers operating up t
oscillator strength and improved injection tunneling. Opt. Express, 20, 4, 3866 (2012). DOI: 10.1364/OE.20.003866
[96] Amanti, M.I.; Scalari, G.; Terrazzi, R.; Fischer, M.; Beck, M.; Faist, J.; Rudra, A.; Gallo, P.; Kapon, E. Bound-to-continuum terahertz quantum cascade laser with a single-quantum-well phonon extraction/injection stage. New J. Phys., 11, 125022 (2009). DOI: 10.1088/1367-2630/11/12/125022
[97] Vitiello, M.S.; Scamarcio, G.; Spagnolo, V.; Alton, J.; Barbieri, S.; Worrall, C.; Beere, H.D.; Ritchie, D.A.; Sirtori, C. Thermal properties of THz quantum cascade lasers based on different optical waveguide configurations. Appl. Phys. Lett., 89, 021111 (2006). DOI: 10.1063/1.2220546
[98] Castellano, F., Bianchi, V., Li, L., Zhu, J., Tredicucci, A., Linfield, E.H., Davies, A.G., Vitiello, M.S., Tuning a microcavity-coupled terahertz laser, Appl. Phys. Lett., 107, 261108 (2015) DOI: 10.1063/1.4938207
[99] Morthier, G., Vankwikelberge, P. Handbook of Distributed Feedback Laser Diodes, Artech House, Boston, USA (1997).
[100] Golka,S., Pflügl, C., Schrenk, W., Strasser, G., Quantum cascade lasers with lateral double-sided distributed feedback grating, Applied Physics Letters, 86, 11 (2005) DOI: 10.1063/1.1883332
[101] Mahler, L., Köhler, R., Tredicucci, A., Beltram, F., Beere, H.E., Linfield, E.H., Ritchie, D.A., Davies, A.G., Single-mode operation of terahertz quantum

cascade lasers with distributed feedback resonators. Applied Physics Letters, 84, 26, pp. 5446 - 5448 (2004) DOI: 10.1063/1.1767957
[102] Vitiello, M.S., Scalari, G., Williams, B., De Natale P., Quantum Cascade Lasers: twenty years of challenges, Opt. Express 23, 4, 5167 - 5182 (2015) DOI: 10.1364/OE.23.005167
[103] Bartalini, S., Consolino, S., Cancio, L., De Natale, P., Bartolini, P., Taschin, P., De Pas, A., , Beere, H., Ritchie, D., Vitiello, M.S., Torre, R., Frequency-Comb-Assisted Terahertz Quantum Cascade Laser Spectroscopy, Phys. Rev. X 4, 021006 (2014) DOI: 10.1103/PhysRevX.4.021006
[104] Locatelli, M., Ravaro, M., Bartalini, S., Consolino, L., Vitiello, M.S., Cicchi, R., Pavone, F., De Natale, P., Real-time terahertz digital holography with a quantum cascade laser, Scientific Reports, 5, 13566 (2015) DOI: 10.1038/srep13566
[105] Hübers, H.-W., Pavlov, S. G., Richter, H., A.D., High-resolution gas phase spectroscopy with a distributed feedback terahertz quantum cascade laser, Appl. Phys. Lett. 89, 061115 (2006) DOI: 10.1063/1.2335803
[106] Fasching, G., Benz, A. & Unterrainer, K., Terahertz microcavity quantum cascade lasers, Appl. Phys. Lett. 87, 211112 (2005) DOI: 10.1063/1.2136222
[107] Szedlak, R., Hisch,T., Schwarz,B., Holzbauer,M., MacFarland,D., Zederbauer,T., Detz,H., Andrews,A.M., Schrenk,W., Rotter, S., Strasser,G., Ring quantum cascade lasers with twisted wavefronts, Scientific Reports 8, 7998 (2018) DOI: 10.1038/s41598-018-26267-x
[108] Jin, Y., Gao, L., Chen, J., Wu, C., Reno, J.L., Kumar, S., High power surface emitting terahertz laser with hybrid second- and fourth-order Bragg gratings, Nat. Commun., 9, 1407 (2018), DOI:10.1038/s41467-018-03697-9
[109] Chassagneux, Y., Colombelli, R., Maineult, W., Barbieri, S., Khanna, S. P., Linfield, E. H., A. G. Davies, A. G., Graded photonic crystal terahertz quantum cascade lasers, Appl. Phys. Lett. 96, 031104 (2010) DOI: 10.1063/1.3273056
[110] Zeng, Y., Liang, G., Qiang, B., Meng, B., Liang, H.K., Mansha, S., Li, J., Li, Z., Li, L., Davies, A.G., Linfield, E.H., Zhang, Y., Chong, Y., Wang, Q.J., Terahertz emission from localized modes in one-dimensional disordered systems, Photonics Research, 6, 2, 117-122 (2018) DOI: 10.1364/PRJ.6.000117
[111] Yuan, H.Q., Grimm, U., Repetowicz, P., Schreiber, M., Energy spectra, wave functions, and quantum diffusion for quasiperiodic systems, Phys. Rev. B, 62, 15 569-15578 (2000) DOI: 10.1103/PhysRevB.62.15569

[112] Brandão, E.R., Costa, C.H., Vasconcelos, M.S., Anselmo, D.H.A.L., Mello, V.D., Octonacci photonic quasicrystals, Optical Materials 46, 378 383 (2015) DOI: http://dx.doi.org/10.1016/j.optmat.2015.04.051
[113] Sirtori, C., Barbieri, S., Colombelli, R., Wave engineering with THz quantum cascade lasers, Nature Photonics, 7, pp. 691-701 (2013) DOI: 10.1038/nphoton.2013.208
[114] Rousseau, M. Statistical properties of optical fields scattered by random media. Application to rotating ground glass. J. Opt. Soc. Am. 61, 10, 1307-1316 (1971) DOI: 10.1364/JOSA.61.001307
[115] Wiersma, D. S., Bartolini, P., Lagendijk, A., Righini, R. Localization of light in a disordered medium, Nature 390, 671 673 (1997) DOI: 10.1038/37757
[116] Mafi, A., Karbasi, S., Kock, K.W., Hawkins, T., Ballato, J. Transverse Anderson localization in disordered glass optical fibers: a review. Materials, 7, 5520-5527 (2014), DOI:10.3390/ma7085520
[117] Garcia, P.D., Sapienza, R., Bianco, A., Lopez, C., Photonic glass: A novel random material for light, Adv. Mat. 19, 18, 2697-2602 (2007) DOI: 10.1002/adma.200602426
[118] Yina, H., Donga, B., Liua, X., Zhana, T., Lei Shia, Zia, J., Yablonovitch, E. Amorphous diamond-structured photonic crystal in the feather barbs of the scarlet macaw. PNAS, 109, 27, 10798-10801 (2012)
[119] Segev, M., Silberberg, Y., Christodoulides, D.N. Anderson localization of light. Nature Photonics, 7, 197-204 (2013) DOI: 10.1038/nphoton.2013.30
[120] Gouedard, C., Husson, D., Sauteret, C., Auzel, F., Migus, A., Generation of spatially incoherent short pulses in laser-pumped neodymium stoichiometric crystals and powders, J. Opt. Soc. Am. B 10, 12, 2358-2362 (1993) DOI: 10.1364/JOSAB.10.002358
[121] Agnew, G., Grier, A., Taimre, T., Lim, Y.L., Nikolic, M., Valavanis, A., Cooper, J., Dean, P.,. Khanna, S.P., Lachab, M., Linfield, E.H., Davies, A.G., Harrison, P., Ikonic, Z., Indjin, D., Rakic, A.D., Efficient prediction of terahertz quantum cascade laser dynamics from steady-state simulations, Appl. Phys. Lett. 106, 161105 (2015) DOI: 10.1063/1.4918993
[122] Qi, X., Kundu, I., Dean, P., Agnew, G., Taimre, T., Valavanis, A., Grier, A.T., Linfield, E.H., Davies, A.G., Indjin, D., Rakic, A.D. Mode Selection and Tuning Mechanisms in Coupled-Cavity Terahertz Quantum Cascade Lasers, IEEE J. Sel. Top. Quantum Electron., 23, 4, (2017) DOI: 10.1109/JSTQE.2017.2668600

[123] Jiang, X., Feng, S., Soukoulis, C.M., Zi, J., Joannopoulos, J.D., Cao, H., Coupling, competition, and stability of modes in random lasers, Phys. Rev. B, 69, 104202-1 - 104202-7 (2004) DOI:10.1103/PhysRevB.69.104202
[124] Redding, B., Choma, M. A. & Cao, H. Spatial coherence of random laser emission, Opt. Lett. 36, 3404-3406 (2011). DOI: 10.1364/OL.36.003404
[125] Florescu, L. & John, S. Photon statistics and coherence in light emission from a random laser. Phys. Rev. Lett. 93, 013602 (2004). DOI: 10.1103/PhysRevLett.93.013602
[126] Cao, H., Ling, Y., Xu, J. Y., Cao, C. Q. & Kumar, P. Photon statistics of random lasers with resonant feedback. Phys. Rev. Lett. 86, 4524 4527 (2001). DOI: 10.1103/PhysRevLett.86.4524
[127] Redding, B., Choma, M.A., Cao, H. Speckle-free laser imaging using random laser illumination, Nature Photonics 6, 355 (2012). DOI: 10.1038/nphoton.2012.90
[128] Polson, R. C., Varden, Z. V., Random lasing in human tissues. Appl. Phys. Lett. 85, 1289 1291 (2004). DOI: 10.1063/1.1782259
[129] Choe, R., Corlu, A., Lee, K., Durduran, T., Konecky, S.D., Grosicka-Koptyra M, Arridge SR, Czerniecki BJ, Fraker DL, De Michele A, Chance B, Rosen MA, Yodh AG. Diffuse optical tomography of breast cancer during neoadjuvant chemotherapy: a case study with comparison to MRI., Med. Phys. 32, 1128 1139 (2005). DOI: 10.1118/1.1869612
[130] Lahini, Y., Avidan, A., Pozzi, F., Sorel, M., Morandotti, R., Christodoulides, D.N., Silberberg, Y., Anderson Localization and Nonlinearity in One-Dimensional Disordered Photonic Lattices, Phys. Rev. Lett. 100, 013906 (2008) DOI: 10.1103/PhysRevLett.100.013906
[131] Schwartz, T., Bartal, G., Fishman, S., Segev, M., Transport and Anderson localization in disordered two-dimensional photonic lattices, Nature 446, pp:52 55 (2007) DOI: 10.1038/nature05623
[132] Ghofraniha, N., La Volpe, L., Van Opdenbosch, D., Zollfrank, C., Conti, C., Biomimetic random lasers with tunable spatial and temporal coherence. Adv. Opt. Mater. 4, 1998 2003 (2016) DOI: 10.1002/adom.201600649
[133] Tsai, C.Y., Liao, Y.M., Liao, W.C., Lin, W.J., Perumal, P., Hu, H.H, Lin, S.Y., Chang, C.H., Cai, S.Y., Sun, T.M., Lin, H.I., Haider, G., Chen, Y.F., Magnetically controllable random lasers, Adv. Mater. Technol. 2, 1700170 (2017) DOI: 10.1002/admt.201700170

[134] Wiersma, D. S., Cavalieri, S. A temperature-tunable random laser. Nature 414, 708 709 (2001) DOI: /10.1038/414708a
[135] Zhai, T., Chen, J., Chen, L., Wang, J., Wang, L., Liu, D., Li, S., Liu, H., Zhang, X., A plasmonic random laser tunable through stretching silver nanowires embedded in a flexible substrate. Nanoscale 7, 2235 2240 (2015) DOI: 10.1039/c4nr06632d
[136] Gottardo, S., Cavalieri, S., Yaroshchuk, O., Wiersma, D.S., Quasi-two-dimensional diffusive random laser action. Phys. Rev. Lett. 93, 263901 (2004) DOI: 10.1103/physrevlett.93.263901
[137] Alam, T., Wienold, M., Lue, X., Biermann, K., Schrottke, L., Grahn, H.T., Huebers, H.-W., Wideband, high-resolution terahertz spectroscopy by light-induced frequency tuning of quantum-cascade lasers, Optics Express, 7, 4, 5420 (2019) DOI: 10.1364/OE.27.005420
ková, D., Amanti, M.I., Scalari, G., Beck, M., Faist, J., Electrically tunable terahertz quantum cascade lasers based on a two-sections interdigitated distributed feedback cavity, Appl. Phys. Lett. 106, 131107 (2015) DOI: 10.1063/1.4916653
[139] Benz, A., Deutsch, C., Brandstetter, M., Andrews, A.M., Klang, P., Detz, H., Schrenk, W., Strasser, G., Unterrainer, K., Terahertz Active Photonic Crystals for Condensed Gas Sensing, Sensors 11, 6003 (2011). DOI: 10.3390/s11060600310
[140] Turcinkova,D., Amanti,M.I., Castellano,F., Beck,M., Faist,J., Continuous tuning of terahertz distributed feedback quantum cascade laser by gas condensation and dielectric deposition, Appl. Phys. Lett. 102, 181113 (2013) DOI: 10.1063/1.4803483
[141] Qin, Q., Williams, B.S., Kumar, S., Reno, J.L., Hu, Q., Tuning a terahertz wire laser, Nat. Photonics 3, 732 (2009) DOI: 10.1038/nphoton.2009.218
[142] Qin, Q., Reno, J.L., Hu, Q., MEMS-based tunable terahertz wire-laser over 330 GHz, Opt. Lett. 36, 692 694 (2011) DOI: 10.1364/OL.36.000692
[143] Kundu, I., Dean, P., Valavanis, A., Chen, L., Li, L., Cunnigham, J.E., Linfield, E.H., Davies, A.G., Quasi-continuous frequency tunable terahertz quantum cascade lasers with coupled cavity and integrated photonic lattice,
Optics Express, 25, 1, 486 (2017) DOI: 10.1364/OE.25.000486
[144] Hugi, A., Maulini, R., Faist, J., External cavity quantum cascade laser, Semicond. Sci. Technol. 25, 083001 (2010) DOI: 10.1088/0268-1242/25/8/083001

[145] Meng, B., Wang, Q.J., Broadly tunable single-mode mid-infrared quantum cascade lasers, J. Opt. 17, 023001 (2015) DOI: 10.1088/2040-8978/17/2/023001
[146] Xu, J., Hensley, J.M, Fenner, D.B., Green, R.P., Mahler, L., Tredicucci, A., Allen M.G., Beltram, F., Beere, H.E., Ritchie, D.A., Tunable terahertz quantum cascade lasers with an external cavity, Appl. Phys. Lett. 91, 121104 (2007) DOI:10.1063/1.2786587
[147] Schwaighofer, A., Alcaráz, M.R., Araman, C., Goicoechea, H., Lendl, B., External cavity-quantum cascade laser infrared spectroscopy for secondary structure analysis of proteins at low concentrations, Scientific Reports 6, 33556 (2016) DOI: 10.1038/srep33556
[148] Ostendorf, R., Butschek, L., Hugger, S., Fuchs, F., Yang, Q., Jarvis, J., Schilling, C., Rattunde, M., Merten, A., Grahmann, J., Boskovic, D., Tybussek, T., Rieblinger, K., Wagner, J., Recent Advances and Applications of External Cavity-QCLs towards Hyperspectral Imaging for Standoff Detection and Real-Time Spectroscopic Sensing of Chemicals, Photonics 2016, 3, 2, 28 (2016) DOI: 10.3390/photonics3020028
[149] Mahler, L., Tredicucci, A., Beltram, F., Beere, H.E., Ritchie, D.A., Tuning a distributed feedback laser with a coupled microcavity, Optics Express, 18, 18, 19185-19191 (2010). DOI: 10.1364/OE.18.019185
[150] Castellano, F., Bianchi, V., Li, L., Zhu, J., Tredicucci, A., Linfield, E.H., Davies, A.G., Vitiello, M.S., Tuning a microcavity-coupled terahertz laser, Appl. Phys. Lett., 107, 261108 (2015). DOI:10.1063/1.4938207
[151] Marcuse, D., Coupled mode theory of optical resonant cavities, IEEE J. Quantum Electron., 21, 1819 (1985). DOI: 10.1109/JQE.1985.1072590
[152] French,P.M.W., The generation of ultrashort laser pulses, Rep. Prog. Phys. 58, 169 (1995) DOI: 10.1088/0034-4885/58/2/001

-

integrated terahertz modulators, Nanophotonics 7, 1, pp:127 144 (2018)
[154] Sensale Rodriguez B, Yan R, Rafique S, et al. Extraordinary control of terahertz beam reflectance in graphene electroabsorption modulators, Nano Lett 12, 4518 22 (2012) DOI: 10.1021/nl3016329
[155] Gopalan, P., Chanana, A., Krishnamoorty, S., Nahata, A., Scarpulla, M.A., Sensale-Rodriguez, B., Ultrafast THz modulators with WSe2 thin films, Optical Materials Express, 9, 2, pp. 826-836 (2019) DOI: 10.1364/OME.9.000826

[156] Novoselov, K.S., Geim, A.K., Morozov, S.V., Jiang, D., Zhang, Y., Dubonos, S.V., Grigorieva, I.V., Firsov, A.A., Electric Field Effect in Atomically Thin Carbon Films, Science, 306, 5696, pp. 666-669 (2004) DOI: 10.1126/science.1102896
[157] Falkovsky, L.A., Optical properties of graphene, J. Phys.: Conf. Ser. 129, 012004 (2008) DOI: 10.1088/1742-6596/129/1/012004
[158] Yamashita, S., Nonlinear optics in carbon nanotube, graphene and related 2D materials, APL Photonics 4, 034301 (2019) DOI: 10.1063/1.5051796
[159] Tassin, P., Koschny, T., Soukoulis, C.M., Graphene for Terahertz Applications, Science, 341, 6146 (2013) DOI: 10.1126/science.1242253
[160] Wang, M., Yang, E.H., THz applications of 2D materials: graphene and beyond, Nano-Structures & Nano-Objects 15, pp.107 113 (2018) DOI: 10.1016/j.nanoso.2017.08.011
[161] Yadav, D., Tamamushi, G., Watanabe, T., Mitsushio, J., Tobah, Y., Sugawara, K., Dubinov, A.A., Satou, A., Ryzhii, M., Ryzhii, V., Otsuji, T., Terahertz light-emitting graphene-channel transistor toward single-mode lasing, Nanophotonics, 7, 4 (2018) DOI: 10.1515/nanoph-2017-0106
[162] Dubinov, A.A., Bylinkin ,A., Aleshkin, V.Y., Ryzhii, V., Otsuji, T., Svintsov, D., Ultra-compact injection terahertz laser using the resonant inter-layer radiative transitions in multi-graphene-layer structure, Optics Express 24, 26, pp. 29603-29612 (2016) DOI:10.1364/OE.24.029603
[163] Yadav, D., Tombet, S.B., Watanabe, T., Arnold, S., Ryzhii1, V., Otsuji, T., Terahertz wave generation and detection in double-graphene layered van der Waals heterostructures, 2D Materials, 3, 4 (2016) DOI: 10.1088/2053-1583/3/4/045009
[164] Fallahazad, B., Lee, K., Kang, S, Xue, J., Larentis, S., Corbet, C., Kim, K., Movva, H.C., Taniguchi, T., Watanabe, K., Register, L.F., Banerjee, S.K., Tutuc, E., Gate-tunable resonant tunneling in double bilayer graphene heterostructures, Nano Lett. 15, 1, 428-33 (2015) DOI: 10.1021/nl503756y
[165] Liu, M., Yin, X., Ulinavila, E., Geng, B., Zentgraf, T., Ju, L., Wang, F., Zhang, X., A graphene-based broadband optical modulator, Nature 474, pp. 64 67 (2011) DOI: 10.1038/nature10067
[166] Ren, L., Zhang, Q., Nanot, S., Kawayama, I., Tonouchi, M.,Kono, J., Terahertz Dynamics of Quantum-Confined Electrons in Carbon Nanomaterials, J. Infrared, Millimeter and Terahertz Waves, 33, 8, pp. 846-860 (2012) DOI: 10.1007/s10762-012-9916-8

[167] Hartmann, R.R., Kono, J., Portnoi, M.E., Terahertz science and technology of carbon nanomaterials, Nanotechnology 25, 322001 (2014). DOI: 10.1088/0957-4484/25/32/322001
[168] Gao, W., Shu, J., Reichel, K., Nickel, D.V., He, X., Shi, G., Vajtai, R., Ajayan, P.M., Kono, J., Mittleman, D.M., Xu, Q., High-contrast terahertz wave modulation by gated graphene enhanced by extraordinary transmission through ring apertures, Nano Lett., 14(3), pp:1242-8 (2014) DOI: 10.1021/nl4041274
[169] Grigorenko, A.N., Polini, M., Novoselov, K.S., Graphene plasmonics, Nature Photonics, 6, pp: 749 758 (2012) DOI: 10.1038/nphoton.2012.262
[170] Chakraborty, S., Marshall, O.P., Folland, T.G., Kim, Y.-J., Grigorenko, A.N., Novoselov, K.S., Gain modulation by graphene plasmons in aperiodic lattice lasers, Science, 351, 6270, pp. 246-248 (2016) DOI: 10.1126/science.aad2930
[171] Ferrari, A.C. et al. Science and technology roadmap for graphene, related two-dimensional crystals, and hybrid systems, Nanoscale 7, 4598 4810 (2015) DOI: 10.1039/c4nr01600a
[172] Tredicucci, A.,Vitiello, M.S., Device Concepts for Graphene-Based Terahertz Photonics. IEEE J. Sel. Top. Quantum Electron. 20, 8500109 (2014) DOI: 10.1109/jstqe.2013.2271692
[173] Sun, Z., Popa, D., Hasan, T., Torrisi, F., Wang, F., Kelleher, E.J.H., Travers, J.C., Nicolosi, V., Ferrari, A.C., A stable, wideband tunable, near transform-limited, graphene-mode-locked, ultrafast laser. Nano Res. 3, 653 660 (2010). DOI: 10.1007/s12274-010-0026-4
[174] Keller, U. Recent developments in compact ultrafast lasers. Nature 424, 831 838 (2013) DOI: 10.1038/nature01938
[175] Keller, U.,. Weingarten, K.J., Kartner, F.X., Kopf, D., Braun, B., Jung, I.D., Fluck, R., Honninger, C., Matuschek, N., Aus der Au, J., Semiconductor saturable absorber mirrors (SESAMs) for femtosecond to nanosecond pulse generation in solid-state lasers. IEEE J. Sel. Top. Quantum Electron. 2, 435 453 (1996) DOI: 10.1109/2944.571743
[176] Lagatsky,A.A., Bain,F.M., Brown,C.T.A., Sibbett,W., Livshits,D.A., Erbert,G., Rafailov, E.U., Low-loss quantum-dot-based saturable absorber for efficient femtosecond pulse generation. Appl. Phys. Lett. 91, 231111 (2007) DOI: 10.1063/1.2817755

[177] Hoffmann, M. C. & Turchinovich, D. Semiconductor saturable absorbers for ultrafast terahertz signals. Appl. Phys. Lett. 96, 151110 (2010) DOI: 10.1063/1.3386542
[178] Wang, F., Maussang, K., Moumdji, S., Colombelli, R., Freeman, J.R., Kundu, I., Li, L., Linfield, E.H., Davies, A.G., Mangeney, J., Tignon, J., Dhillon, S.S., Generating ultrafast pulses of light from quantum cascade lasers. Optica 2, 944 949 (2015) DOI: 10.1364/optica.2.000944
[179] Brida, D., Tomadin, A., Manzoni, C., Kim, Y.J., Lombardo, A., Milana, S., Nair, R.R., Novoselov, K.S., Ferrari, A.C., Cerullo, G., Polini, M., Ultrafast collinear scattering and carrier multiplication in graphene. Nat. Commun. 4, 1987 (2013) DOI: 10.1038/ncomms2987
[180] Sun, Z., Hasan, T., Torrisi, F., Popa, D., Privitera, G., Wang, F., Bonaccorso, F., Basko, D.M., Ferrari, A.C., Graphene mode-locked ultrafast laser. ACS Nano 4, 803 810 (2010) DOI: 10.1021/nn901703e
[181] Bonaccorso, F., Lombardo, A., Hasan, T., Sun, Z., Colombo, L., Ferrari, A.C., Production and processing of graphene and 2d crystals, Mater. Today 15, 564 589 (2012) DOI: 10.1016/s1369-7021(13)70014-2
[182] Baek, H., Lee, H.W., Bae, S., Hong, B.H., Ahn, Y.H., Yeom, D.I., Rotermund, F., Efficient mode-locking of Sub-70-fs Ti:sapphire laser by graphene saturable absorber. Appl. Phys. Express 5, 032701 (2012) DOI: 10.1143/apex.5.032701
[183] Zaugg, C. A., Sun, Z., Wittwer, V.J., Popa, D., Milana, S., Kulmala, T.S., Sundaram, R.S., Mangold, M., Sieber, O.D., Golling, M., Lee, Y., Ahn, J.H., Ferrari, A.C., Keller, U., Ultrafast and widely tuneable vertical-external-cavity surface-emitting laser, mode-locked by a graphene-integrated distributed Bragg reflector. Opt. Express 21, 31548 31559 (2013) DOI: 10.1364/oe.21.031548
[184] Mary, R., Brown, G., Beecher, S.J., Torrisi, F., Milana, S., Popa, D., Hasan, T., Sun, Z., Lidorikis, E., Ohara, S., Ferrari, A.C., Kar,A.K.,1.5 GHz picosecond pulse generation from a monolithic waveguide laser with a graphene-film saturable output coupler. Opt. Express 21, 7943 7950 (2013) DOI: 10.1364/oe.21.007943
[185] Zhang, M., Kelleher, E.J.R., Torrisi, F., Sun, Z., Hasan, T., Popa, D., Wang, F., Ferrari, A.C., Popov, S.V., Taylor, J.R., Tm-doped fiber laser mode-locked by graphene-polymer composite. Opt. Express 20, 25077 25084 (2012) DOI: 10.1364/oe.20.025077

[186] Cizmeciyan, M.N., Kim, J.W., Bae, S., Hong, B.H., Rotermund, F., Sennaroglu, A., Graphene mode-locked femtosecond Cr:ZnSe laser at 2,500 nm. Opt. Lett. 38, 341 343 (2013) DOI: 10.1364/ol.38.000341
[187] Torrisi, F., Hasan, T., Wu, W., Sun, Z., Lombardo, A., Kulmala, T.S., Hsieh, G.W., Jung, S., Bonaccorso, F., Paul, P.J., Chu, D., Ferrari, A.C., Inkjet-printed graphene electronics. ACS Nano 6, 2992 3006 (2012) DOI: 10.1021/nn2044609
[188] Torrisi, F., Coleman, J. N. Electrifying inks with 2D materials. Nat. Nanotechnol. 9, 738 739 (2014) DOI: 10.1038/nnano.2014.218
[189] Hasan, T. et al. Solution-phase exfoliation of graphite for ultrafast photonics, Phys Status Solidi Basic Res. 247, 2953 2957 (2010).
[190] Torrisi,F., Popa,D., Milana,S., Jiang,Z., Hasan,T., Lidorikis,E., Ferrari,A.C. , Stable, surfactant-free graphene-styrene methylmethacrylate composite for ultrafast lasers. Adv Opt. Mater. 4, 1088 1097 (2016) DOI: 10.1002/adom.201500760
[191] Torrisi, F., Coleman, J.N., Inkjet-printed graphene electronics. ACS Nano 6, 2992 3006 (2012) DOI: 10.1021/nn2044609
[192] Secor, E. B., Prabhumirashi, P. L., Puntambekar, K., Geier,M. L. & Hersam, M. C. Inkjet printing of high conductivity, flexible graphene patterns. J. Phys. Chem. Lett. 4, 1347 1351 (2013) DOI: 10.1021/jz400644c
[193] Ciesielski, A., Samorì, P. Graphene via sonication assisted liquid-phase exfoliation. Chem. Soc. Rev. 43, 381 398 (2014) DOI: 10.1039/c3cs60217f
[194] -broadband THz time-domain spectroscopy of common polymers using THz air photonics. Opt. Express 22, 12475 12485 (2014) DOI: 10.1364/oe.22.012475
[195] Oka, A., Tominaga, K., Terahertz spectroscopy of polar solute molecules in non-polar solvents. J. Non-Cryst. Solids 352, 4606 4609 (2006) DOI: 10.1016/j.jnoncrysol.2006.03.122
[196] Lee, S. H., Choi,M., Kim, T.T., Lee, S., Liu, M., Yin, X., Choi, H.K., Lee, S.S., Choi, C.G., Choi,S.Y., Zhang, X., Min, B., Switching terahertz waves with gate-controlled active graphene metamaterials, Nat. Mater. 11, 936 941 (2012) DOI: 10.1038/nmat3433
[197] Sensale-Rodriguez, B., Fang, T., Yan, R.S., Kelly, M.M., Jena, D., Liu, L., Xing, H.L., Unique prospects for graphene-based terahertz modulators, Appl. Phys. Lett. 99, 11 (2011) DOI: 10.1063/1.3636435

[198] Chakraborty, S., Marshall, O.P., Folland, T.G., Kim, Y.-J., Grigorenko, A.N., Novoselov, K.S., Gain modulation by graphene plasmons in aperiodic lattice lasers, Science, 351, 6270, 246-248 (2016) DOI: 10.1126/science.aad2930
[199] Castro Neto, A., GUinea, F., Peres, N.M.R., Novoselov, K.S., Geim, A.A.K., The electronic properties of graphene, Reviews of Modern Physics, 81 , 1, pp. 109 - 162 (2009) DOI: 10.1103/RevModPhys.81.109
[200] Depine, R. A., Graphene Optics: Electromagnetic Solution of Canonical Problems, IOP Concise Physics, London, UK (2017)
[201] Novoselov,K.S., Geim,A.K., Morozov,S.V., Jiang,D., Zhang,Y., Dubonos,S.V., Grigorieva,I.V., Firsov,A.A., Electric Field Effect in Atomically Thin Carbon Films, Science, 306, 5696, pp. 666-669 (2004) DOI: 10.1126/science.1102896
[202] Koppens, F.H.L., CHang, D.E., Grcia de Abajo, F.J., Graphene Plasmonics: A Platform for Strong LightMatter Interactions, Nano Letters 11, 3370 3377 (2011) DOI: 10.1364/opn.22.12.000036
[203] Falkovsky, L.A, Pershoguba, S.S.,Optical far-infrared properties of a graphene monolayer and multilayer, Physical Review B, 76, 153410 (2007) DOI: 10.1088/1742-6596/129/1/012004
[204] Xing, G., Guo, H., Zhang, X., Sum, T.C., Huan, C.H.A., The physics of ultrafast saturable absorption in graphene, Optics Express, 18, 5 (2010) DOI: 10.1364/oe.18.004564
[205] Nair, R. R. , Blake,P., Grigorenko, A.N., Novoselov,K.S., Booth,T.J., Stauber,T., Peres,N.M.R., Geim, A.K.,Fine Structure Constant Defines Visual Transparency of Graphene,Science, 320, 5881, p. 1308 (2008), DOI: 10.1126/science.1156965
[206] Tuinstra, F., Koenig, J. L., Raman spectrum of graphite, J. Chem. Phys. 53, 1126 1130 (1970) DOI: 10.1063/1.1674108
[207] Ferrari, A. C., Meyer,J. C. , Scardaci,V., Casiraghi,C., Lazzeri,M., Mauri,F., Piscanec,S., Jiang,D., Novoselov,K.S., Roth,S., Geim, A.K., Raman spectrum of graphene and graphene layers, Phys. Rev. Lett. 97, 187401 (2006) DOI: : 10.1103/PhysRevLett.97.187401
[208] Ferrari, A. C., Robertson, J., Resonant Raman spectroscopy of disordered, amorphous, and diamond-like carbon, Phys. Rev. B 64, 075414 (2001) DOI: 10.1103/physrevb.64.075414

[209] Ferrari, A. C., Robertson, J., Interpretation of Raman spectra of disordered and amorphous carbon, J. Phys. Rev. B 61, 14095 14107 (2000) DOI: /10.1103/physrevb.61.14095
[210] Thomsen, C., Reich, S., Double resonant Raman scattering in graphite, Phys. Rev. Lett. 85, 5214 5217 (2000) DOI:10.1103/physrevlett.85.5214
[211] Yu, Q., Lian,J., Siriponglert,S.,Li,H., Chen,Y.P., Pei,S.-S., Graphene segregated on Ni surfaces and transferred to insulators, Appl. Phys. Lett. 93, 113103 (2008) DOI: 10.1063/1.2982585
[212] Zheng,Z., Zhao,C., Lu,S., Chen,Y., Li,Y., Zhang,H., Wen,S., Microwave and optical saturable absorption in graphene, Opt. Express 20, 23201 23214 (2012) DOI: 10.1364/OE.20.023201
[213] Dai, J., Zhang, J., Zhang, W., Grischkowsky, D., Terahertz time-domain spectroscopy characterization of the far-infrared absorption and index of refraction of high resistivity, float-zone silicon, J. Opt. Soc. Am. B, 21, 7, 1379-1386 (2007) DOI: 10.1364/JOSAB.21.001379
[214] Giordano, M.C., Mastel, S., Liewald, C., Columbo, L.L., Brambilla, M., Viti, L., Politano, A., Zhang, K., Li, L., Davies, A.G., Linfield, E.H., Hillenbrand, R., Keilmann, F., Scamarcio, G., Vitiello, M.S., Phase-resolved terahertz self-detection near-field microscopy, Opt. Express, 26 (14), pp. 18423-18435 (2018) DOI: 10.1364/OE.26.018423.
[215] Jaeger, R. C., Lithography. Introduction to Microelectronic Fabrication (2nd edition). Upper Saddle River: Prentice Hall (2002).
[216] Chen, Y., Nanofabrication by electron beam lithography and its applications: A review, Microelectronic Engineering, 315, 5 (2015) DOI: 10.1016/j.m10.1016/j.mee.2015.02.042ee.2015.02.042
[217] Tellier, C.R., Huve, G., Leblois, T.G., Anisotropic chemical etching of III-V crystals, Active and passive electronic components, 27, 133-154 (2004) DOI: 10.1080=08827510310001616858
[218] Jin, J.M., The finite element method in electromagnetics (3rd edition), Wiley - IEEE Press, USA (2014)
[219] Stratton, J.A., Electromagnetic Theory, McGraw-Hill, USA (1941)

IMPACT OF RESEARCH

1. Pubblications

- Biasco, S., Ciavatti, A., Li, L., Davies, A.G., Linfield, E.H., Beere, H.E., Ritchie, D.A., Vitiello, M.S., Highly efficient surface-emitting semiconductor lasers exploiting quasi-crystalline distributed feedback photonic patterns, submitted manuscript (2019)
- Biasco, S., Beere, H.E., Ritchie, D.A., Li, L., Davies, A.G., Linfield, E.H., Vitiello, M.S., Frequency-tunable continuous-wave random lasers at terahertz frequencies, Nature Light: Science & Applications 8, 43 (2019) DOI: 10.1038/s41377-019-0152-z
- Biasco, S., Garrasi, K., Castellano, F., Li, L., Beere, H.E., Ritchie, D.A., Linfield, E.H., Davies, A.G.,Vitiello, M.S., Continuous-wave highly-efficient low-divergence terahertz wire lasers, Nature Communications, 9, 1122-1 - 1122-8 (2018) DOI:10.1038/s41467-018-03440-4
- Biasco, S., Garrasi, K., Castellano, F., Li, L., Beere, H.E., Ritchie, D.A, Linfield, E.H., Davies, A.G., Vitiello, M.S.,, Continuous-wave highly-efficient low-divergence terahertz wire lasers, Proceedings of the 43rd International conference on Infrared, Millimeter and Terahertz waves - IRMMW - THz, IEEE Xplore (2018) DOI: 10.1109/IRMMW-THz.2018.8510384
- Biasco, S., Li, L., Linfield, E.H., Davies, A.G., Vitiello, M.S., Multimode, aperiodic terahertz surface emitting laser resonators, Photonics 3, 32, (2016) DOI: 10.3390/photonics3020032

2. Oral presentations

- Biasco, S., Garrasi, K., Castellano, F., Li, L., Beere, H.E., Ritchie, D.A., Linfield, E.H., Davies, A.G., Vitiello, M.S., "Continuous-wave highly efficient low-divergence terahertz wire lasers", IRMMW-THz 2018 - International conference on Infrared, Millimeter and Terahertz waves, Nagoya, Japan (September 2018)
- Biasco, S., Li, L., Linfield, E.H., Davies, A.G., Beere, H.E., Ritchie, D.A., Vitiello, M.S., "Frequency tunable continuous-wave random THz lasers", IQCLSW 2018 - International Quantum Cascade Laser School and Workshop, Cassis, France (September 2018)

- Biasco, S., Garrasi, K., Li, L., Linfield, E.H., Davies, A.G., Beere, H.E., Ritchie, D.A., Vitiello, M.S., "High-power, low-divergence, single-mode THz quantum cascade wire lasers operating in pulsed and continuous-wave regime", ITQW 2017 - Intersubband Transitions in Quantum Wells, Singapore (September 2017)
- Biasco, S., Garrasi, K., Li, L., Linfield, E.H., Davies, A.G., Vitiello, M.S., "High-power, low-divergence, single-mode THz quantum cascade wire lasers operating in pulsed and CW regime", OTST 2017 - Optical Terahertz Science and Technology, London, United Kingdom (April 2017)
- Biasco, S., Garrasi, K., Li, L., Linfield, E.H., Davies, A.G., Vitiello, M.S., "Low-divergence, high-power single-mode Terahertz wire laser", IQCLSW 2016 - International Quantum Cascade Laser School and Workshop, Cambridge, United Kingdom (September 2016)
- Biasco, S., Li, L., Linfield, E.H., Davies, A.G., Vitiello, M.S., "Two-dimensional random quantum cascade resonators at Terahertz frequencies", 70th Workshop: Terahertz science, nanotechnologies and applications, Erice, Italy (July 2016)

3. Invited oral presentation

- Biasco, S., Garrasi, K., Li, L., Beere, H.E., Ritchie, D.A., Davies, G.A., Linfield, E.H., Vitiello, M.S., "Aperiodic photonic architectures for high-power THz quantum cascade lasers", Terahertz emitters, receivers, and applications X, SPIE Symposium: Optical Engineering + Applications, San Diego, USA (to be held in August 2019)

4. Poster presentation

- Biasco, S., Li, L., Linfield, E.H., Davies, A.G., Vitiello, M.S., "Random Terahertz quantum cascade resonators", IQCLSW 2016 - International Quantum Cascade Laser School and Workshop, Cambridge, United Kingdom (September 2016)

5. Scientific awards

- "NEST Prize for Nanoscience 2018: special edition in memory of Stefano Guiducci". The special edition of the NEST Prize was assigned based on the scientific papers published in 2018 by young NEST researchers (under the

age of 30) as first authors. Award received in June 2019 for the publication: Nature Communications, 9, 1122 (2018)

- "EPL (EuroPhysics Letters) award for the best oral presentation" among PhD students presenting during the "70th Workshop: terahertz science, nanotechnologies and applications", Erice, Italy (2016)